A STUDY OF SUPERCONDUCTIVITY IN A SERIES OF STRONTIUM PLATINUM PHOSPHIDES

A Dissertation

Presented to

the Faculty of the Department of Physics

University of Houston

In Partial Fulfillment

of the Requirements for the Degree

Doctor of Philosophy

By

BenMaan I. Jawdat

August 2015

A STUDY OF SUPERCONDUCTIVITY IN A SERIES OF STRONTIUM PLATINUM PHOSPHIDES

BenMaan I. Jawdat

APPROVED:

Prof. Paul C.W. Chu, Chairman
Dept. of Physics

Prof. Wei-Kan Chu, Co-Chairman
Dept. of Physics

Prof. John H. Miller Jr., Co-Chairman
Dept. of Physics

Prof. Chin-Sen Ting, Co-Chairman
Dept. of Physics

Prof. John C. Wolfe, Co-Chairman
Dept. of Electrical Engineering

Dean, College of Natural Sciences and Mathematics

DEDICATION

To my parents

ACKNOWLEDGEMENTS

Science is inherently a collaborative endeavor, and graduate school is an introduction to this endeavor. I have been privileged to undertake this experience under the guidance of and in collaboration with excellent people who have helped me to grow as a scientist and as a person.

I would like to express my deepest gratitude to my advisor Dr. Paul Chu for providing me the opportunity to pursue this research and for his continued guidance. Dr. Chu exemplifies what it means to be a scientist, with immense patience, curiosity, and persistence, and I am grateful to have had the chance to learn from him.

I am very grateful to the members of my dissertation committee, Dr. Wei-Kan Chu, Dr. John Miller Jr., Dr. Chin-Sen Ting, and Dr. John Wolfe, whose guidance and suggestions throughout the course of my project were a fundamental part of my education.

I would like to give special thanks to Dr. Bing Lv, with whom I have worked on this research project and without whom this work would not have been possible, for his continuous help and advice throughout the past few years. Dr. Lv has synthesized all of the compounds studied in this thesis with great skill and knowledge and has generously provided much guidance and direction; I cannot overstate his contribution.

Many thanks to Dr. Zheng Wu, who was always willing to help me with experimental setups and low-temperature measurements, even at late hours of the night or on the weekends. Dr. Yuyi Xue was always very welcoming of any discussions,

frequently helped to point me in the right direction; I learned a lot about superconductivity from him. Dr. Bernd Lorenz was always willing to answer my questions about physics and superconductivity and welcomed open discussion. Dr. Melissa Gooch and Dr. Fengyan Wei taught many experimental techniques. I sincerely thank my classmates, Keshav Shrestha, Quantum Deng, and Kui Zhao, for all of the long discussions, warm friendship, and good times we have shared.

Finally, I would like to thank my family. My brother, for his endless support, and my parents, for their unyielding, tenacious, and steadfast encouragement.

A STUDY OF SUPERCONDUCTIVITY IN A SERIES OF STRONTIUM PLATINUM PHOSPHIDES

An Abstract of a Dissertation

Presented to

the Faculty of the Department of Physics

University of Houston

In Partial Fulfillment

of the Requirements for the Degree

Doctor of Philosophy

By

BenMaan I. Jawdat

August 2015

ABSTRACT

In this work, the superconductivity in a series of strontium platinum phosphides was investigated. Three compounds, $SrPt_3P$, $SrPt_6P_2$, and $SrPt_{10}P_4$, the latter two of which we discovered, were synthesized and characterized. We studied $SrPt_3P_{1-x}Si_x$ resistively, magnetically, and calorimetrically, and found an apparent non-scaling of the T_c with the density of states at the Fermi level $N(E_F)$ that can be attributed to a significant weakening of the electron-phonon interaction strength. We found superconductivity in the new structure type $SrPt_6P_2$ at $T_c = 0.6$ K and attribute the lower value of T_c to a weak coupling strength as evidenced by our specific heat measurement and analysis. Superconductivity at $T_c = 1.4$ K was found in another new structure type compound $SrPt_{10}P_4$ with structural building blocks reminiscent of those from both $SrPt_3P$ and $SrPt_6P_2$. In $SrPt_{10}P_4$, our specific heat and upper critical field H_{c2} measurements indicate the opening of two superconducting gaps Δ_1 and Δ_2 below T_c. A method of comparing the contributions to superconductivity in different compounds by analysis of the specific heat is developed in which the contribution from the density of states at the Fermi level $N(E_F)$ is separated from that of the interaction strength V and is applied to gain insight into the factors driving the superconductivity in these compounds.

Contents

List of Figures

List of Tables

Chapter 1

Introduction

Superconductivity is one of the most heavily investigated areas of active research in history. Since 1911, when Heike Kamerlingh Onnes made his historic discovery of superconductivity in mercury, the field has drawn and often humbled some of the brightest minds in science. This concentration of efforts has led to some remarkable results, such as the 1957 BCS microscopic theory of superconductivity[1], which is regarded as one of the greatest achievements of theoretical physics. It is easy to see why so much effort is put into further understanding superconductivity when the possible applications are considered. Besides some of the current applications of superconductivity such as magnetic resonance imaging (MRI), nuclear fusion, and particle accelerators, future applications could include long-distance magnetically levitated transportation, ultra-high power density motors, quantum computing, and more. Integral to the implementation of these and other future applications are new materials.

The discovery of new materials has driven breakthroughs in our understanding of superconductivity. After the discovery of superconductivity in the A15 type compound V_3Si in 1953[2] and Nb_3Sn in 1954[3], the highest transition temperature remained at 23.2 K in Nb_3Ge[4, 5] for decades. This apparant plateau in the increase of T_c seemed to support a prediction made in 1968 that the upper limit of T_c is in the 30s K[6]. During this time, the unexpected observation of superconductivity in 1979 in $CeCu_2Si_2$ at low temperature ($T_c \approx 1K$) heralded the exciting new field of heavy-Fermion superconductivity[7]. The discovery of superconductivity in a new class of compounds, the copper oxides, in 1986 by Bednorz and Muller[8] and the historic discovery of superconductivity above the boiling point of liquid nitrogen in $YBa_2Cu_3O_{7-x}$ by Chu and colleagues [9, 10, 11, 12] in 1987 revitalized the field and provided a new framework within which to study and understand superconductivity. Soon after this discovery, the transition temperature rapidly advanced to 115 K in $Bi_2Sr_2Ca_2Cu_3O_{10}$[13], to 125 K in $Tl_2Ba_2Ca_2Cu_3O_{10}$[14, 15], to 133.5 K in $HgBa_2Ca_2Cu_3O_9$[16], to the current highest confirmed T_c of 164 K by Chu and colleagues in $HgBa_2Ca_2Cu_3O_9$ under pressure[17, 18]. In 2001, the discovery of superconductivity in MgB_2[19] provided a model system of a strong-coupling phonon-mediated superconductor with a high transition temperature of 39 K. In the mid-2000's, with the number of publications in high temperature superconductivity decreasing, many were less optimistic about the future of the field[20, 21]. More recently, however, the discovery of the iron-based superconductors in 2008[22, 23] reinforced the evidence for synergistic effects between magnetism and superconductivity observed in the cuprates and further solidified

that the discovery and characterization of new superconducting materials is critically important to furthering our understanding of this field.

In the search for new superconducting materials, the investigation of platinum-based materials has yielded many new compounds with a wide variety of structural and physical properties. These have included the heavy Fermion uranium-based superconductor UPt_3[24, 25] and the metal-hydride (at high pressure) PtH[26, 27, 28]. Specifically, superconducting compounds that include an alkali metal, platinum, and a post-transition element (such as P, Ge, or B), have included the non-centrosymmetric heavy Fermion $CePt_3Si$[29], the non-centrosymmetric Li_2Pt_3B[30, 31, 32], the honeycomb-type SrPtAs[33], the layer compound $SrPt_2Ge_2$[34], and the Ge-based skutterudites MPt_4Ge_{12}[35].

Recently, strong-coupling electron-phonon type superconductivity was discovered in the antiperovskite $SrPt_3P$[36]. The structure of $SrPt_3P$ is composed of corner-shared distorted octahedra. The structure caught the attention of many due to its similarity to the non-centrosymmetric $CePt_3Si$. Several interesting physical properties were found in $SrPt_3P$ such as possible multi-band superconductivity and an observed non-scaling of the T_c with the density of states at the Fermi level $N(E_F)$ upon total replacement of Sr with Ca and La. These observations, followed by results from our preliminary investigations, raised several questions: Can this observation be generalized to replacement with other elements? If the $N(E_F)$ is not responsible for the shift of T_c, what is? Why is the T_c so sensitive to small changes in the crystal structure? Given the interesting nature of this compound and the questions raised, we asked ourselves if it would be possible for us to find other Sr -

Pt - P compounds to address the above questions and more.

During the course of our search for new Pt-based materials, we indeed discovered two new superconductors in this Sr - Pt - P material system with unique structure types. Strikingly, the superconducting transition temperature varies by over an order of magnitude within this material family despite their general similarities, which include 1) all contain Pt_6P polyhedra as building blocks, where a central P atom is coordinated by 6 Pt atoms, 2) the crystal structures of these three compounds are composed of networks of these Pt_6P with Sr atoms filling in cavity sites, and 3) the polyhedra are either octahedra or trigonal prisms, which can be considered distortions of each other. The nature of the superconductivity in these compounds is diverse, with weak-coupling, strong-coupling, single-gap, and multi-gap superconductivity all occuring. In this thesis, a systematic investigation of the chemical, structural, and physical properties of these three compounds was carried out. A method of comparing the contributions to superconductivity in different compounds by analysis of the specific heat is developed in which the contribution from the density of states at the Fermi level $N(0)$ is separated from that of the interaction strength V and is applied to these compounds to gain insight into the factors driving the transition temperature T_c.

Chapter 2

Background

2.1 Basic properties of superconductors

Superconductivity, a macroscopic quantum state which emerges when electrons pair together below a certain critical temperature, is associated with two fundamental properties. The first of these properties is the sudden transition from a state with finite electrical resistivity ρ above the critical temperature to a state with zero electrical resistivity below (Figure 2.1). The second is the transition to a state of perfect diamagnetism ($4\pi\chi = -1$) and the subsequent expulsion of magnetic fields below the critical temperature. Historically, the sudden loss of electrical resistivity was the first property discovered in 1911 by Kamerlingh Onnes[37], while the second property was discovered in 1933 by Walther Meissner and Robert Ochsenfeld[38] and is known as the Meissner effect.

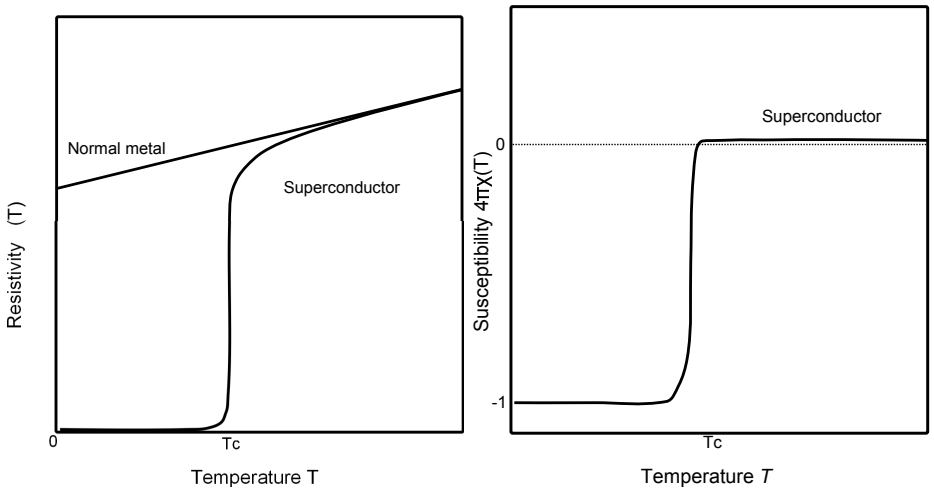

Figure 2.1: (Temperature dependence of resistivity for a normal metal compared to a superconductor (left) and temperature dependence of magnetic susceptibility for a superconductor (right). (Adapted from [39]).

2.1.1 Perfect conductivity

While a superconductor conducts electricity perfectly and can therefore be considered a perfect conductor, a perfect conductor would not necessarily be a superconductor. In other words, perfect conductivity is not a sufficient condition for superconductivity. To see this, one can consider the following thought experiment[39] (summary shown in Figure 2.2). Imagine a sample becomes a perfect conductor below $T = T_c$ ($\rho = 0$). Next, applying an external magnetic field will induce a current to screen the applied field as required by Lenz' law to maintain zero field inside the sample. The field will remain zero inside the sample after the field is turned off (let this be "State 1')'. Now, consider a similar sequence, but beginning with cooling down below the temperature T_c while the magnetic field is applied. If we then remove the magnetic field, screening currents will be induced to maintain

zero change in flux, and with zero external magnetic field there will be a persistent field inside the sample generated by the screening currents. Call this “State 2”. Although the thermodynamic variables are the same in both cases, the state of the sample is very different. Regardless of whether the magnetic field is applied below T_c or above T_c, the total expulsion of magnetic flux will occur in a superconductor. Superconductors, therefore, are not simply perfect conductors; superconductivity is a thermodynamic state.

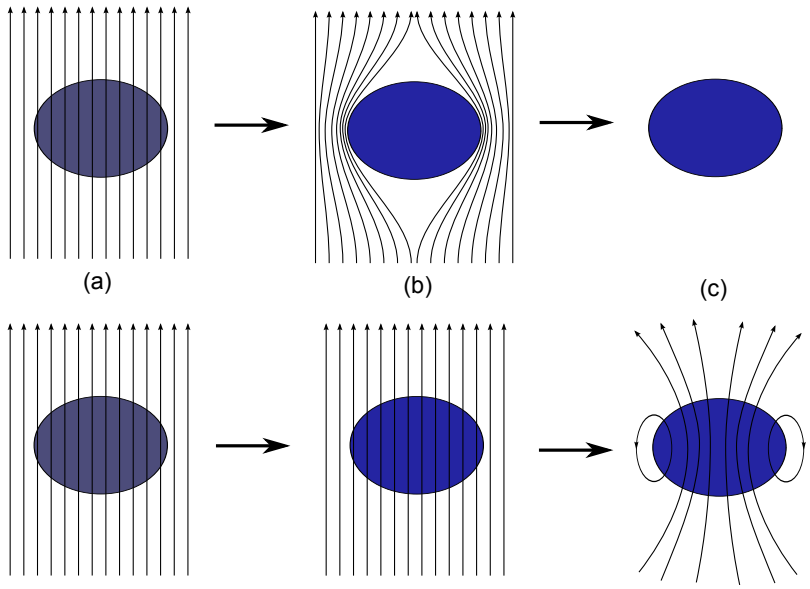

Figure 2.2: Comparison between a superconductor (top) and normal metal (bottom) undergoing a sequence of events: (a) $T > T_c$, $H > 0$, (b) after cooling below T_c, (c) after setting $H = 0$.

2.1.2 Perfect diamagnetism

Superconductors exhibit perfect diamagnetism at low fields. This means that when an external magnetic field is applied, screening currents are induced which produce

a magnetic field that exactly cancels the applied magnetic field. From Maxwell's equations:

$$\nabla \cdot \mathbf{B} = 0$$

$$\mathbf{B} = \mathbf{H} + 4\pi\mathbf{M}$$

Setting the condition $\mathbf{B} = 0$, we get:

$$4\pi\frac{d\mathbf{M}}{d\mathbf{H}} = 4\pi\chi = -1$$

where $\chi = d\mathbf{M}/d\mathbf{H}$ is the magnetic susceptibility.

2.1.3 Type I vs. type II

Superconductors can be classified into two distinct types based on their response to an external magnetic field. In type I superconductors, perfect diamagnetism with $4\pi\chi = -1$ continues until the critical magnetic field H_c is reached, at which point the perfect diamagnetism is suddenly destroyed. In this type of superconductor, the magnetic field inside the superconductor is either perfectly shielded with $\mathbf{B} = 0$ in the interior of the material, or the magnetic field totally penetrates as in a normal metal. Type II superconductors differ in that there are two different critical fields H_{c1} and H_{c2}. In the region below H_{c1}, the material behaves the same

as a type I superconductor. However, in between H_{c1} and H_{c2} there exist non-superconducting regions where the magnetic field can penetrate with "vortices" of shielding current around those small regions. This difference between type I and type II superconductors is visualized in Figure 2.4.

2.2 Overview of the BCS theory

In 1956, Leon Cooper showed that even a weak attraction can bind electrons together into a pair as a bound state[40], as shown in Figure 2.3. To do this, he considered a simple model of two electrons added to a Fermi sea at T = 0:

$$\psi_0(\mathbf{r}_1, \mathbf{r}_2) = \left[\sum_{k>k_F} g_{\mathbf{k}} \cos[\mathbf{k}(\mathbf{r}_1 - \mathbf{r}_2)]\right](\alpha_1\beta_2 - \beta_1\alpha_2) \tag{2.1}$$

where $\mathbf{r_1}$ and $\mathbf{r_2}$ are the positions of the two electrons, $\mathbf{k}$ is the momentum, and the α_i and β_i are the spin states of the electrons.

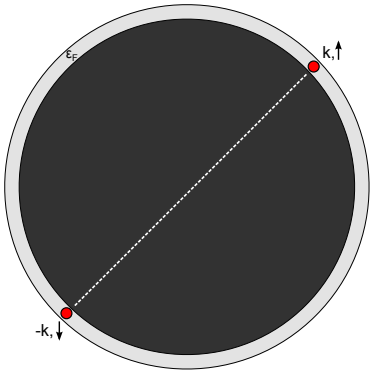

Figure 2.3: Sketch of a Cooper pair.

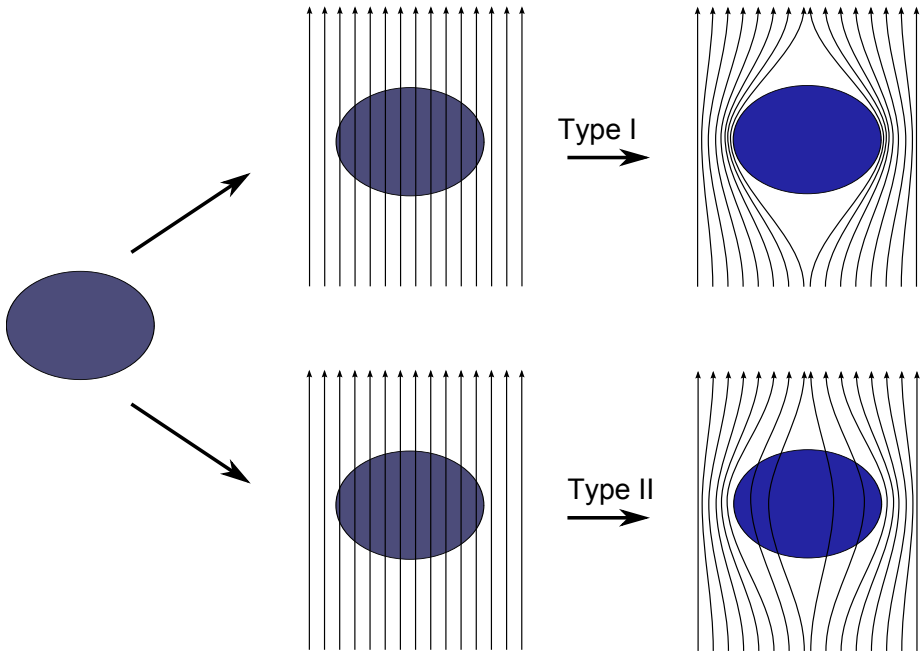

Figure 2.4: Meissner effect in type I (top) and type II (bottom) superconductors upon field-cooling through the superconducting transition above H_{c1} and below H_{c2}.

Cooper introduced an important approximation: for k states out to a cutoff energy $\hbar\omega_c$ away from E_F, $V_{kk'} = V$, and beyond that $V_{kk'} = 0$. In making this approximation, he was able to arrive at the result that an arbitrarily small attractive interaction at low temperature would result in a lowering of the energy for a pair of electrons.

Bardeen, Cooper, and Schrieffer extended this argument in 1957 in their historic BCS theory[1] which considered the phonon mediated electron-electron interaction and introduced the gap parameter Δ_k. The BCS Hamiltonian is written in the following way:

$$H = \sum_{\mathbf{k},\sigma} \epsilon(\mathbf{k}) C^\dagger_{\mathbf{k}\sigma} C_{\mathbf{k}\sigma} + \sum_{\mathbf{k},l} V_{\mathbf{k}l} C^\dagger_{\mathbf{k}\uparrow} C^\dagger_{-\mathbf{k}\downarrow} C_{-l\downarrow} C_{l\uparrow}$$

This Hamiltonian consists of two parts. The first term is the kinetic energy of the electrons. The second term is the phonon-mediated electron-electron interaction. Here, $C^\dagger_{\mathbf{k}\sigma}$ and $C_{\mathbf{k}\sigma}$ are the creation and annihilation operators, respectively, for electrons with momentum $\mathbf{k}$ and spin σ.

The gap Δ_k defined by BCS is an important parameter in superconductivity and $2\Delta_k$ corresponds to the minimum energy needed to break a cooper pair and create an electron-hole pair quasiparticle excitation. The temperature dependence of the superconducting gap $\Delta(T)$ can be solved for numerically from the BCS result:

$$\frac{1}{N(0)V} = \int_0^{\hbar\omega_c} \frac{\tanh \frac{1}{2}\beta(\xi^2 + \Delta^2)^{1/2}}{(\xi^2 + \Delta^2)^{1/2}} d\xi$$

where $E_k \equiv \sqrt{\xi_k^2 + |\Delta_k|^2}$.

It is very useful to consider two limiting cases of this result. In the case of $T \to T_c$, the superconducting gap $\Delta \to 0$ and the equation can be simplified to find the BCS formula for T_c:

$$\frac{1}{N(0)V} = \log \frac{\omega_D}{T_c} \quad \Longrightarrow \quad T_c \approx \omega_D \exp\left(-1/N(0)V\right)$$

In the case of $T \to 0$, $\tanh(\beta E_k/2) \to 1$, and we can get:

$$\frac{1}{N(0)V} \approx \ln\left(\frac{2\omega_D}{\Delta}\right) \quad \Longrightarrow \quad \Delta \approx 2\omega_D \exp\left(-1/N(0)V\right)$$

The dependence of the superconducting gap Δ on the coupling strength $\lambda = N(0)V$ can be seen in Figure 2.5, where the relation $\Delta_0/\hbar\omega_D = 1/\sinh(1/N(0)V)$ is plotted without the weak coupling approximation. The region where the weak-coupling approximation is valid is shown in the inset of Figure 2.5.

The BCS theory can be visualized in the following way (Figure 2.6). Consider an electron (call it electron 1) moving through a crystal lattice. As it moves through the lattice, it will attract nearby ions on its path due to the Coulomb attraction. The ions, feeling the pull of electron 1, are moved so that the lattice is slightly deformed. Due to the heavier mass of the ions, this deformation will remain for some time after the electron passes. As a second electron, electron 2, moves towards this region, it will feel a pull from the ions which are still out of place. Therefore, in an indirect way, electron 1 is attracting electron 2. The two electrons are thus experiencing an attractive net potential which is mediated by phonons (Figure 2.7).

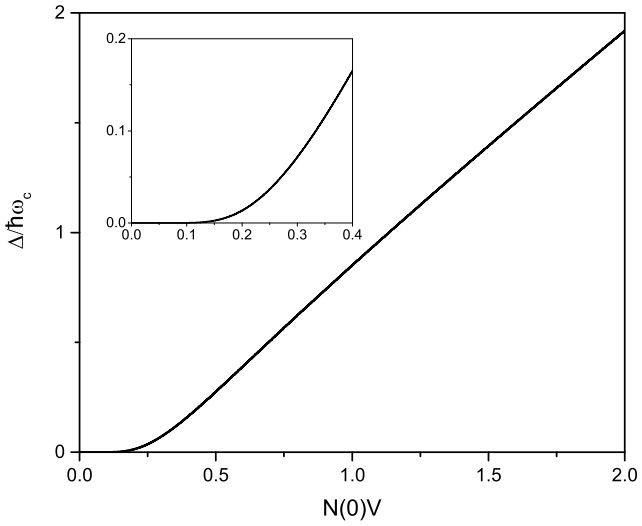

Figure 2.5: Dependence of the superconducting gap on the coupling strength N(0)V (here the dimensionless $\Delta/\hbar\omega_c$ is plotted).

2.3 The α-model

As mentioned previously, the superconducting gap Δ is an important parameter in the theory of superconductivity. In the conventional superconductors which are well-described by the BCS theory, the superconducting gap is isotropic. An isotropic gap means that the energy required to break a Cooper pair is the same at any point on the Fermi surface. On the other hand, there are many superconductors which are not well-described by an isotropic gap and may have gaps with nodes (points on the Fermi surface where the superconducting gap is equal to zero). Furthermore, a superconductor does not have to be limited to only one superconducting gap. Indeed, there are materials where more than one superconducting gap have been observed. The most notable example of this is MgB_2 which is known

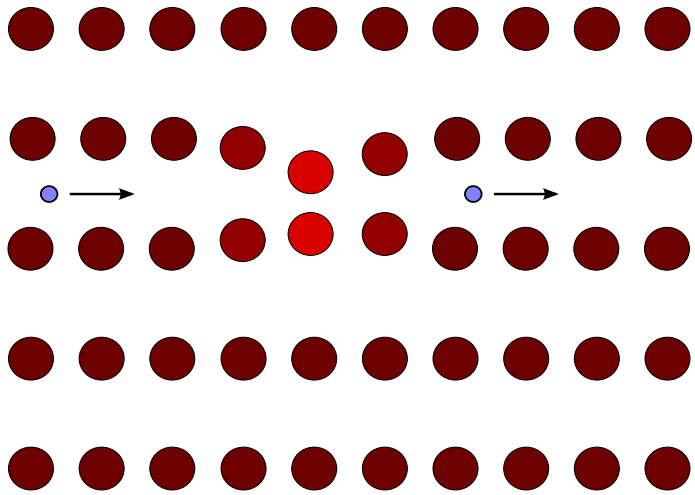

Figure 2.6: Phonon-mediated electron-electron attractive interaction.

to have two superconducting gaps based on specific heat, critical field, and other measurements[19, 41, 42].

The specific heat is related to the superconducting gap in the following way:

$$C_{es} = 2\beta k \sum_{\mathbf{f}} -\frac{\partial f_{\mathbf{k}}}{\partial E_{\mathbf{k}}} \left(E_{\mathbf{k}}^2 + \frac{1}{2}\beta \frac{d\Delta^2}{d\beta^2} \right)$$

In an extension of the BCS theory, Padamsee et al. [43] introduced the α-model to fit experimental data for superconductors with stronger or weaker-coupling than the BCS weak-coupling value of $\Delta/k_B T_c = 1.764$. In this model, the zero temperature value of the superconducting gap $\Delta(0)$ is allowed to become a variable parameter α, while the normalized temperature dependence $\Delta(T)/\Delta(0)$ is the same as that of the BCS theory. After introducing the reduced variables $\bar{\Delta} = \frac{\Delta}{\Delta(0)}$, $\bar{\epsilon} = \frac{\epsilon}{\Delta(0)}$, and $t = \frac{T}{T_c}$, along with $\alpha_{BCS} = \Delta(0)/k_B T_c$, the specific heat can be re-written in the following way[44]:

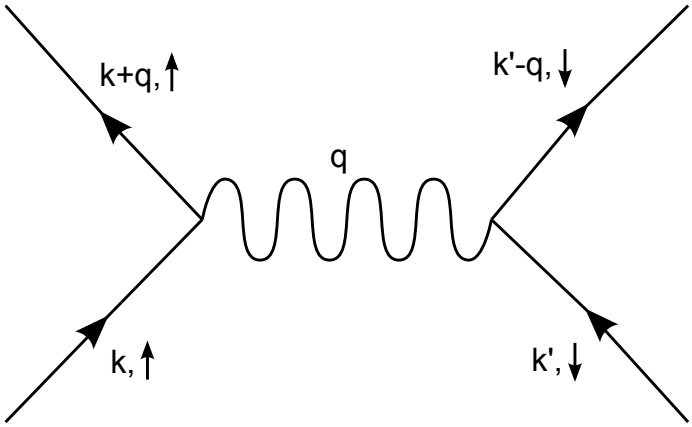

Figure 2.7: Electron-phonon interaction.

$$\frac{C_{es}(t)}{\gamma_N T_c} = \frac{6\alpha_{BCS}^3}{\pi^2 t}\int_0^\infty f(1-f)\left(\frac{\bar{E}^2}{t} - \frac{1}{2}\frac{d\bar{\Delta}^2}{dt}\right)d\bar{\epsilon}$$

where:

$$\gamma_N = \frac{2\pi^2 k_B^2}{3}N(0)$$

is the normal-state Sommerfeld electronic specific heat coefficient. The above equation for the specific heat can be solved numerically to fit experimentally measured data for different values of α. In the case of two superconducting gaps, one can introduce two gap parameters, Δ_1 and Δ_2, and use the same procedure as above.

Chapter 3

Experimental Methods

3.1 Sample preparation

The materials investigated in this thesis were prepared by solid-state synthetic techniques. Typically, the solid-state synthetic method consists of mixing the precursors together in the solid state, usually in powder form. In some cases, this would simply consist of mixing powders of the elemental precurors. However, in many other cases, the precursors, or "reactants", may themselves be pre-reacted compounds and may or may not be in the convenient powder form. The reactants are mixed together using an agate mortar and pestle and are ground to fine powders. The powder is then pressed into a pellet under pressure to facilitate reactivity at high temperature. If metal chunks are used for one or more of the precursors, they are added into the powder at this stage. In the case of the air-sensitive materials studied in this dissertation, all operations are performed in an inert argon atmosphere inside of

a glove box, and the reactants pellet is placed in an alumnia crucible and sealed under vacuum in a quartz tube. The quartz tube is then placed into a furnace which will heat the reactants pellet up to high temperature following a specific temperature profile based on the particular phase which is desired. To improve the homogeneity of the sample, especially in the case where non-powder precurors are used (such as metal chunks), a second round of grinding, pelletizing, and heating is performed. The whole process may take up to several weeks and care must be taken at each step to ensure no contaminants are introduced. Though this method is time consuming, it is preferred over faster methods such as arc melting due to the constraints of the materials studied in this dissertation. Phosphorus is very volatile and rapid heating such as that carried out in an arc-melting furnace would cause much of the phosphorus to vaporize; beyond the fact that this would prevent the compound of interest from being formed, phosphorus is dangerous and must be handled very carefully. Another constraint in the case of the materials studied in this thesis is the existence of multiple phases with different stoichiometries. These different phases are thermodynamically favored at reaction temperatures which are not dramatically different from each other. This means that temperature control is a very important factor in the preparation of these materials. Traditional solid-state synthetic techniques allow for the management of these constraints.

3.1.1 $SrPt_3P$

The synthesis of $SrPt_3P$ was carried out as follows. Stoichiometric amounts of platinum powder, prereacted PtP_2 powder, and strontium pieces were mixed together

in a glove box under argon atmosphere with total O_2 and moisture level less than 1 ppm. The mixture was pressed into a small pellet and loaded into a clean Al_2O_3 crucible. The crucible together with the pellet was then sealed in a clean quartz tube under vacuum. The whole assembly was then put inside a tube furnace for reaction. The reaction sequence was as follows: the tube was first heated to 400 °C for 12 hours, and then to 900 °C for 72 hours. A further step of regrinding the pellet under argon atmosphere, sealing in a clean quartz tube under vacuum, and annealing at 900 °C for three days was carried out to improve the homogeneity of the sample. The sample was quenched in ice water after being cooled down to 400 °C in order to avoid the formation of white phosphorus.

3.1.2 $SrPt_6P_2$

A pure phase of $SrPt_6P_2$ was synthesized by the high temperature reaction of Sr pieces, Pt powder, and prereacted PtP_2 from Pt and P powder within a clean Al_2O_3 crucible enclosed in a clean and dried fused-silica tube. Thereafter, the tube was sealed under vacuum. The tube was placed in a furnace, heated to 900 °C, kept at 900 °C for 4 days, and then cooled down at 20 °C/h to 400 °C, and finally quenched in ice water. To improve the homogeneity, the sample was reground, cold-pelletized, and then sintered following the previously described temperature profile. The resulting pellet is very dense with an approximate density of ~ 8.6 g/cm^3. The synthesis procedures were carried out within a purified argon atmosphere glovebox with total O_2 and H_2O levels of < 0.1 ppm. (Note: a small piece of Zr foil (oxygen getter) was added at the opposite end of the fused-silica tube without contacting

the reaction charge to ensure that oxygen did not enter the compound; the Zr foil did not decompose and our X-ray diffraction results show that synthesis without the Zr oxygen getter also show a pure phase).

3.1.3 $SrPt_{10}P_4$

The synthesis of $SrPt_{10}P_4$ was carried out similarly to $SrPt_3P$ and $SrPt_6P_2$, but with a different reaction profile. Stoichiometric amounds of reactants (platinum powder, prereacted PtP_2 powder, and strontium pieces) were mixed together in a glove box and the mixture was pressed into a pellet which was then loaded into a clean Al_2O_3 crucible. Together with the pellet the crucible was sealed in a clean quartz tube under vacuum and the assembly was placed into the tube furnace for reaction. The reaction sequence was as follows: the tube was first heated at 1 °C / min to 500 °C, and then heated at 1 °C / min to $\approx$ 1100 °C. The tube was kept at 1100 ° C for 2 days and then slowly cooled overnight to 450 °C followed by quenching in air. The sample was then reground, cold-pelletized, and the above reaction sequence was repeated.

3.2 Crystal structure characterization

3.2.1 Single crystal X-ray diffraction

Single crystal X-ray diffraction was used to characterize the crystal structures of new compounds with previously unknown structures. Small crystals with sizes on the order of hundreds of microns were grown and extracted from the bulk polycrystalline samples and were sufficient to be used to determine the structure by single-crystal X-ray diffraction. In order to protect the crystals from air and moisture, the selected small crystals were covered with a layer of Paratone-N oil and were attached to the end of narrow glass fibers. These crystals were then mounted on a Siemens SMART CCD diffractometer with Mo Kα radiation (λ = 0.71073 Å) and a graphite monochromater. The SHELXTL software was used to solve the crystal structures which were then refined by least-square methods.

3.2.2 Powder X-ray diffraction

In order to identify the phase of bulk samples as well as to verify the phase purity of bulk samples, powder X-ray diffraction was carried out on all measured samples. To prepare the bulk samples for measurement in the powder X-ray diffractometer, they were first ground into fine powders using a mortar and pestle and placed onto silicon zero background flat holders. A Panalytical X'pert Diffractometer with $\theta - \theta$ geometry and a monochromatic Cu Kα (λ = 1.54178 Å) radiation source was used. The powder patterns were matched either to those of known compounds by utilizing

databases or to patterns calculated from data obtained from single-crystal X-ray diffraction.

3.2.3 Electron microprobe analysis

As part of the process of identifying new phases, chemical analysis was performed on bulk and single-crystalline samples by using a scanning electron microscope with energy dispersive spectroscopy (EDS) capabilities (JEOL 8600 electron microprobe at the Texas Center for Superconductivity at the University of Houston). The chemical analysis is particularly important when multiple phases are intially present in a single batch of bulk polycrystalline sample. By utilizing EDS on these types of samples, we were able to determine the stoichiometries of different phases present in bulk samples and use the information to grow pure samples of those different phases. To prepare the samples for chemical analysis using SEM/EDS, the samples were placed on a graphite disk with a piece of carbon tape attached to it. Because all of the samples measured were conducting, there was no need to perform carbon coating to avoid charge accumulation.

3.3 Physical properties characterization

3.3.1 Magnetic susceptibility

The magnetic measurements in this work were carried out using either the Quantum Design Magnetic Property Measurement System (MPMS) or the Physical Property Measurement System (PPMS) with a home-made compensated-coil mutual inductance setup (Figure 3.1). Measurements below 2 K down to 400 mK were performed using the PPMS ^{3}He insert (see Figure 3.2 for a schematic drawing of a helium-3 refrigerator). To detect superconductivity, the sample is first cooled down below the transition temperature and then a magnetic field is applied ("zero-field cooling"). When the magnetic field is applied below the transition temperature in a superconductor, a screening current generates an opposing magnetic field such that the magnetic field inside the superconductor is zero. The temperature is raised above the transition temperature so that the magnetic field penetrates the material, and then the temperature is again lowered below the transition temperature ("field-cooling") to examine the Meissner effect.

3.3.2 Electrical transport

Electrical transport measurements were carried out using the conventional 4-wire measurement to reduce the influence of lead resistance on the measurements. When measuring very small resistances, as is the case with superconductors, it is important to employ this method. Contact resistances are often on the order of a few Ω,

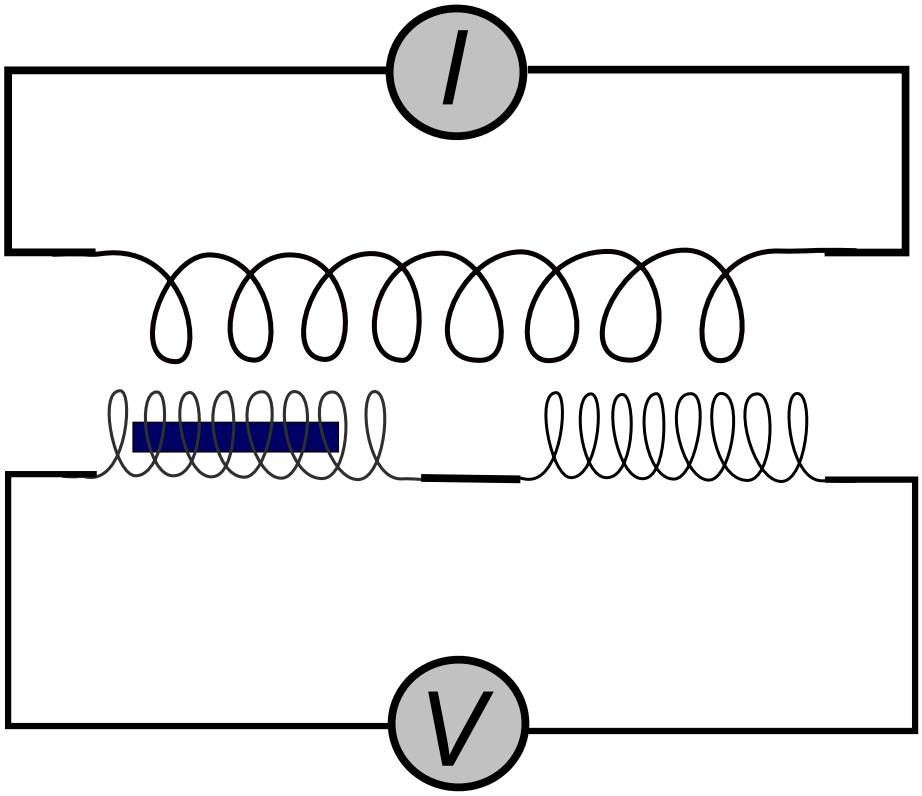

Figure 3.1: Schematic drawing of mutual inductance coil setup. Primary coil is shown on top, two oppositely wound secondary coils are shown on bottom (sample is placed inside one of the secondary coils).

whereas the typical resistance of a measured sample is on the order of mΩ or less. The typical arrangement of a 4-wire measurement is shown in Figure 3.3. Two leads are connected to either side of the sample to push the current through, and two leads are connected between the current leads to measure the voltage. Although there are still contact resistances for all of these leads, the internal resistance of a voltmeter is typically very high, which prevents any substantial amount of current from passing through it so that it does not distrupt the circuit being measured. Therefore, the voltage drop measured by the voltmeter is dominated by the actual

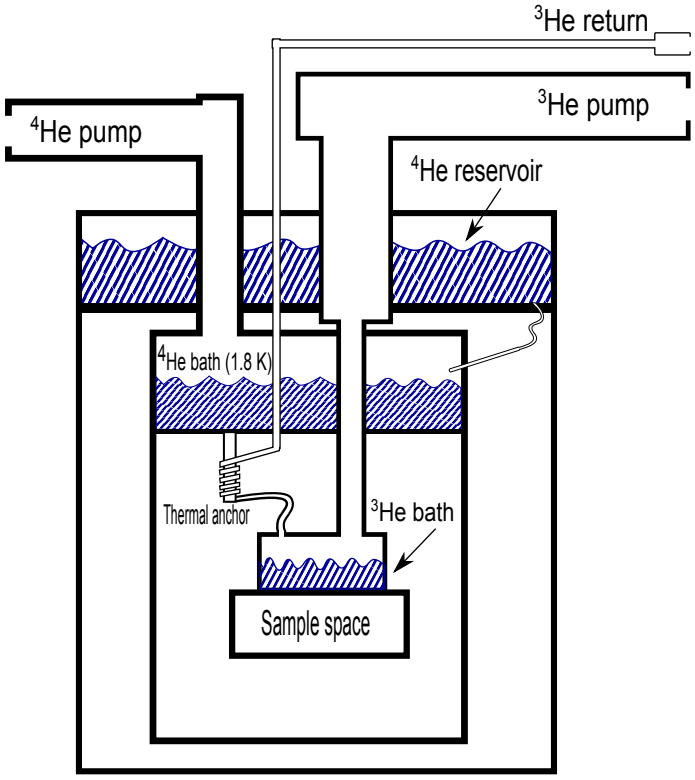

Figure 3.2: Schematic drawing of generic helium-3 refrigerator.

voltage drop across the sample itself.

In this work, all of the electrical transport measurements were carried out using either the Quantum Design Physical Property Measurement System (PPMS) ACT option or using an in-house built probe along with measurement electronics. Measurements down to 400 mK were performed using the PPMS ^{3}He insert. The measurment electronics used with the in-house built probe include a Linear Research

LR-400 ac resistance bridge operated at 15.9 Hz, a Keithley 220 current source, and a Keithley 182 nanovoltmeter. Silver paint was used to make contact between the sample and platinum wires which were then connected to the probe being used. Thermal paste was used to ensure proper thermal contact between the sample and the probe.

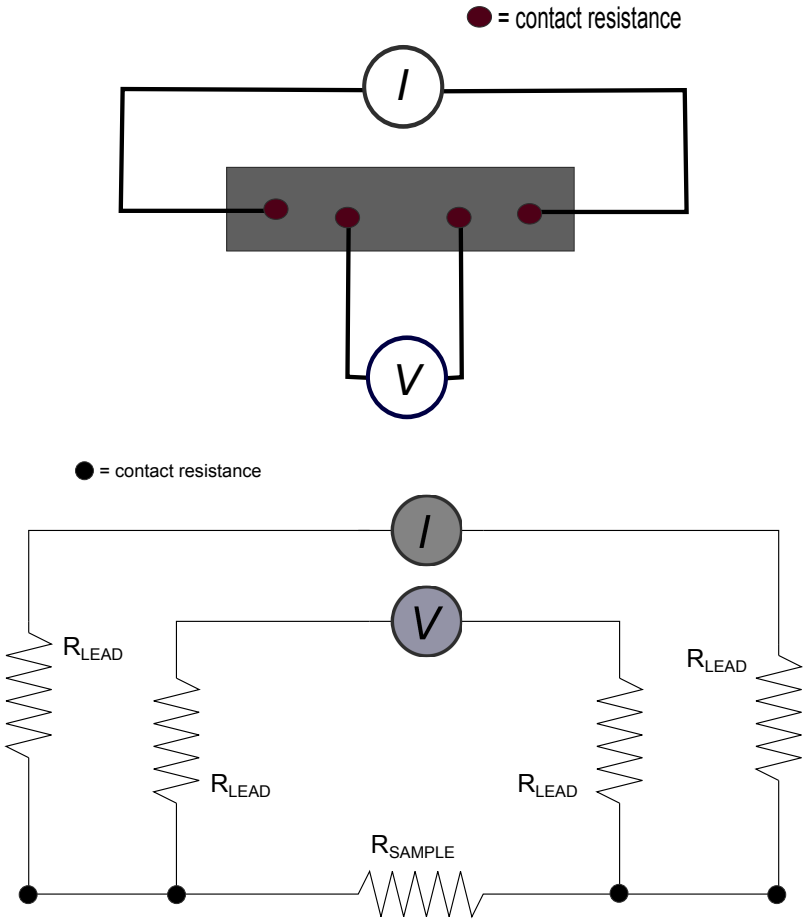

Figure 3.3: (Top) Schematic drawing of typical 4-lead arrangement for resistivity measurements, (bottom) schematic drawing showing lead resistances and sample resistance in 4-wire configuration

3.3.3 DFT calculations

In this work, density functional theory (DFT) calculations were performed to further investigate electronic and vibrational properties of the compounds being studied. The electronic structure calculations were primarily carried out using the Stuttgart TB-LMTO-ASA program, while the charge density calculations were carried out using Quantum ESPRESSO[45].

3.3.4 High-pressure measurements

The application of high physical pressure is a very useful tool in the investigation of superconductivity and other physical properties because of the ability of pressure to tune important parameters such as the size of the lattice, the density of states at the Fermi level, electron-phonon coupling strength, and more, without changing the chemical condition of the sample. Oftentimes, physical pressure can simulate the effects of isovalent chemical doping without the impurities that chemical doping may involve. In this dissertation, high physical pressure is applied to samples using the piston-cylinder type pressure cell technique. Electrical resistivity and magnetic susceptibility can both be measured under high pressure and at low temperatures via this technique.

In this technique, the sample is immersed in a hydrostatic or quasi-hydrostatic pressure medium and confined within a teflon “cup” which is sealed by a beryllium copper (BeCu) “cap” which has an electrical feedthrough. The electrical feedthrough is made using stycast, an epoxy which has excellent performance under high pressure

and repeated thermal cycling. Care must be taken to prepare the stycast epoxy without air bubbles or inhomogeneity to avoid a collapse under pressure. The teflon "cup" along with the BeCu "cap" and electrical feedthrough are placed inside of a hardened BeCu cylinder with a through-hole the same diameter as the teflon container. Pistons are then brought from above and below the teflon container, separated from the teflon container by small BeCu rings. The piston "above" the teflon container (as shown in Figure 3.4 (top)) has a through-hole to allow the electrical connections to pass through to the measurement electronics. The piston "below" the teflon container (as shown in Figure 3.4 (top)) is "pushed" into the teflon container by a BeCu cylinder under the applied force from a hydraulic press. As the force is applied and the piston moves, squeezing the teflon container and increasing the pressure, the screw cap (at the bottom of Figure 3.4 (top)) is tightened. Therefore, when the force is released, the screw cap keeps the teflon container from expanding and locks in the pressure. The pressure medium used throughout this dissertation is Fluorinert77. Figure 3.4 (bottom) shows a scale drawing of the pressure cell setup with all of the interior components assembled, without the screw top. All of the BeCu caps, teflon cups, and BeCu rings are machined for each pressure run using a lathe. The temperature is measured by means of a thermocouple which is inserted near the sample in the teflon container through the electrical feedthrough, and by means of a germanium resistor which is embedded in the wall of the BeCu clamp cell. The thermocouple is typically used for temperatures above 50 K, and the germanium resistor is typically used for temperatures below 50 K.

3.3.5 Heat capacity measurements

Heat capacity measurements in this dissertation were performed using the Quantum Design PPMS Heat Capacity Option. Heat capacity measurements below 2 K were made using the PPMS ^{3}He insert. The heat capacity option measures the heat capacity by applying a small amount of heat to the sample and measuring the resulting temperature versus time. This measurement yields the heat capacity at constant pressure, $C_p = \left(\frac{dQ}{dT}\right)_p$.

In order to thermally isolate the sample while being able to apply heat and measure the temperature, a specially designed sample holder is utilized for this purpose. A small sample platform is suspended by eight very small wires which are connected to the body of the sample holder. These eight wires allow for some thermal conduction to the sample holder and also serve as structural support for the sample platform (Figure 3.5 (top)). The wires are connected to a thermometer and heater which are mounted below the sample platform and which serve to apply heat to the sample and accurately measure the temperature of the sample. The sample is placed onto the sample platform with a layer of thermal grease between the sample and platform to ensure good thermal contact. The measurement is performed under high vacuum so that the thermal contact between the sample and the sample puck is dominated by the thermal conduction provided by the eight wires.

In the case of good thermal contact between the sample and the platform (which is the case for the samples studied in this work) a simple model is used to determine the heat capacity from the measured temperature vs. time data. In this “simple

model", the temperature T depends on the time t in the following way:

$$C_{total}\frac{dT}{dt} = -K_w(T - T_b) + P(t)$$

where K_w is the thermal conductance of the small wires which support the platform, T_b is the temperature of the thermal bath (the puck frame in this case), $P(t)$ is the power from the heater, and C_{total} is the combined heat capacity from the sample and the sample platform. A heat pulse is applied at a time t_0 and the temperature is measured as a function of time. The data is fitted with the solutions to the above equation which are exponential functions with time constant τ equal to C_{total}/K.

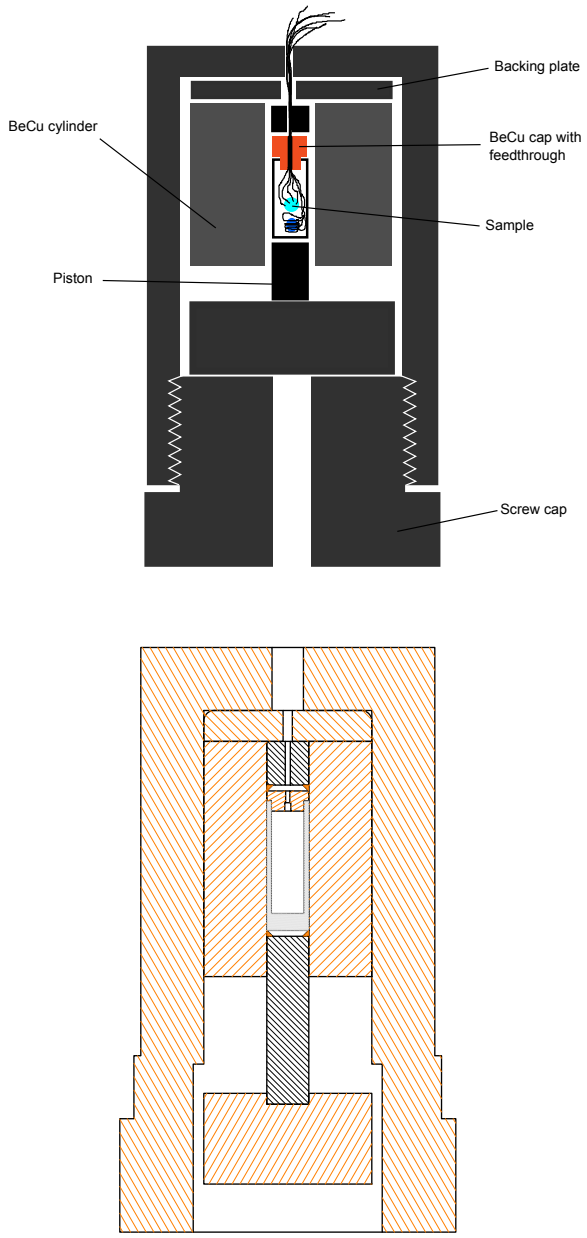

Figure 3.4: (Top) Schematic drawing of high pressure clamp cell. Small blue spheres with wires attached indicate sample and lead monometer; (Bottom) Scale drawing of pressure cell with interior components assembled, shown without screw top.

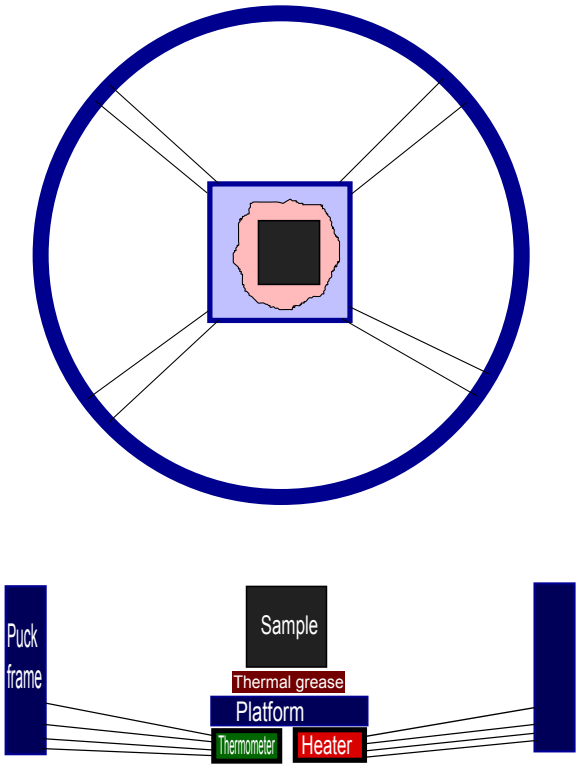

Figure 3.5: Schematic drawing of the PPMS heat capacity option puck.

Chapter 4

Results and Discussion

In this chapter, the results of our investigations into a series of platinum-based superconductors will be presented and discussed. We began our work in this area investigating the recently discovered $SrPt_3P$ which exhibited many interesting properties. In our search for new superconductors in this class of materials, we discovered two new superconductors with new stucture types, also with Sr-Pt-P compositions. Together, these three superconductors form a group of materials with both shared structural features and diverse superconducting properties. All three of these superconductors are composed of "building blocks" which are polyhedra containing one phosphorus atom surrounded (coordinated) by 6 platinum atoms, as shown in Figure 4.1. The exact nature of how these building blocks are arranged and their specific geometry is different in each of these three compounds, and the transition temperatures vary dramatically from 8.4 K down to 600 mK. In this work, a series of systematic experiments has been carried out on these compounds

measuring key properties such as magnetic susceptibility, electrical resistivity, and specific heat, as well as employing techniques such as the application of high physical pressure, in order to better understand the dramatically different superconducting properties of each of these three compounds.

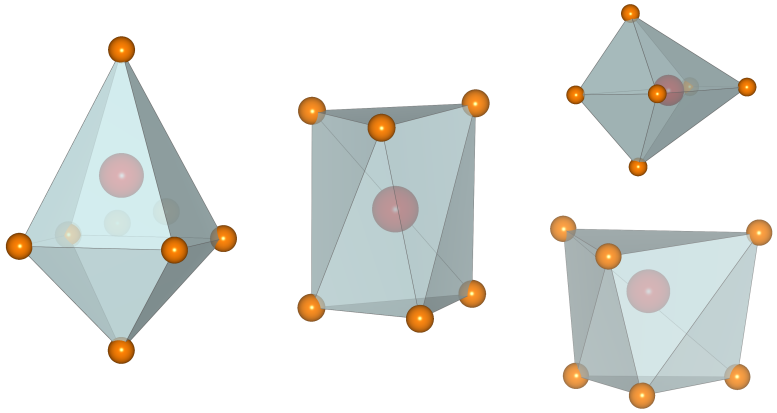

Figure 4.1: Pt_6P building blocks found in (left) $SrPt_3P$, (middle) $SrPt_6P_2$, (right) $SrPt_{10}P_4$.

4.1 $SrPt_3P$

4.1.1 Introduction

Since the discovery of superconductivity in magnesium diboride in 2001[19], strong-coupling electron-phonon type superconductivity has gained increasing interest due to renewed hope for high transition temperatures in this type of superconductor[46, 47, 48, 49]. One can see, qualitatively, why superconductors with stronger electron-phonon coupling are of interest by examining the BCS expression for the transition temperature:

$$T_c = \Theta_D \exp\left[-\frac{1}{N(0)V}\right]$$

At first glance it appears from inspecting this equation, because of the prefactor Θ_D, that decreasing the phonon frequencies would generally decrease the transition temperature. However, this relationship is not so simple. Because the interaction strength V also depends on the frequency of the phonons involved in superconductivity, a decrease in the frequency of phonons which are involved in electron-phonon pairing would tend to increase the T_c, and vice-versa.

Given a particular compound, one way in which to attempt to modify the transition temperature is through chemical doping by partial substitution of one element with another. This type of modification may change the T_c by changing the density of states at the Fermi level, $N(E_F)$, by chemical pressure [50], or by both. A suitable choice of replacement element can often be chosen to favor one effect

over the other. For example, isovalent substitution with a smaller element would tend to shrink the lattice while avoiding significant changes to $N(E_F)$. On the other hand, partial replacement with an adjacent atom to the left or right on the periodic table would be expected to have minimal influence based on size-effects and mainly change the number of charge carriers and therefore shift the Fermi level (which may result in a change in $N(E_F)$ depending on the density of states vs. energy).

In this section, the results of our work on the first of the strontium platinum phosphide superconductors, $SrPt_3P$, are presented. The strong dependence of the strong-coupling, relatively high-T_c (≈ 8.4 K) superconductivity on certain structural details is explored. The coupling strength and transition temperature of this compound are tuned by chemical doping and by the application of physical pressure; analysis of the C_p/T anomaly and the transport properties allow separation of the contributions from $N(E_F)$ and V. The change in T_c is shown to be driven by a strong sensitivity of the interaction strength V to the local rigidity. Later, in Section 4.2, the low-T_c superconductivity of $SrPt_6P_2$ is examined in comparison and sheds further light onto the strong-coupling in $SrPt_3P$.

Outline The remainder of this section is as follows. First, an introduction to the previous work on $SrPt_3P$ and a motivation for our initial study will be given. Then, the experimental results from chemical doping of $SrPt_3P$ will be discussed. The results of our high pressure study on $SrPt_3P$ will then be discussed, followed by a discussion of our specific heat study of chemically doped $SrPt_3P$. Finally, a summary will be given.

4.1.2 Motivation

In 2012, Takayama and coworkers discovered a new platinum-based phosphide superconductor, $SrPt_3P$, with a critical temperature of 8.4 K[36]. This compound crystallizes in an anti-perovskite type structure with a tetragonal unit cell. The crystal structure is very similar to that of the noncentrosymmetric, heavy-fermion superconductor $CePt_3Si$ which is composed of distorted, polar octahedra which line up in the same direction resulting in a breaking of inversion symmetry[29]. The building blocks of $SrPt_3P$ are also distorted octahedra; however, in this case they are aligned in an antipolar arrangement where centrosymmetry is maintained.

From measurements of the specific heat, $SrPt_3P$ was determined to be a strong-coupling superconductor with $2\Delta_0/k_BT_c \sim 5$[36]. This value is much higher than the weak-coupling BCS ratio of 3.52[36]. Such a high value of $2\Delta_0/k_BT_c$ is not common and there are a limited number of examples including the A15 compounds[51], the Chevrel-type compounds[52], the pyrochlore-osmates[53, 54], and the Pb-Bi alloy[36]. Furthermore, deviation from linearity at low temperatures of C/T vs. T^2 was cited as possible evidence for very low-energy phonons in this compound[36]. The Hall resistivity was observed to be highly dependent on both temperature and magnetic field which suggests the possibility of multiple Fermi surfaces in this compound. Strontium was also replaced with both calcium and lanthanum. The T_c for $CaPt_3P$ is 6.6 K and that of $LaPt_3P$ is 1.5 K[36]. Interestingly, in the case of $CaPt_3P$ the electronic specific heat coefficient γ was found to be 17.4 mJ/molK^2, compared to 12.7 mJ/molK^2 observed for $SrPt_3P$, and 6.7 mJ/molK^2 observed for $LaPt_3P$ (Figure 4.5). The electronic specific heat coefficient γ is related to the density

Table 4.1: Structural parameters for $SrPt_3P$[36]

Atom	Site	x	y	z
Pt(1)	4e	1/4	1/4	1/2
Pt(2)	2c	0	1/2	0.1409(3)
Sr(1)	2a	0	0	0
P(1)	2c	0	1/2	0.7226(16)

Axis	Length
a	5.8094(1) Å
b	5.8094(1) Å
c	5.3833(2) Å

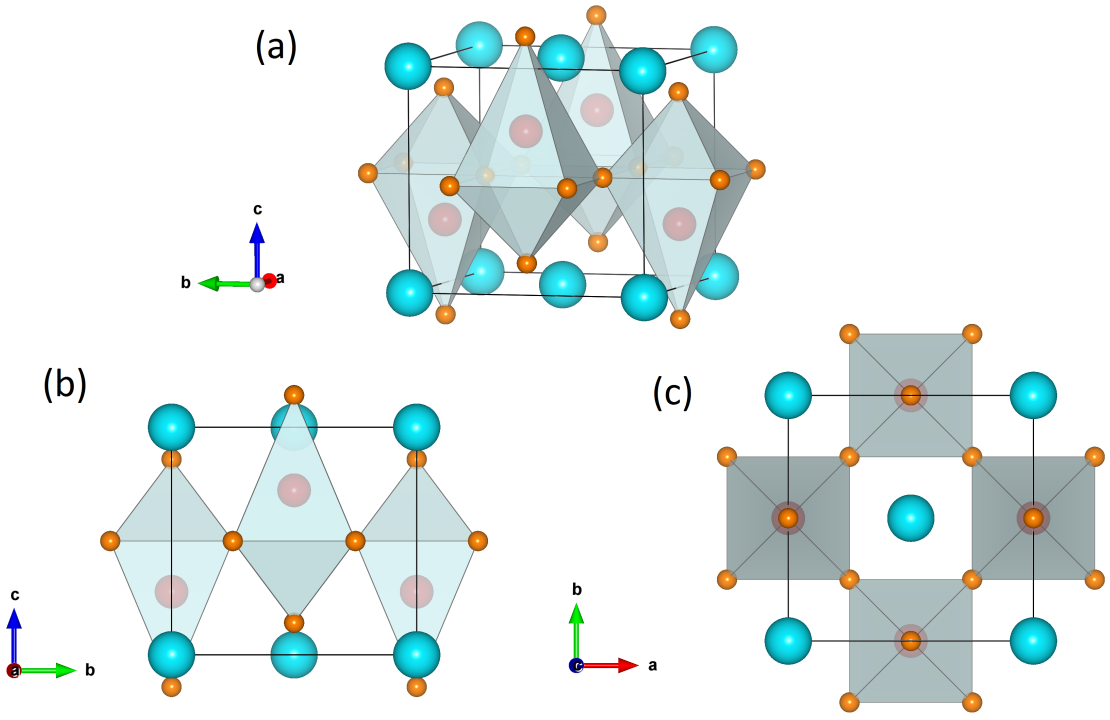

Figure 4.2: Crystal structure of $SrPt_3P$. (a) Perspective view, (b) view along a-axis, (c) view along c-axis

of states at the Fermi level by the following relation: $\gamma = \frac{2\pi^2 k_b^2}{3} N(0)$. According to this observation, the T_c does not scale with the density of states in $SrPt_3P$.

Several theoretical works followed the initial discovery of $SrPt_3P$ to describe the details of the electronic and vibrational properties of this new compound and its Ca and La analogues. Kang et al. and Subedi et al. both carried out density functional theory calculations of the electronic band structure and the phonon properties in APt_3P[55, 56]. They observed a peak at low frequencies in the phonon density of states (Figure 4.4) due to the low-energy in-plane "breathing" modes of the Pt(I) ions which form a square-planar configuration as shown in Figure 4.2 and in Figure 4.3. These low-energy "breathing" phonons might be coupling with the in-plane Pt(I)-P antibonding electronic states, resulting in the relatively high T_c for $SrPt_3P$[55].

Nekrasov et al. performed density functional theory band structure calculations in the Local Density Approximation (LDA) and plotted the density of states vs. energy for APt_3P. Their calculated electronic density of states shows that the Fermi level lies on a negative slope in the density of states (Figure 4.6). They proposed that the suppression of T_c in $LaPt_3P$ and can be explained by possible electron doping which may cause the shift of the Fermi level to higher energy and a decrease in the DOS at the Fermi level[57]. This, however, does not explain the decrease in T_c of $CaPt_3P$, which was experimentally observed to have a higher DOS at the Fermi level. Furthermore, Nekrasov et al. suggest that hole-doping the system would cause a shift of the Fermi level towards lower energy and therefore increase the DOS at the Fermi level and possible increase the T_c of the system.

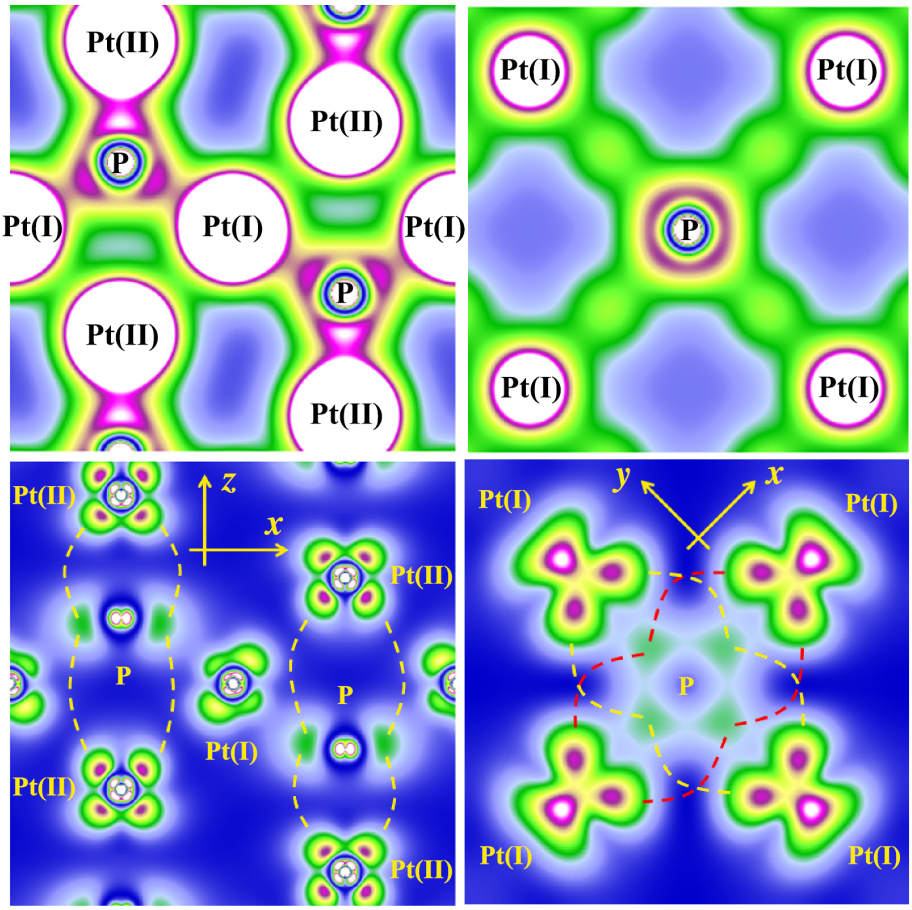

Figure 4.3: Charge density calculations on $SrPt_3P$. (Reproduced from [55]).

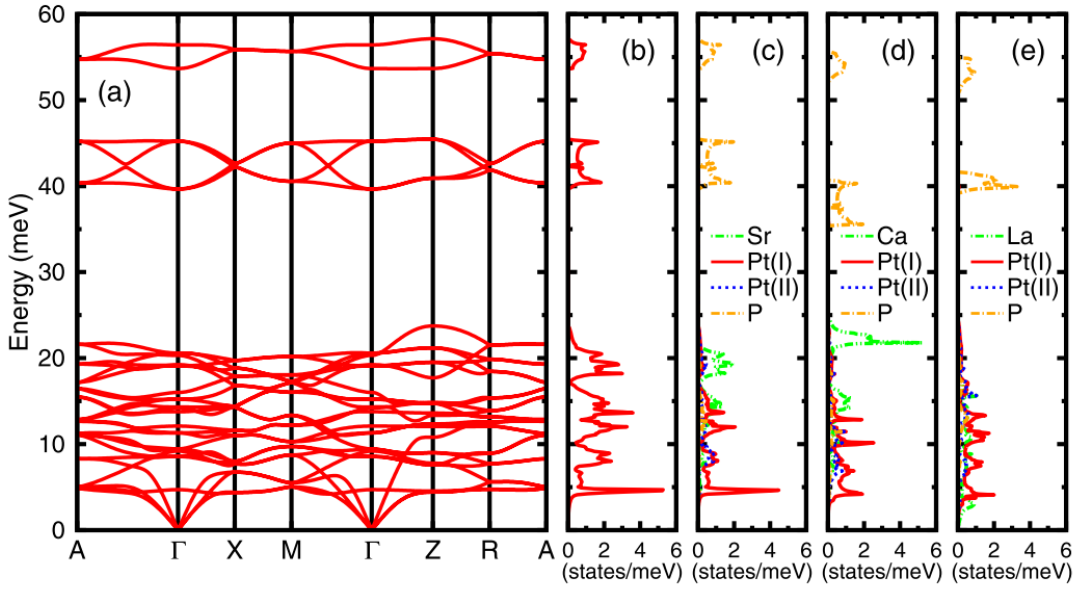

Figure 4.4: Phonon dispersion of $SrPt_3P$ with total phonon DOS and partial phonon DOS for (a) Sr, (b) Ca, (c) La analogues. (Reproduced from [55]).

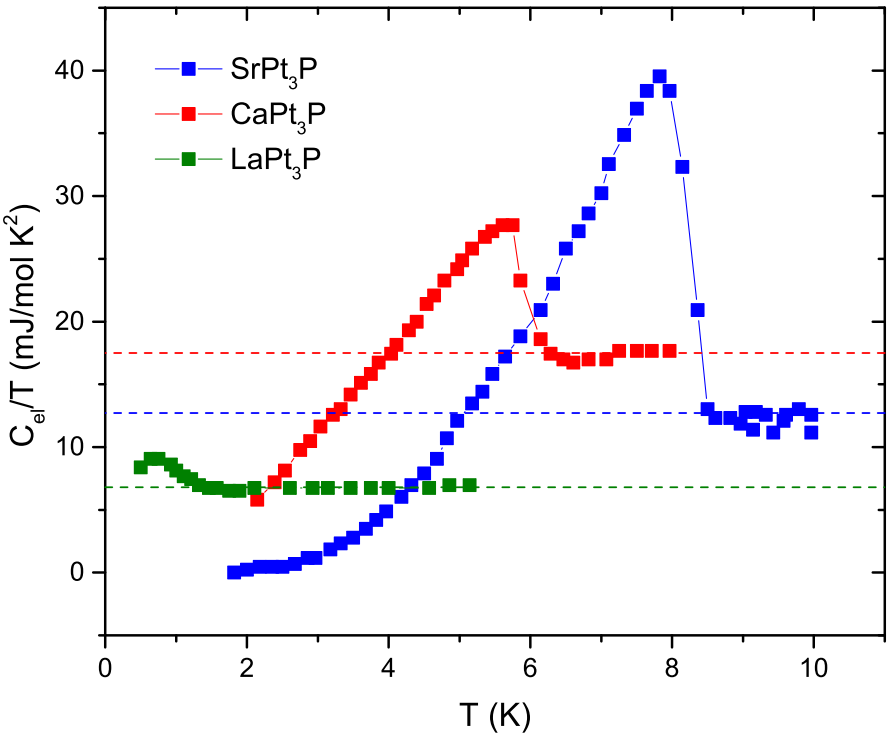

Figure 4.5: Specific heat data for Sr, Ca, and La analogues of APt_3P [Reproduced from [36]].

Therefore, we were motivated to answer the following related questions: is the apparent non-scaling of T_c with the electronic density of states in $SrPt_3P$ confined to only replacement of Sr with La and Ca, or could it be generalized to other elements and sites? If the electronic density of states is not responsible for the shift in T_c, what is?

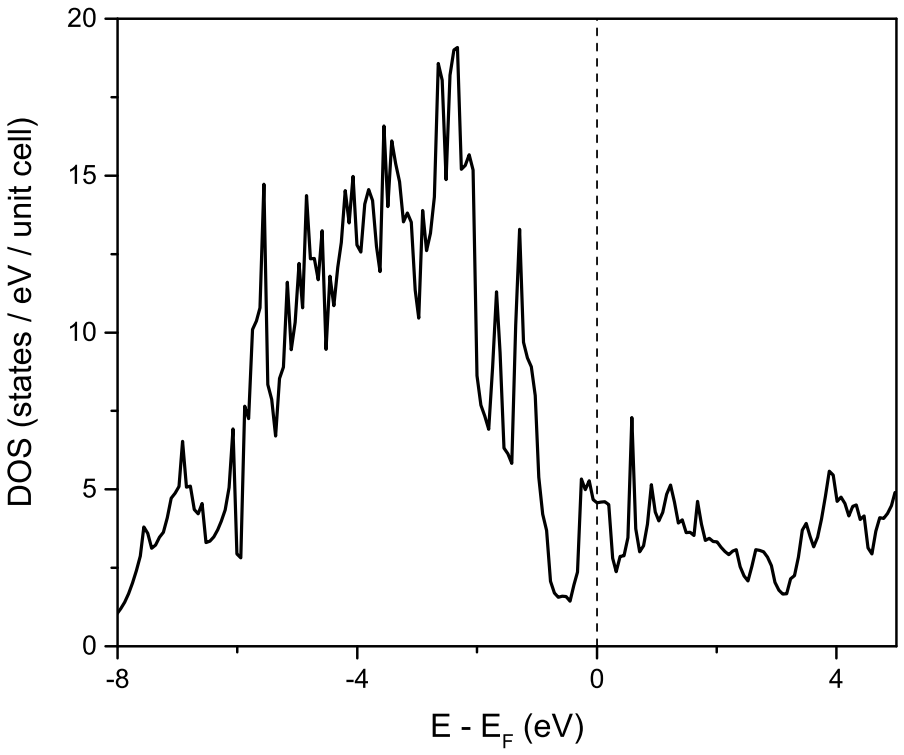

Figure 4.6: Density of states from DFT calculations for $SrPt_3P$ [Calculated following [57]]

4.1.3 Chemical doping

We decided to begin investigating the properties of $SrPt_3P$ by chemically doping the system. There are four crystallographic sites in $SrPt_3P$, which are occupied by Sr, P, Pt(I), and Pt(II). The Pt(I) ions, as mentioned above, are arranged in a square-planar configuration, and occupy half of the vertices of the distorted octahedra. The Pt(II) ions sit above and below the P atoms, and occupy the other half of the vertices. These octahedra are corner shared at all corners and form a network in three dimensions. This network forms cavity sites which are occupied by the Sr ions. The phosphorus ion occupies the crystallographic position within the distorted octahedra and is coordinated by the six surrounding platinum ions. One choice of site to chemically dope would be the Sr site. In their work, Takayama et al. totally replaced Sr with Ca and La[36]. Therefore, one could imagine hole doping into the Sr site with K. However, there is a significant size difference when going from column II to column I of the periodic table. For example, Sr has a crystal ionic radius of 1.58 Å when 12-coordinated[58], as is the case in $SrPt_3P$. In the same case of 12-coordination, La and Ca have crystal ionic radii of 1.5 Å and 1.48 Å, respectively, compared to 1.78 Å for 12-coordinated K[58]. We decided to pursue a different approach and dope into the P site. A brief examination of the nieghborhood of P on the periodic table reveals a limited number of options. Phosphorus is 6-coordinated by the neighboring Pt ions, and has a crystal ionic radius of 0.52 Å. Nearby elements with one less valence electron are C, Si, and Ge. Of these three candidates, Si is closest in size to P. Therefore, we decided to partially replace P with Si, which has a 6-coordinated crystal ionic radius very close to that of P at 0.54 Å[58].

The parent compound $SrPt_3P$ was synthesized by standard solid-state synthetic methods following the procedure reported by Takayama et al. The general procedure is described in Section 3.1.1 of this thesis. The X-ray powder pattern obtained, shown in Figure 4.7, is rather pure, as evidenced by the matching of almost all peaks to the structure proposed by Takayama et al. The relatively good quality of the sample was further verified by the rather sharp resistivity drop of the superconducting transition. The width of the resistive transition at 90% of the drop is $\sim$ 0.31 K, and the diamagnetic shielding is $\sim$ 1.3 (without demagnetization corrections) as showin in Figure 4.8. The large difference between the field-cooled (FC) and zero-field-cooled (ZFC) data suggests type-II superconductivity with possible strong field pinning.

To verify whether Si successfully doped into the P site, we performed powder X-ray diffraction measurements on both the parent compound and 20% Si-doped compound. The XRD spectrum of these two samples are compared with each other in Figure 4.9. That Si is actually going into the P site is indicated by the shifting of the X-ray diffraction peaks as shown in the inset of Figure 4.9. The shifting of the peak corresponds to a shrinking of the lattice by $\sim$ 0.1%. The change is not isotropic, however, which will be discussed towards the end of this section. Higher Si doping in $SrPt_3P_{1-x}Si_x$ with $x = 0.4$ and 0.6 has also been carried out. A clear systematic decrease of the transition temperature is observed through the highest doping level, $x = 0.6$. At low levels of doping, the decrease of T_c is linear, and only begins to deviate from linearity at higher doping levels. Our XRD results clearly show a phase separation with the impurity phase increasing with x, which explains the deviation

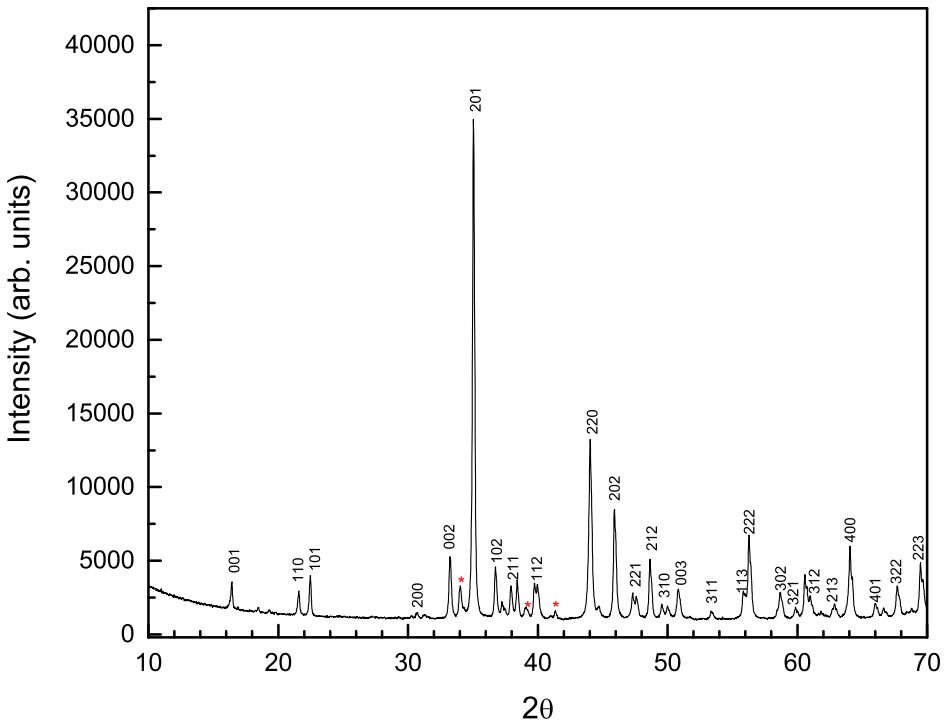

Figure 4.7: X-ray diffraction pattern obtained for bulk polycrystalline $SrPt_3P$. Peak are annotated according to miller indices and small * marks indicate impurity peaks

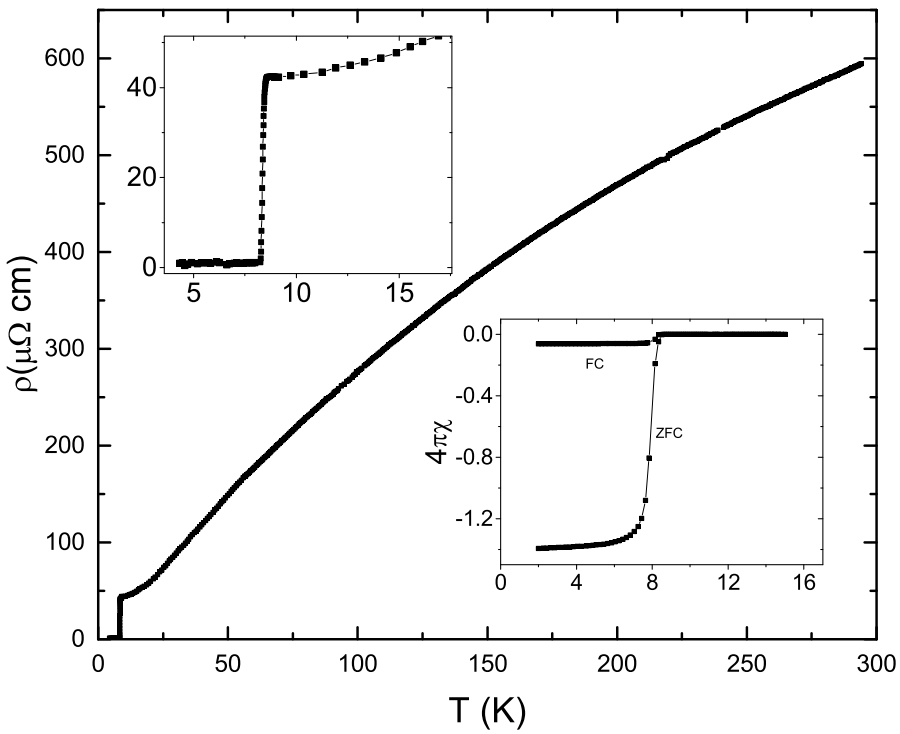

Figure 4.8: Temperature-dependent resistivity and magnetic susceptibility of $SrPt_3P$. Inset (top left): The narrow resistive transition in an enlarged temperature scale from 0 to 20 K. Inset (bottom right): The magnetic susceptibiliy in ZFC and FC modes

from linearity observed in the plot of T_c vs. x (Figure 4.11). Furthermore, this trend can be observed from the decrease in diamagnetic shielding fraction with increasing Si doping beyond 20% as shown in Figure 4.10. It is clear from these data that Si can replace P up to 20% without inducing an impurity phase.

From our resistivity measurements, we observe a suppression of superconductivity with a magnetic field of 3 T to below the lowest temperature measured (Figure 4.12).

4.1.4 Heat capacity

Bulk superconductivity was established in both the parent compound $SrPt_3P$ and the sample with 20% Si, $SrPt_3P_{0.8}Si_{0.2}$, by measuring the specific heat of both the parent compound $SrPt_3P$ and the sample with 20% Si, $SrPt_3P_{0.8}Si_{0.2}$. We apply the α-model[43, 44] to extract further information from the calorimetric data, which extends BCS theory by introducing a variable parameter $\alpha = \Delta_0/k_BT_c$. Subtracting the normal state specific heat C_N (achieved by applying 7T magnetic field) from the superconducting state, we can arrive at a plot of $\Delta C/T$ vs. T (Figure 4.13). From this plot (knowing that the actual value of $\gamma = \Delta C/T - C_{el}(T)/T$ must lie between the lowest measured value of $\Delta C/T$ and the 0 K α-model value) we can estimate the normal state γ values for both samples. For the x = 0 sample, we find $\gamma = 6.31 \pm 0.10$ mJ/mol $\cdot$ K^2, and for the x = 0.2 sample we find $\gamma = 7.77 \pm 0.73$ mJ/mol $\cdot$ K^2. We arrive at $\alpha = 2.4$ for x=0 and $\alpha = 2.2$ for x=0.2. From this information we can extract $\Delta_0 = 1.65$ meV for $SrPt_3P$, which is agreeable with the report of $\Delta_0 = 1.58$

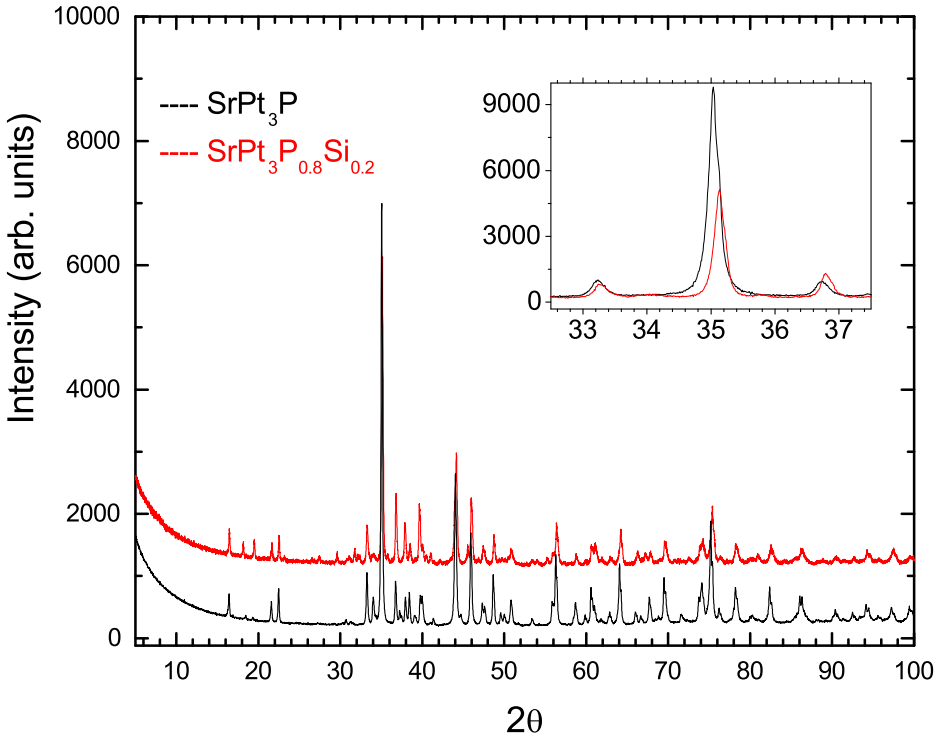

Figure 4.9: X-ray diffraction patterns for $SrPt_3P_{1-x}Si_x$ with x=0 and x=0.2

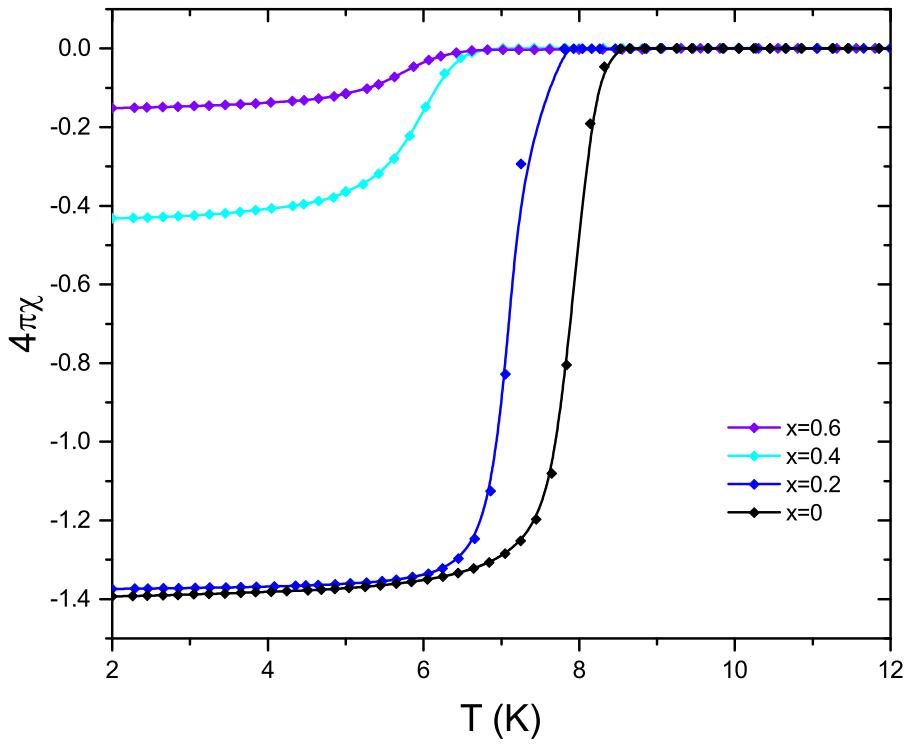

Figure 4.10: Zero-field-cooled magnetic susceptibility vs. temperature for $SrPt_3P_{1-x}Si_x$ samples with x = 0, 0.2, 0.4, and 0.6

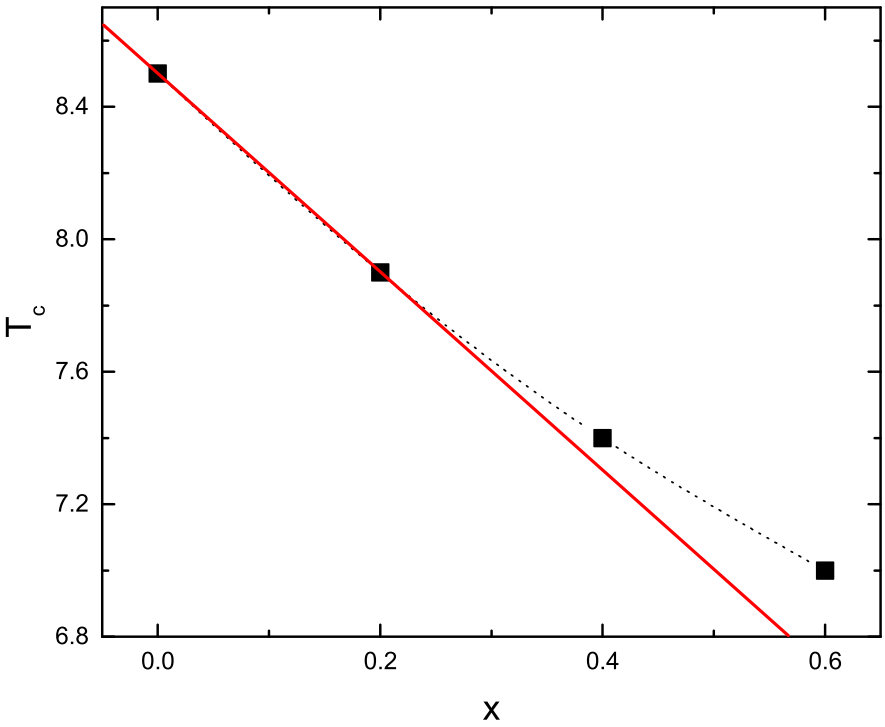

Figure 4.11: T_c vs. x for $SrPt_3P_{1-x}Si_x$

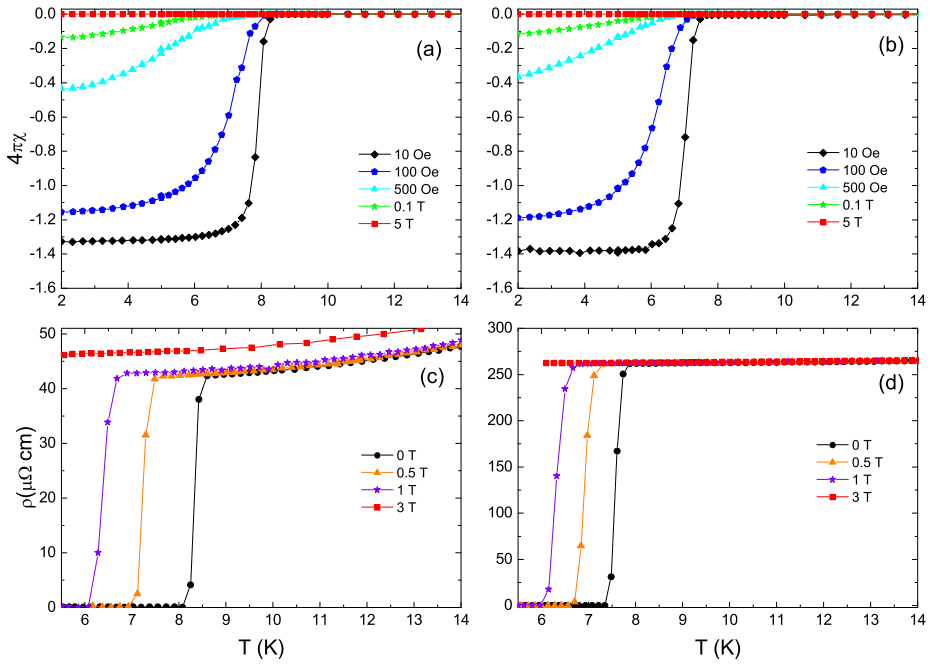

Figure 4.12: Top: Magnetic susceptibility vs. temperature at different magnetic fields for (a) $SrPt_3P$ and (b) $SrPt_3P_{0.8}Si_{0.2}$; resistivity vs. temperature with different magnetic fields is applied for (c) $SrPt_3P$ and (d) $SrPt_3P_{0.8}Si_{0.2}$

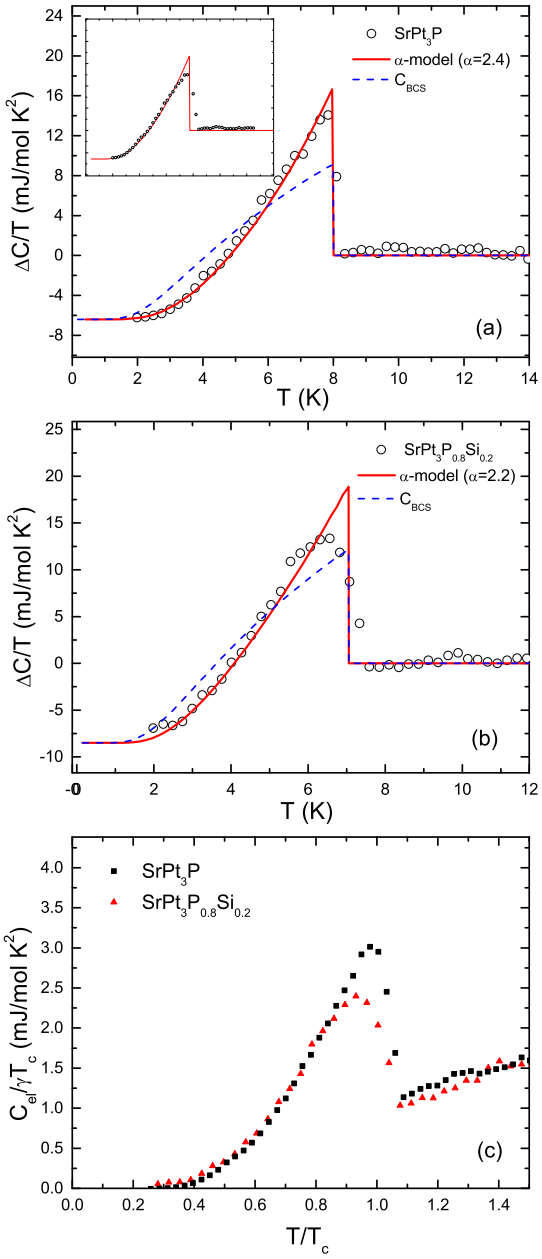

Figure 4.13: $\Delta C/T$ vs. T for (a) $SrPt_3P$ and (b) $SrPt_3P_{0.8}Si_{0.2}$. (c) $C_{el}/\gamma T_c$ vs. T/T_c for both $SrPt_3P$ (broadened) and $SrPt_3P_{0.8}Si_{0.2}$. The red lines represents the α-model, and the blue lines represents the BCS-theory. Inset: $\Delta C/T$ vs. T for $SrPt_3P$ with a broadened transition temperature width.

meV by Khasanov et al.[59]; we find $\Delta_0 = 1.28$ meV for $SrPt_3P_{0.8}Si_{0.2}$.

It can be seen from the specific heat data that the T_c of the x=0.2 doped sample is broader than that of the undoped sample. For x = 0.2, the width is roughly 1.0 K, whereas for x = 0, the width is roughly 0.5 K. To verify that the difference in α value obtained from our fitting is not an artifact due to this difference between the samples, we artificially broadened the data of the x = 0 sample by assuming a 20% content with 5% lower T_c. We assume the same temperature dependence below T_c for the lower T_c component. This assumption results in a transition with a width that is the same as the x = 0.2 sample (1.0 K). This modified data is still well-fitted by $\alpha = 2.4$ (Figure 4.13 a inset). Comparing the scaled specific heat $C_{el}/\gamma T_c$ vs. T/T_c (Figure 4.13 c) for the x=0 data and the x=0.2 data with equal transition temperature width, we observe a significant decrease in the specific heat jump $\Delta C/\gamma T_c$ at T_c from ≈ 1.87 for the undoped sample to ≈ 1.36 for the x = 0.2 doped sample[60].

The apparent increase of $N(\epsilon_F)$ with Si doping is in agreement with previous electronic structure calculations showing the Fermi level located on a negative slope in the density of states[57]. However, our simultaneous observation of a decrease in the transition temperature from ~ 8.4 K in the undoped parent compound to $\sim$ 7.8 K in the 20% Si-doped compound is opposing this trend. These observations can be reconciled when taking into consideration the variation in the coupling strength. Our fitting of the data with the α-model indicates that the value of α decreases from 2.4 to 2.2, which translates to a change in $2\Delta_0/k_BT_c$ from 4.8 to 4.4. The

value of α gives us direct information about the magnitude of the superconducting gap parameter, Δ, as is clear from the definition $\alpha = 2\Delta_0/k_B T_c$. Furthermore, we can inspect the following BCS relation to understand the relation between the gap parameter and the coupling strength:

$$\Delta_0 = \frac{\hbar\omega_D}{\sinh(\frac{1}{N(0)V})}$$

From this relation, we can see that while we observe an increase in $N(0)$, our observed decrease of the gap parameter Δ_0 signifies a significant decrease of the interaction strength V. The significance of this result will be discussed in the conclusion of this chapter after the high pressure results are discussed in the following section.

4.1.5 High pressure

We observed in our chemical doping study that, while the transition temperature decreases from ~ 8.4 K in the undoped parent compound to ~ 7.8 K in the 20% Si-doped compound, the density of states at the Fermi level increased by ~ 20%. This raises the question of why the T_c would be so sensitive to the slight compression of the lattice induced by partial replacement of P with Si. As is well-known, the application of high physical pressure can allow us to learn quite a bit about the underlying physics of a material system. For example, compressing the lattice could lead to changes in phonon frequency, density of states at the Fermi level, electron-phonon coupling, and may also induce structural transitions[61, 50]. These effects

can manifest in changes in the transition temperature and can provide us with further insights into the system.

Taking the midpoint of the transition as the superconducting transition temperature, we can clearly see an increase of the superconducting transition from 8.35 K at ambient pressure to a maximum of 8.49 K at a pressure of 9.90 kbars (Figure 4.14). Further application of pressure beyond 9.90 kbars appears to lower the transition temperature, with the highest applied pressure of 17.53 kbars leading to a T_c of 8.47 K. The slope of the superconducting transition changes with increasing pressure, which may be related to the width of the transition. A slight spread in T_c would mean that, at a given temperature within the superconducting transition, part of the sample is below T_c while some parts may not be below T_c. As the pressure is increased, the higher T_c part of the material will reach the maximum T_c and begin to decrease before the lower T_c portion does. This effect leads to the appearance of a sharpening of the transition width near the maximum pressure. In order to verify the reversibility of the trend that we observed, it is useful to take several measurements during the unloading of pressure as well as the loading of pressure. We measured several points during unloading and reversed the process multiple times. Our results show that the observed trend is largely reversible with a minor split (< 0.01 K) between the pressure-increasing and pressure-decreasing branches. Upon unloading to ambient pressure, the T_c does not recover its original value and instead is slightly higher. Irreversible defects may have been introduced to the sample during the course of applying pressure as evidenced by our observation that, upon unloading pressure, the resistivity above T_c is higher than that before loading

(Figure 4.15b).

Our observation of an increase of the T_c up to a maximum value at $\sim$ 9.90 kbars followed by a decrease to lower T_c upon further increase of pressure suggests that there are several competing factors at play. Indeed, the application of physical pressure typically changes multiple parameters simultaneously. In simple (non-transition metal) elemental superconductors, a linear decrease in the transition temperature is typically observed with application of pressure. When pressure is applied, the lattice is compressed, and the bonds are typically stiffened. The result of this stiffening of the lattice is an increase in phonon frequency. The increase in phonon frequency has two simultaneous effects on the transition temperature. First, it can increase the Debye temperature, which is the pre-factor in the BCS relation for T_c. Second, the stiffening of the lattice and resulting increase in phonon frequency can weaken the electron-phonon interaction strength. The latter of these two effects wins out due to the exponential dependence and the T_c decreases[61, 50]. However, there is another effect which can cause an increase in the transition temperature. With the application of pressure, the Fermi level typically increases due to an increase in the number of charge carriers per unit volume. If there is a peak in the density of states near the Fermi level, the shift of the Fermi level induced by the application of pressure will cause a change in the T_c which could be greater than the change caused by the stiffening of the lattice.

To further understand the mechanism taking place in $SrPt_3P$, we decided to apply physical pressure to $SrPt_3P_{1-x}Si_x$ with $x = 0.2$. We observed a systematic decrease of T_c with increasing pressure up to 17.08 kbars (Figure 4.16). This decrease in

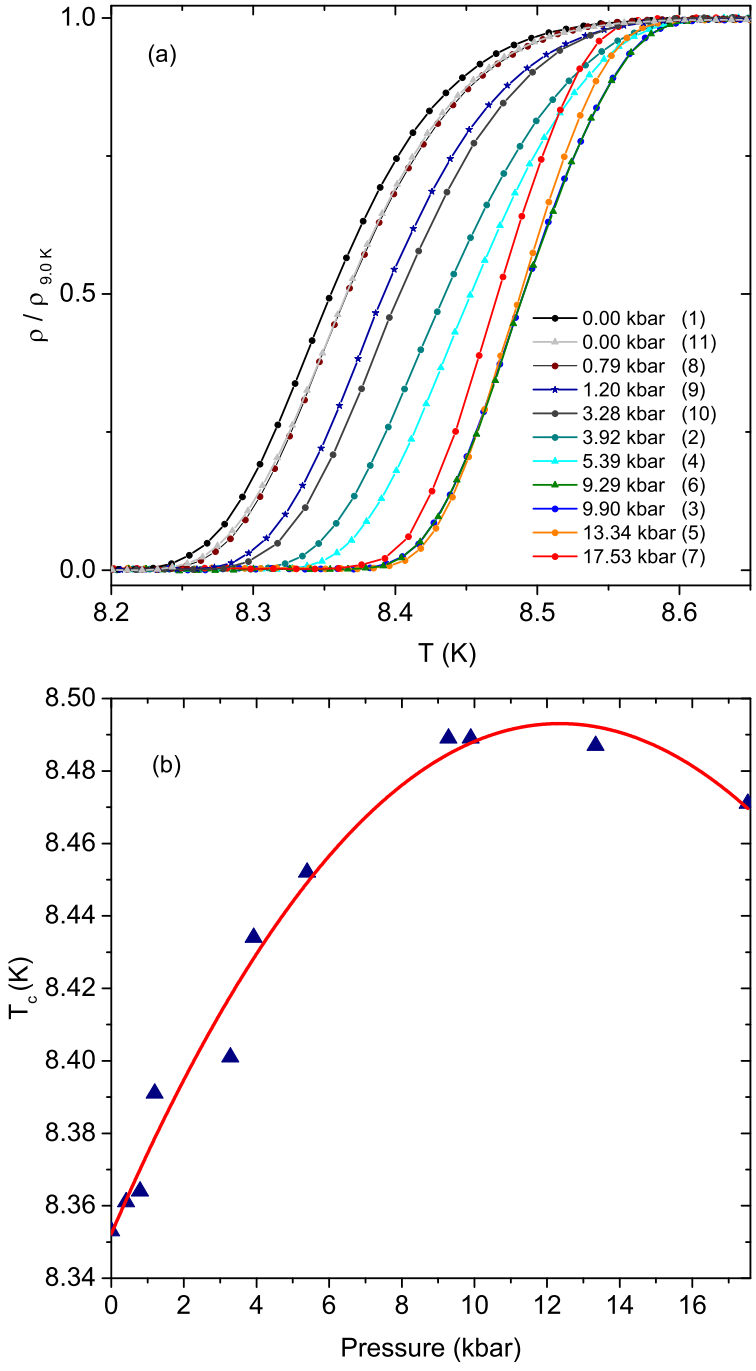

Figure 4.14: (a) Temperature dependent resistivity of $SrPt_3P$ at different pressures, (b) T_c vs pressure

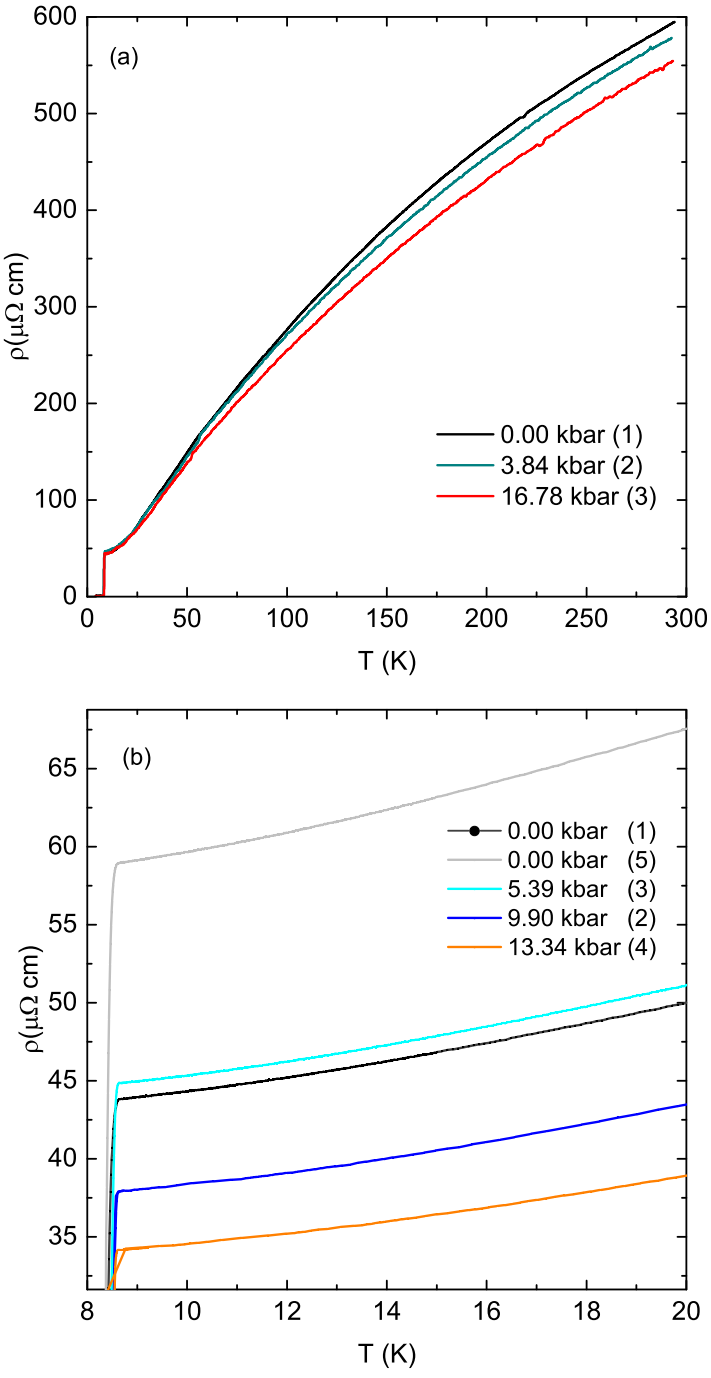

Figure 4.15: (a) Enlarged temperature scale of resistivity vs. temperature near T_c for $SrPt_3P$ at different pressures (the sequential order of runs indicated by numbers in parenthesis), (b) resistivity vs. temperature above T_c for loading and unloading runs

T_c under pressure for the Si-doped sample is in good agreement with our previous results. For the parent compound, $SrPt_3P$, the T_c increases initially because the Fermi level increases under pressure and, because the Fermi level originally lies in a local valley in the density of states, the density of states at the Fermi level increases. Beyond a certain pressure, the density of states begins to flatten again and the stiffening of the lattice and weakening of the electron-phonon interaction begins to dominate, and the T_c begins to decrease.

The decrease of T_c with increasing pressure in $SrPt_3P_{1-x}Si_x$ with $x = 0.2$ can be understood in a similar way. With Si doping, from specific heat measurements, we have observed that the electronic specific heat coefficient γ, and therefore the density of states at the Fermi level $N(E_F)$, increases. This is due to the hole-doping effect which would lower the Fermi level onto the other side of the valley in the density of states, as suggested by Nekrasov et al.[57]. Therefore, the slope in the density of states at the Fermi level at ambient pressure is negative for $SrPt_3P_{1-x}Si_x$ with $x = 0.2$, as opposed to positive for $x = 0.0$. When pressure is applied, the Fermi level increases, but in this case the increase in the Fermi level causes a decrease in the density of states rather than an increase, resulting in the observed decrease of T_c. This, however, raises another question. If the application of pressure causes the lattice to become stiffer and therefore causes the electron-phonon interaction strength and the T_c to decrease, why does the shrinking of the lattice with Si-doping cause such a large change in T_c compared to the change induced by the application of physical pressure?

This question can be answered by examining the nature of the change of the

lattice in these two different cases. In the case of physical pressure, we have used a hydrostatic pressure medium which would result in a relatively isotropic pressure. This, in turn, would cause the lattice to shrink isotropically. Furthermore, when the lattice is compressed by pressure, the amount of compression of a given axis is distributed more or less evenly among all of the bonds in that particular direction. Therefore, when pressure is applied, most of the bonds are shortened by a small amount. However, with the replacement of phosphorus by silicon, the amount of shrinking that the lattice undergoes is mostly due to a change in the length of the Pt-P to Pt-Si bonding.

Why can this change in the Pt-P bond length, induced by the partial replacement of P with Si, cause such a significant change in the electron-phonon coupling that it can overcome the $\sim$ 20% increase in the density of states at the Fermi level and lead to a systematic decrease in the T_c? To understand this, we need to recall the mechanism for superconductivity in this compound. Based on previous experimental and theoretical works[36, 56, 55], superconductivity occurs because of the coupling of low-frequency "breathing" modes, due to the Pt-P bonding in the a-b plane, to the in-plane Pt(I) d_{xy} - P p_{xy} orbitals. When we take a closer look at our powder X-ray diffraction data, we can extract the change in d-spacing between planes perpendicular (200) to the a-b plane and planes with components parallel to the a-b plane (201) (Figure 4.17). We observe that the change in d-spacing between planes perpendicular to the a-b plane is much stronger than that of other planes. To further verify this, we performed Rietveld refinement analysis of the X-ray diffraction data for undoped and 20% Si-doped samples. The results of the Rietveld refinement

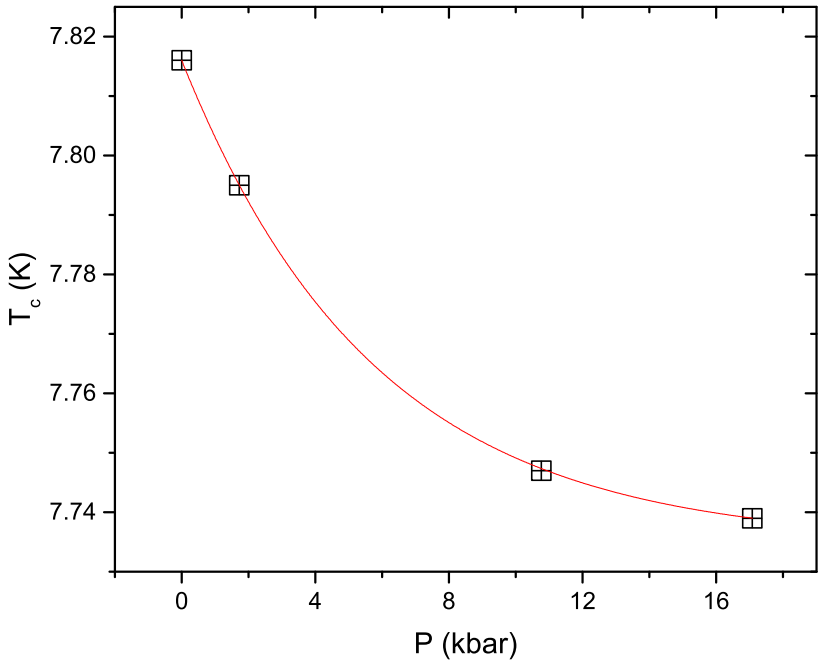

Figure 4.16: Superconducting transition temperature vs. pressure for $SrPt_3P_{0.8}Si_{0.2}$

Table 4.2: Lattice parameters from Rietveld refinement for $SrPt_3P_{1-x}Si_x$ with x=0 and x=0.2 in Angstroms

	a	b	c
x = 0	5.8174(4)	5.8174(4)	5.3741(7)
x = 0.2	5.8050(3)	5.8050(3)	5.3821(7)

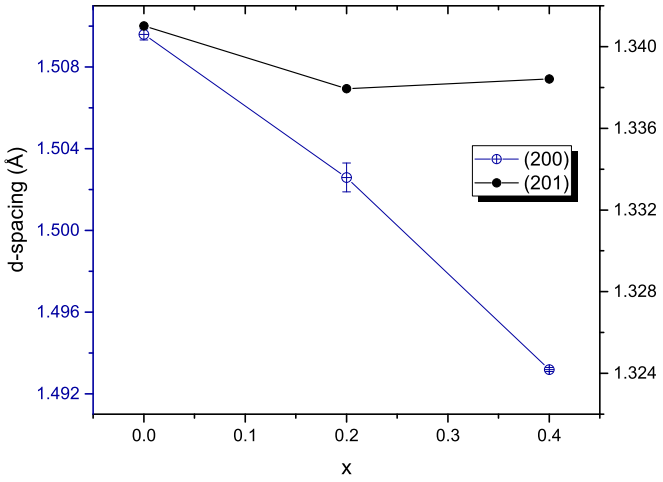

Figure 4.17: The Si-doping dependence of the d-spacing between planes along the (201) and (200) directions

(Table 4.2) support the above analysis and show that the a- and b-axes contract while the c-axis slightly expands. This means that Si doping is not only reducing the Pt-P bond length, it is selectively reducing the Pt-P bond length in bonds along the a-b plane. This makes sense when looking at the crystal structure and examining the octahedral building blocks. The interior of the octahedra is quite crowded, however there is more space along the c-axis direction compared to the space along the a-b plane. Replacing P with Si may slightly "relieve" the crowding of the interior of these octahedra and allow for the Pt(I) ions to move closer, while the Pt(II) ions above and below P already have enough "space". This shrinking of the Pt-P bond length along the a-b plane causes the low-frequency Pt(I)-P "breathing" modes to shift to higher frequency with Si doping, resulting in the observed suppression of T_c.

4.1.6 Summary

We have investigated the superconductivity in $SrPt_3P$ resistively, magnetically, and calorimetrically, including under the application of high physical pressure and with the partial replacement of phosphorus with silicon. The high-pressure investigation yielded the result that the superconducting transition temperature increases by a maximum of approximately 0.14 K upon application of pressure up to 9.90 kbars, with an apparent decrease in T_c beyond that pressure. High pressure systematically decreases the T_c in Si-doped $SrPt_3P$. Contrary to previous predictions[57], hole-doping with Si results in a systematic decrease in T_c, despite

an increase in $\gamma \propto N(E_F)$. Our specific-heat measurements demonstrate the bulk nature of the superconductivity in the parent compound as well as the silicon doped sample with x=0.2; furthermore, we observe a decrese in α as well as $\Delta C/\gamma T_c$, implying that a decreasing interaction strength V may be responsible for the suppression of T_c. Furthermore, we observe an anisotropic change in the lattice d-spacings with increasing Si-doping, with a much stronger decrease of the length of the a and b axes than the c-axis. We propose that this is due to the crowding of the distorted octahedral building blocks of $SrPt_3P$. Because of this geometry and the strong coupling of low-frequency Pt(I)-P phonons to Pt(I) in-plane orbitals, the slight shrinking of the Pt-P induced by replacement of P with Si causes a strong suppression of the electron-phonon interaction strength, as evidenced by the decrease in T_c despite an increase in $N(E_F)$.

4.2 $SrPt_6P_2$

4.2.1 Introduction

Oftentimes, studying related material systems or compounds with different physical properties can lead to further insights into the nature of those materials. Sparked by our investigation of superconductivity in $SrPt_3P$, we became curious to find new materials in the Sr-Pt-P ternary system with different and interesting physical properties. During this investigation, we discovered a new ternary phase, $SrPt_6P_2$, which crystallizes in a new cubic structure with space group number 205, contains unique structural features, and is a weak-coupling superconductor with T_c = 600 mK.

Outline The remainder of this section is organized as follows. The crystal structure of $SrPt_6P_2$ will be described in detail. Calculations of the bonding interactions and their influence on the stability of this structure will be presented and discussed. Then, the superconducting properties of $SrPt_6P_2$ will be discussed. The weak-coupling superconductivity of $SrPt_6P_2$ will then be compared with the strong-coupling superconductivity of $SrPt_3P$. Finally, the work on this compound will be summarized.

Part of this section is reprinted with permission from: Synthesis, Structure, and Superconductivity in the New-Structure-Type Compound: SrPt6P2. Bing Lv, BenMaan I. Jawdat, Zheng Wu, Maurice Sorolla, II, Melissa Gooch, Kui Zhao, Liangzi Deng, Yu-Yi Xue, Bernd Lorenz, Arnold M. Guloy, and Ching-Wu Chu. Inorganic Chemistry 2015 54 (3), 1049-1054. DOI 10.1021/ic502377v

4.2.2 Crystal structure

The fundamental building block in the crystal structure of $SrPt_6P_2$, as in $SrPt_3P$, are the Pt_6P polyhedra with a phosphorus atom 6-coordinated by platinum atoms. Whereas the polyhedra in $SrPt_3P$ are distorted octahedra, the polyhedra in $SrPt_6P_2$ are slightly distorted trigonal prisms. Figure 4.18 shows a perspective view of the crystal structure of $SrPt_6P_2$, and Table 4.3 shows the lattice parameters and atomic positions. The slightly distorted trigonal prisms are formed by two equilateral Pt_3 triangles with P atoms at the centers. The two equilateral triangles which form the trigonal prisms and which consist of three Pt atoms are slightly different from each other. The Pt-Pt bond lengths of these two equilateral Pt_3 triangles are slightly different (2.822(1) Å and 2.828(1) Å), and the Pt-P bond lengths are also slightly different (2.353(5) Å and 2.327(5) Å). Furthermore, the Pt-P-Pt bond angles are different, at 73.7(2)° and 74.9(2)°, respectively. These two parallel Pt_3 triangles do not completely overlap when projected onto each other and are offset by 16.4 ° (Figure 4.19). Together, they form the distorted trigonal prism Pt_6P.

These slightly distorted trigonal prismatic Pt_6P polyhedra are corner-shared, and consequently, a complicated unique three-dimensional framework is constructed in which a total of 12 corrugated Pt_4P_4 rings are formed around one central Pt_6P building block, which is rather similar to the octahedral arrangement observed in the anti-ReO_3 structure[62].

The neighboring Pt_4P_4 rings form an irregular pseudocubic cage that is composed of a total of eight Pt_6P polyhedra. The four Pt_6P polyhedra on each of the six faces

Table 4.3: Structural parameters for $SrPt_6P_2$

Atom	Site	x	y	z
Pt	24d	0.3441(1)	0.1571(1)	0.0790(1)
Sr	4a	0	0	0
P	8c	0.8063(5)	0.1937(5)	0.6937(5)
Axis		Length		
a		8.4740(2) Å		
b		8.4740(2) Å		
c		8.4740(2) Å		

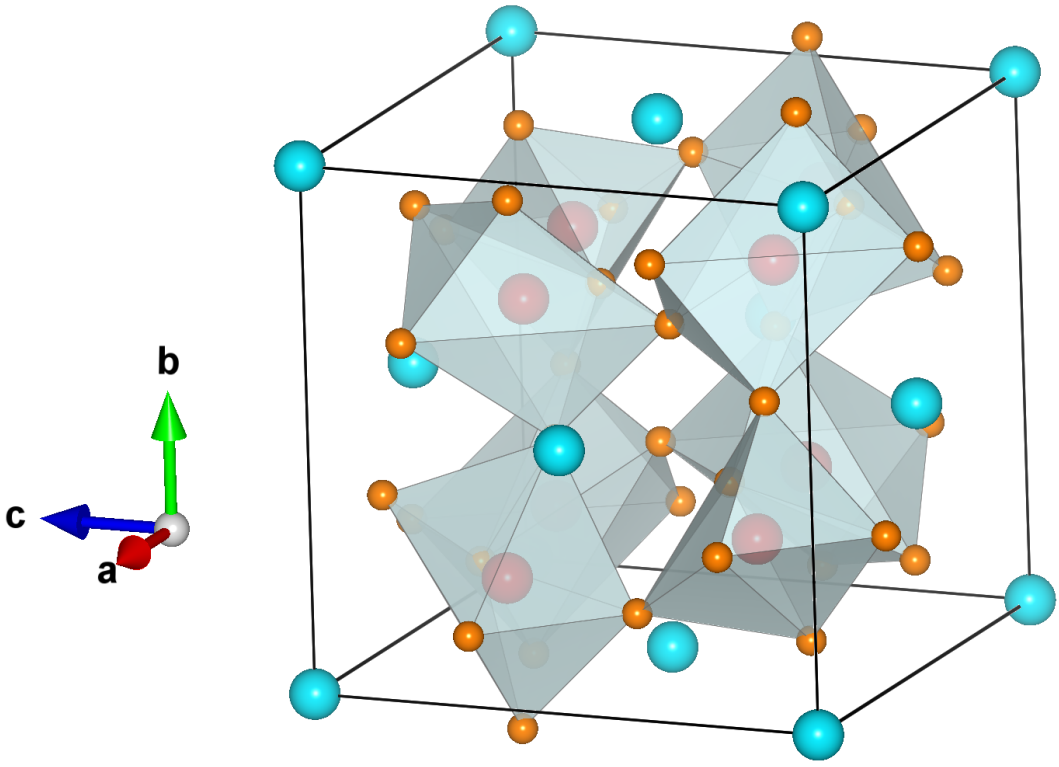

Figure 4.18: Crystal structure of $SrPt_6P_2$ (perspective view)

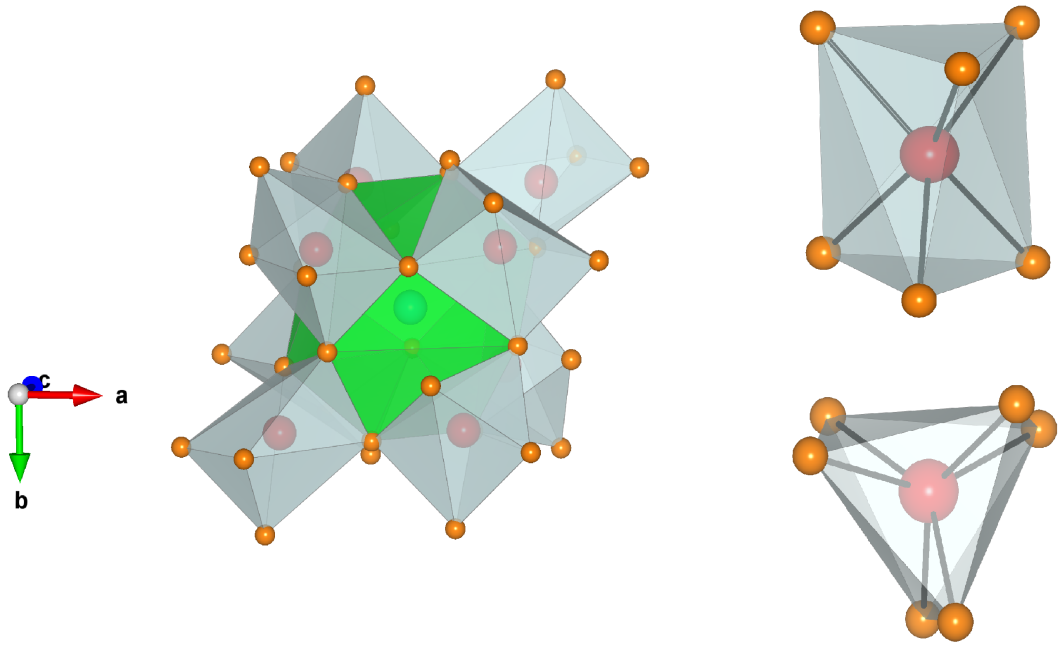

Figure 4.19: Crystal structure of $SrPt_6P_2$. (Left) Cuboctahedron formed by corner-shared Pt_6P trigonal prisms, (Top Right) Side view of trigonal prismatic building block, (Bottom Right) Top view of trigonal prismatic building block

of the pseudocube are all bridged through Pt vertices and form the Pt_4P_4 ring. Therefore, a cavity site, which is equivalent to the A site of the perovskite structure, is created (Figure 4.19). Similar to the coordination number of the perovskite, the Sr atoms sit in the cavity site with a total of 12 nearest-neighbor Pt atoms. The 12 Pt atoms constitute a highly distorted cuboctahedron with six Sr-Pt distances ar 3.2616(8) Å and another six Sr-Pt distances at 3.2742(8) Å. In the extended lattice, each Pt_6P polyhedron is shared by eight neighboring Pt_4P_4 rings and has a formula of $(Pt_{6/2}P)_{8/8} = (Pt_3P)$. The Sr atoms only occupy half of the cavity sites formed by Pt_4P_4 rings alternately and thus have a final formula $Sr_{0.5}(Pt_3P) = SrPt_6P_2$. It is interesting to note that there are only four crystallographic sites for the cubic space group $Pa\bar{3}$ (No. 205): 24d (occupied by Pt); 8c (occupied by P); 4a (occupied by Sr); 4b (another half-cavity site). The cavity site formed at the 4a site has a much larger Pt-Pt distance ($\sim$ 6.5 Å) across the distorted cuboctahedron than the Pt-Pt distance at the 4b cavity site ($\sim$ 3.98 Å) (Figure 4.20). An arbitrary assignment of Sr atom occupation at the 4b site will result in much shorter Sr-Pt ($\sim$ 1.99 Å) and Sr-P ($\sim$ 2.84 Å) distances, which will destabilize the structure.

4.2.3 Bonding analysis

To understand the chemical bonding of the compound, electronic band-structure calculations were performed using the Stuttgart $TB-LMTO-ASA$ program. The density of states (DOS) plots of $SrPt_6P_2$ with projected DOS (PDOS) of the Pt d and P s and p states are shown in Figure 4.21. The calculations show that the compound is metallic, with the Fermi level near or just below a pseudogap. A simple

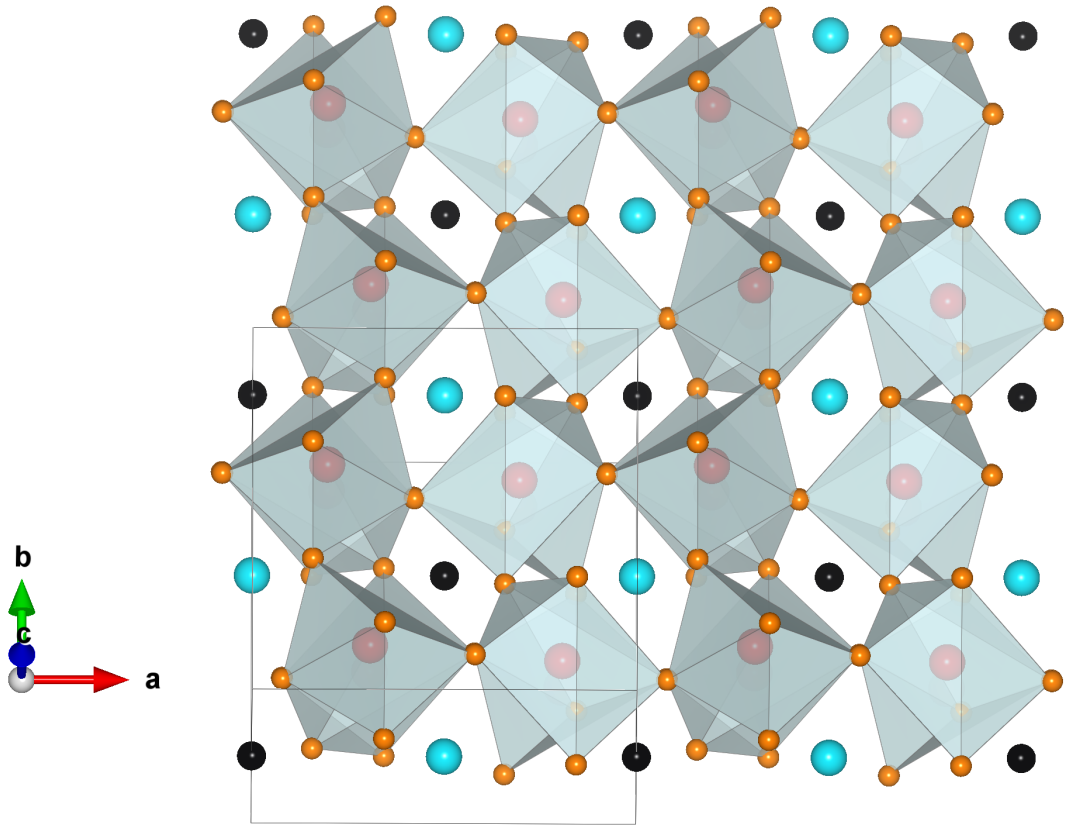

Figure 4.20: Crystal structure of $SrPt_6P_2$. Network of corner-shared Pt_6P trigonal prisms. Black spheres represent vacant cavity sites.

formal electron-counting scheme of Sr^{2+} and P^{3-} ions results in a total formal electronic charge of $[Pt_6]^{4+}$ or $[Pt_3]^{2+}$ for every Pt_3 triangle. This is consistent with the calculated DOS and PDOS, which indicate that phosphorus-derived s and p states are essentially occupied with incompletely filled d bands of the Pt atoms. Studies on the chemical bonding of late-transition-metal polar intermetallics have shown that late-transition metals like Pt usually exhibit negative oxidation states with filling of the d orbitals before the p states of the main-group metalloid[63, 64, 65, 66]. In $SrPt_6P_2$, the p orbitals of P are sufficiently lower in energy and are completely filled. However, the incomplete filling or electron deficiency of the d states of Pt leads to interesting results.

It is useful to further analyze the bonding interaction between individual atoms to better understand why this particular crystal structure, with a significant difference in size between the vacant and occupied cavity sites, is stabilized. Further information can be extracted from the band structure calculations by using a method called crystal orbital Hamilton populations (COHP) analysis[67]. This method is essentially an orbital-overlap weighted density of states. The resulting COHP plots are shown as energy vs. -COHP; positive values of -COHP indicate bonding interactions (orbital overlap) and negative -COHP values indicate antibonding. Integration of the total value below the Fermi level yields the ICOHP which is an indicator of the bonding strength between two atoms. Analysis of the chemical bonding in $SrPt_6P_2$ using the COHP method and the ICOHP clearly indicates that the P-Pt interatomic contacts within the $[Pt_6P]$ trigonal prisms are strongly bonding and essentially optimized interactions (Figure 4.22). However, the COHP plots of Pt-Pt

Table 4.4: Calculated ICOHP values [eV/bond] of relevant interatomic distances in $SrPt_6P_2$

Atom Pair	Length (Å)	ICOHP
Pt-P (6x)	2.327(5) - 2.353(5)	2.77
Pt-Pt (3x)	2.822(1) - 2.828(1)	0.74
Pt-Pt (1x)	2.811(2)	0.49
Pt-Pt (3x)	3.388(1)	0.03

interactions indicate significant bonding interactions within the planar triangles of the Pt_6P trigonal prisms (ICOHP $\sim$ 0.74; Table 4.4). Moreover, the shortest Pt-Pt distance between neighboring Pt_6P triangular prisms also shows significant bonding interactions (ICOHP $\sim$ 0.49). The structural nature of the bonding interaction between Pt-Pt atoms of neighboring triangles is shown in Figure 4.23. The close approach and bonds of the Pt atoms crowd into the 4e site and provide a rationale for the vacancy of the body-centered-cubic site. COHP analysis also shows that the Pt-Pt interactions between Pt_3 triangles of a Pt_6P trigonal prism [Pt-Pt distance = 3.388(1) Å] are essentially nonbonding (ICOHP $\sim$ 0.03). Thus, the "electron deficiency" of the Pt atoms (unfilled d orbitals) is compensated by the formation of Pt-Pt bonds within the triangular planes of the trigonal prisms and Pt-Pt atoms between neighboring trigonal prisms. The interprism Pt-Pt interactions coupled with the vacancy at the 4e site also provide an electronic and geometric rationale for the observed distortions of the Pt_6P trigonal prisms from ideality.

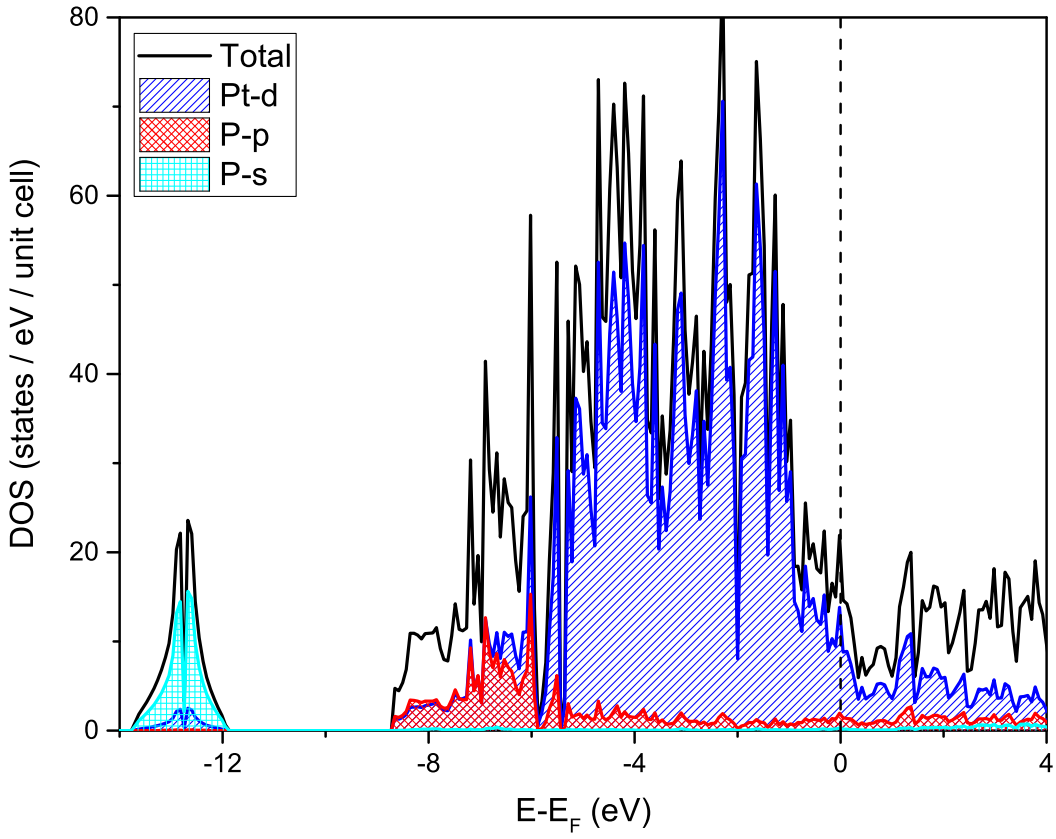

Figure 4.21: Calculated DOS and PDOS for $SrPt_6P_2$ using the LMTO method: (a) PDOS for Pt d states; (b) PDOS for P p states; (c) PDOS for P s states. Solid black line: total DOS. Shaded areas: PDOS. The Fermi level (E_F) is set at 0.0 eV.

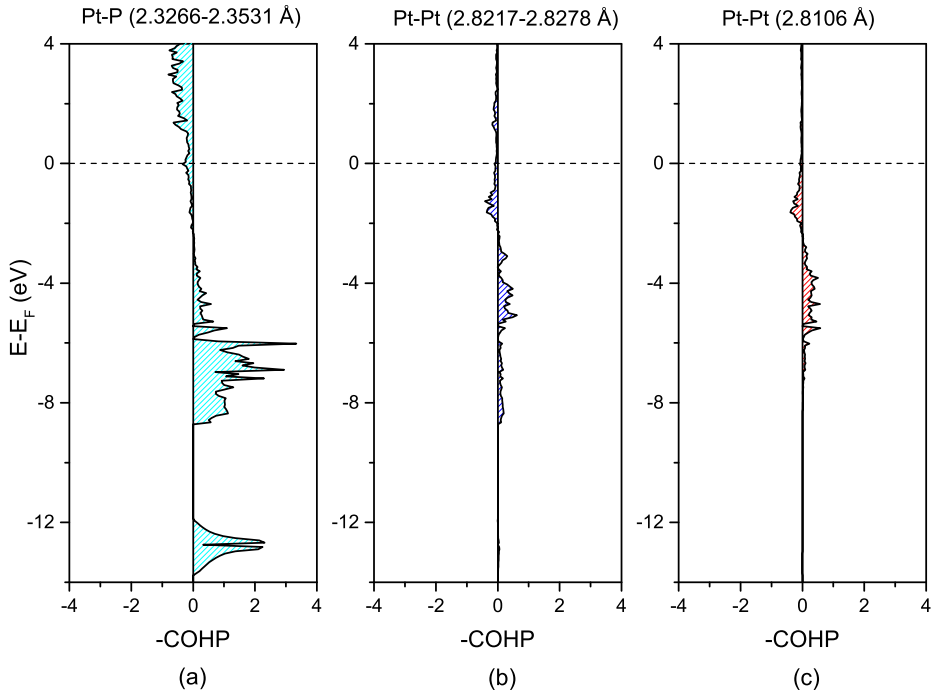

Figure 4.22: Calculated COHP curves for $SrPt_6P_2$: (a) COHP for P-Pt interactions (b) COHP for Pt-Pt interactions within Pt_3 trianglesk (c) COHP for Pt-Pt interactions between Pt_3 units of neighboring Pt_6P trigonal prisms. Fermi level (E_F) is set at 0.0 eV

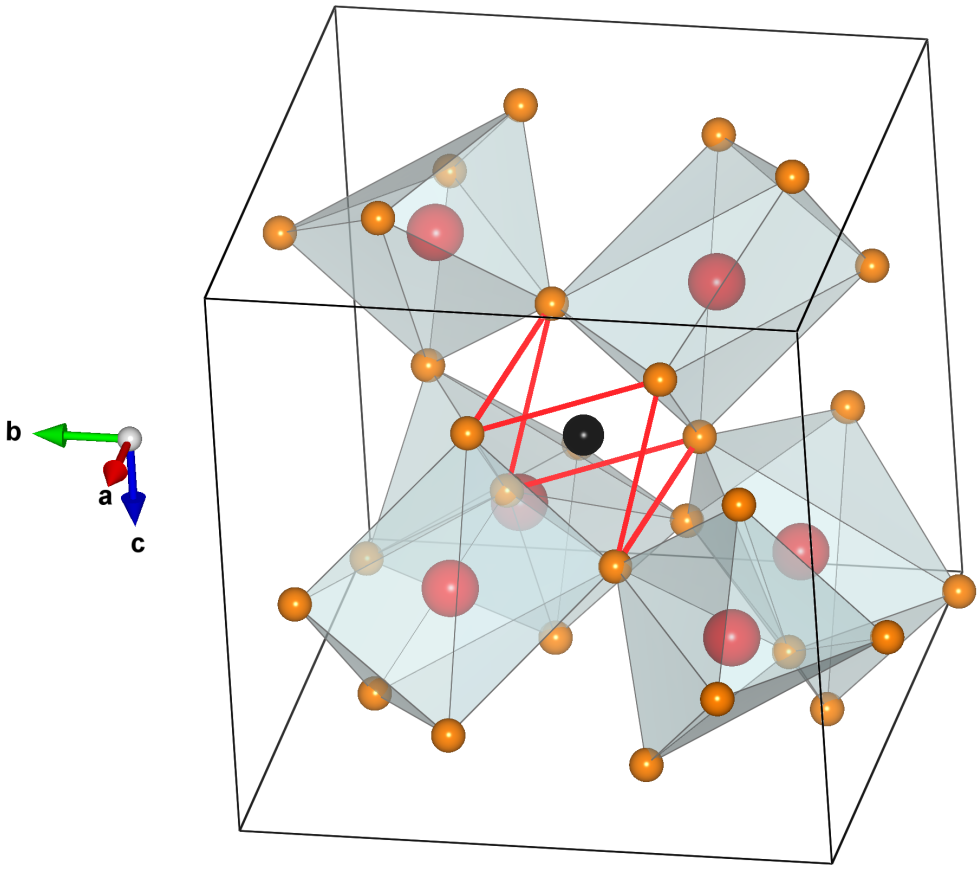

Figure 4.23: Pt-Pt bonding interactions between Pt atoms of neighboring Pt_6P trigonal prisms near vacant site indicated by red lines (some polyhedra removed for visibility).

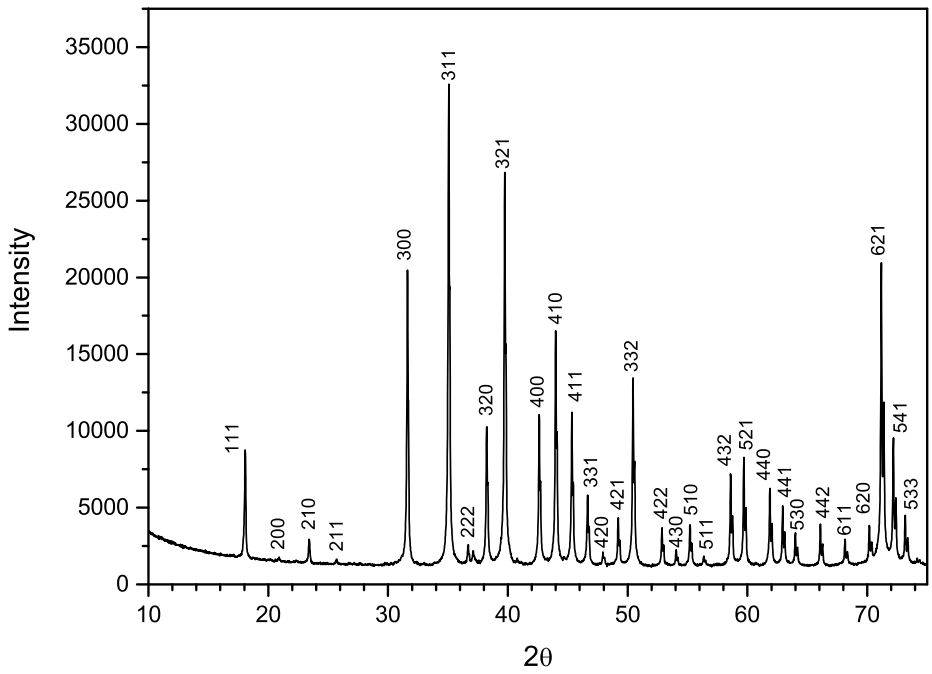

Figure 4.24: Powder XRD pattern with Miller indices for $SrPt_6P_2$

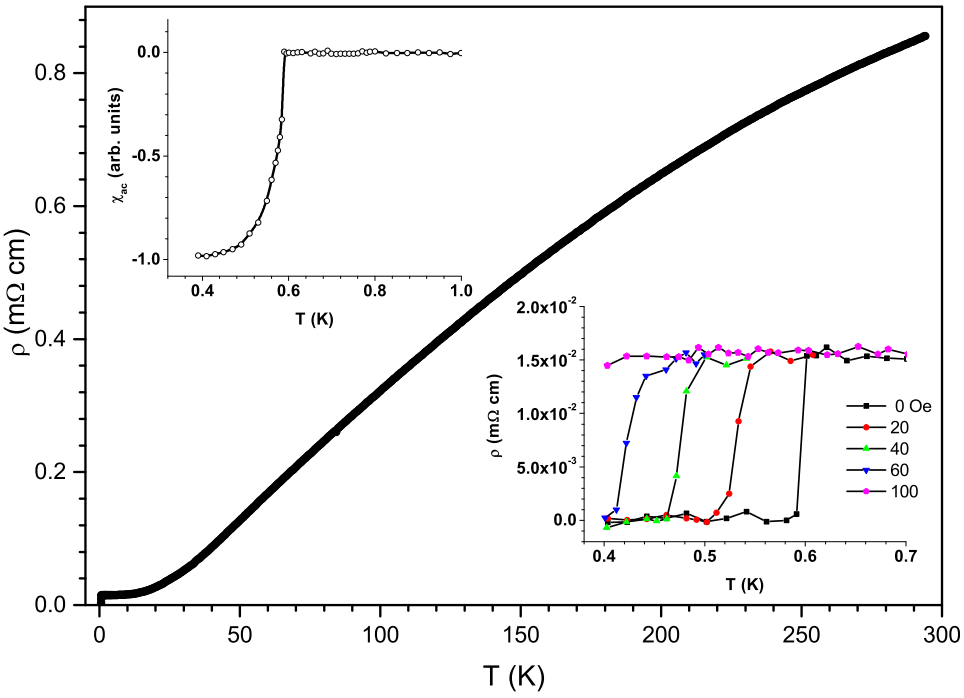

Figure 4.25: Resistivity $\rho(T)$ of $SrPt_6P_2$ from 0.4 to 290 K. Upper inset: ac susceptibility on a pelleted sample from mutual inductance measurements from 0.4 K to 1.0 K. Lower inset: resistivity data under different magnetic fields from 0.4 to 0.7 K

4.2.4 Electrical resistivity and magnetic susceptibility

The as-synthesized powder shows a dark-gray color with a metallic luster and is stable in air. The diffraction peaks from the powder XRD pattern were well indexed without any noticeable impurity peaks and match well with the theoretical pattern generated from the structure obtained from single-crystal X-ray diffraction, as shown in Figure 4.24. The temperature dependent resistivity, $\rho(T)$, of $SrPt_6P_2$ (Figure 4.25) at zero field, with a room temperature value of 0.85 $m\Omega \cdot cm$, decreases with temperature. The resistivity flattens between 8 and 0.6 K, and the residual resistivity is $\sim 0.015 m\Omega \cdot cm$. The relatively high value of the residual resistivity ratio, $\rho(290K)/\rho(5K) = 56$, suggests that the sample is of high quality. The resistivity drops sharply to zero below 0.60 K, with a transition width of less than 0.01 K at zero field, characteristic of a superconducting transition. In the presence of a magnetic field, the superconducting transition is systematically broadened, shifted to lower temperatures, and suppressed below 0.4 K at 100 Oe, as shown in the lower inset of Figure 4.25, suggesting a relatively low upper critical field. In addition, the superconducting transition of $SrPt_6P_2$ was confirmed by the ac susceptibility measured through a mutual inductance technique down to 0.4 K, using the Linear Research LR 400 bridge. It displays a large and narrow diamagnetic shift at $\sim$ 0.6 K with a tail nearly flat at 0.4 K, as shown in the upper inset of Figure 4.25, consistent with the $\rho(T)$ results and indicating the bulk superconducting nature of the material. To the best of our knowledge, this is the first Pt-based pnictide superconductor with trigonal-prismatic building units.

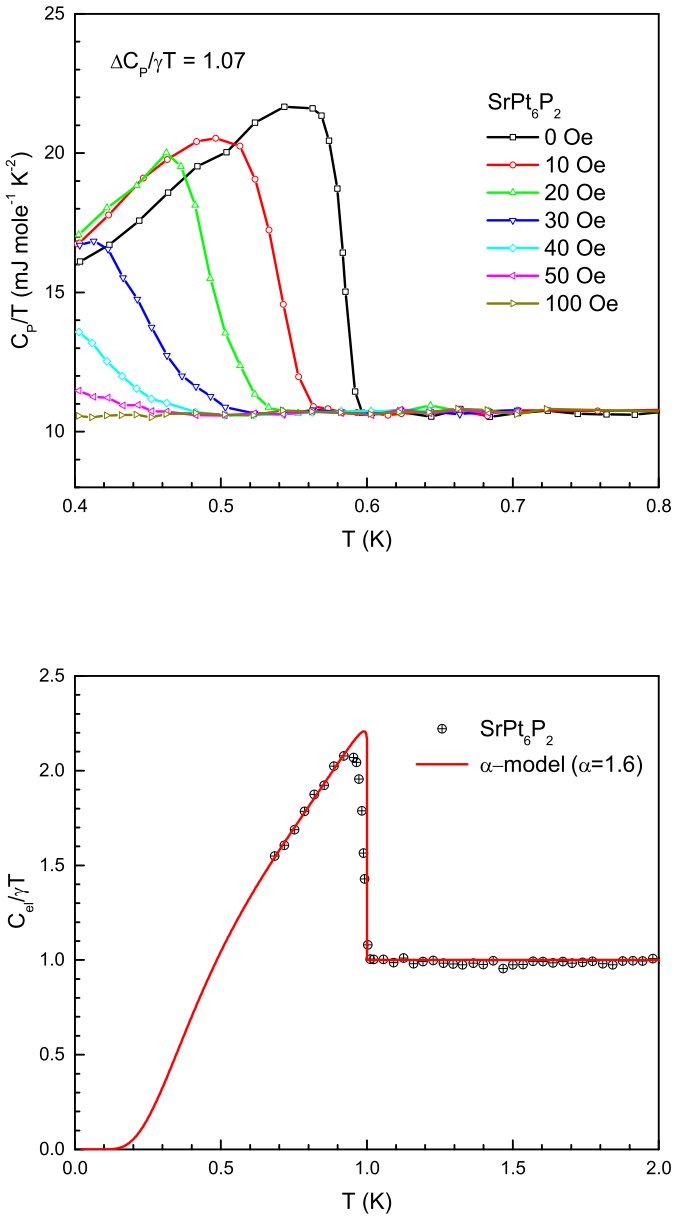

Figure 4.26: Top: specific heat $C_p/T(\text{mJ mol}^{-1}\text{K}^{-2})$ vs temperature of $SrPt_6P_2$ with different applied magnetic fields. Bottom: normalized specific heat $C_{el}/\gamma T$ vs. normalized temperature T/T_c for $SrPt_6P_2$ with α-model fitting shown (red curve) with $\alpha = 1.65$.

4.2.5 Heat capacity

To learn more about the nature of the superconductivity in $SrPt_6P_2$, we performed a detailed measurement of the specific heat. The measurement of the specific heat, besides allowing us to verify whether or not the superconductivity in $SrPt_6P_2$ is truly a bulk property, can tell us about the coupling strength of the superconductor (see Chapter 1). Specifically, we can determine the ratio $2\Delta_0/k_bT_c$, which is equal to 3.528 in the BCS theory. Figure 4.26 shows the results of the specific heat measurements carried out on a pure polycrystalline sample of $SrPt_6P_2$. Judging by the jump at T_c observed from the specific heat measurement, it is clear that the superconductivity in $SrPt_6P_2$ is bulk. Furthermore, as observed from the resistivity measurements, it is evident that the critical field is quite low - an applied field of 100 Oe completely suppresses the superconductivity down to the lowest measured temperature of 0.4 K. We fitted the temperature dependence of the specific heat below the transition temperature with the α-model, which gives a value of $\alpha = 1.6$ for $SrPt_6P_2$. The value of $\alpha = 1.6$ is quite low - the weak-coupling BCS value for $\alpha = 1.764$. Our observation of $\alpha < \alpha_{BCS}$ could explain the quite low transition temperature of 600 mK observed in $SrPt_6P_2$.

4.2.6 Analogy to $SrPt_3P$

It is interesting to note a structural analogy between $SrPt_6P_2$ and $SrPt_3P$ (Figure 4.27). If one considers doubling the unit cell of $SrPt_3P$, the resulting formula unit would be $Sr_2Pt_6P_2$. In this case, unlike in $SrPt_6P_2$, all of the cavity sites between

the network of corner-shared distorted octahedra are occupied. However, if one considers removing half of the Sr atoms from $SrPt_3P$ = $Sr_2Pt_6P_2$, the resulting stoichiometry is $SrPt_6P_2$. As discussed above, our DFT calculations and COHP analysis indicate that the $SrPt_6P_2$ structure is stabilized by bonding between Pt atoms of neighboring Pt_6P trigonal prisms near the vacant cavity. Essentially, one could consider that removing half of the Sr atoms from $SrPt_3P$ "opens" up half of the cavity sites. This "opening" of the cavity sites allows the other atoms to move into these sites slightly, and causes a rearrangment or "distortion" of the structural building blocks from octahedra into trigonal prisms. That this analogy can be made is supported by the bonding between neighboring trigonal prisms near the cavity sites, which stabilizes this distortion upon removal of half the Sr atoms.

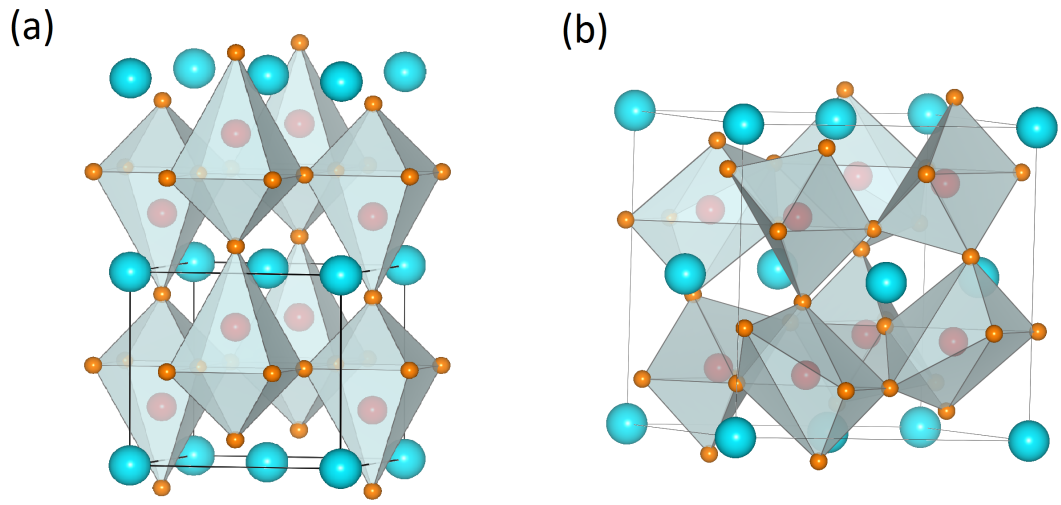

Figure 4.27: (a) Two unit cells of $SrPt_3P$, giving $Sr_2Pt_6P_2$, (b) unit cell of$SrPt_6P_2$

Given the fact that the elemental components of $SrPt_3P$ and $SrPt_6P_2$ are the same - Sr, Pt, and P, with electronically equivalent 6-coordinated P centered polyhedral

building blocks, and that there exists a striking analogy between these two compounds, what is the reason that strong-coupling superconductivity with relatively high T_c = 8.4 K exists in one, while weak-coupling superconductivity with quite low T_c = 0.6 K exists in the other? In order to answer this question, we must recall the mechanism for superconductivity in $SrPt_3P$. As discussed in the previous chapter, the superconductivity in $SrPt_3P$ is due to the strong coupling of low-energy in-plane "breathing" phonon modes of Pt to the Pt-P in-plane electronic states near the Fermi level. That the coupling strength is so high is likely due to the high anisotropy of these states, or the degree to which they are confined in the a-b plane. This suggestion is supported by previous calculations showing that the coupling strength of $CaPt_3P$ and $LaPt_3P$ are weaker than that of $SrPt_3P$, and that this can be attributed to the larger ionic radius of Sr which forces the vibrational mode of Pt to be more strongly localized in $SrPt_3P$ resulting in higher coupling strength and higher T_c[55]. We decided to calculate the density of states vs. energy for $SrPt_3P$ and $SrPt_6P_2$ to compare the degree of anisotropy of the Pt electronic states in these compounds (Figure 4.28). From this calculation, it is clear that in $SrPt_3P$ the $d_{(x^2-y^2)}$ in-plane states are contributing much more strongly to the DOS at E_F than the other orbitals of Pt. In contrast, the DOS of $SrPt_6P_2$ shows an almost equal contribution at E_F from the different d-orbitals of Pt. This shows that, while in $SrPt_3P$ the square-planar arrangement of Pt-atoms allows for an anisotropic DOS at E_F, the high degree of distortion in $SrPt_6P_2$ results in a basically isotropic DOS at E_F and possibly contributes to the observed weaker coupling and lower T_c

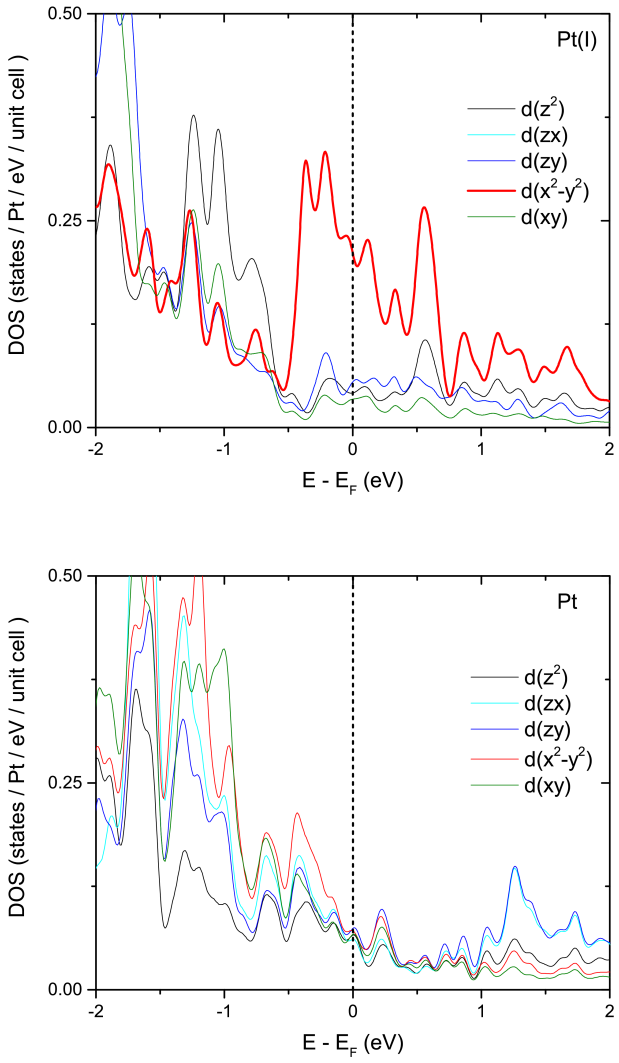

Figure 4.28: Density of states vs. energy ($E - E_F$) for (top) $SrPt_3P$ and (bottom) $SrPt_6P_2$

4.2.7 Summary

To summarize, in this section our discovery of a new structure type superconductor, $SrPt_6P_2$, was presented and discussed. A detailed describtion of the crystal structure of $SrPt_6P_2$ was given, followed by calculations of the bonding interactions which provided insight into the stability of this compound. The superconductivity was investigated magnetically and resistively and exhibits a T_c of 600 mK. The results of our specific heat study were discussed, which show that superconductivity in $SrPt_6P_2$ is of weak-coupling nature, explaining the rather low value of T_c. Finally, an analogy to $SrPt_3P$ was given, supported by DFT calculations showing a rather isotropic density of states at the Fermi level in $SrPt_6P_2$ as a possible driving factor in the strongly reduced coupling strength and hence T_c compared to $SrPt_3P$.

4.3 $SrPt_{10}P_4$

4.3.1 Introduction

In the previous two chapters, investigations into two ternary platinum phosphide superconductors were presented. First, $SrPt_3P$, a strong-coupling electron-phonon type superconductor was introduced and a systematic study of chemical doping and the application of high physical pressure were presented and discussed. In the following chapter, our discovery of the new-structure-type superconductor $SrPt_6P_2$ with weak-coupling nature was presented and discussed, as well as a comparison between $SrPt_3P$ and $SrPt_6P_2$. The large difference in T_c was explained as being due to the large difference in the coupling strength: in $SrPt_3P$, $2\Delta/k_BT_c \sim 5.0$, whereas in $SrPt_6P_2$, $2\Delta/k_BT_c \sim 3.2$. Furthermore, both of these two Sr-Pt-P superconductors contain 6-coordinated P-centered Pt_6P polyhedra as building blocks: octahedral building blocks in $SrPt_3P$, and trigonal prismatic building blocks in $SrPt_6P_2$. Because of this large difference in superconducting properties between these two related compounds with identical elemental components Sr, Pt, and P, and similar building blocks, we became interested in searching for other new superconducting compounds with Sr, Pt, and P, with unique crystal structures. In this section, our discovery of another, new-structure type superconductor $SrPt_{10}P_4$ with two superconducting gaps in this family of materials is presented and discussed.

Outline The rest of this section will be organized as follows. First, the crystal structure of $SrPt_{10}P_4$ will be discussed. The results of electrical transport and

magnetic susceptibility measurements showing superconductivity in this compound will follow. The results of the high-pressure work will be detailed. Then, the specific heat data of $SrPt_{10}P_4$ will be presented and discussed, followed by a discussion of the critical field data, and our discovery of two-gap superconductivity in $SrPt_{10}P_4$. Finally a summary of the work on $SrPt_{10}P_4$ will be given.

4.3.2 Crystal structure

The crystal structure of $SrPt_{10}P_4$ is both unique and complex, with 218 atoms per unit cell. $SrPt_{10}P_4$ crystallizes in a monoclinic structure type with space-group C2/c (#15) (structural parameters shown in Table 4.5). The angle β which makes this compound monoclinic is only slightly off from 90°, at 90.027°. A perspective view of a single unit cell of $SrPt_{10}P_4$ can be seen in Figure 4.29. Like $SrPt_3P$ and $SrPt_6P_2$, the basic building blocks of this compound are 6-coordinated P-centered Pt_6P polyhedra. However, unlike $SrPt_3P$ and $SrPt_6P_2$, the building blocks of $SrPt_{10}P_4$ come in two different varieties: octahedral and trigonal-prismatic. The two different types of polyhedra form two distinct types of layers which alternate with each other. This can be seen by viewing the crystal structure along the b and a axes as is shown in Figures 4.30b and 4.30c. One type of layer contains the strontium atoms, and the other type of layer does not. Let us first consider the type of layer that does not contain the strontium atoms. The layer that does not contain Sr atoms is composed of a network of highly distorted Pt_6P octahedral building blocks which form edge-shared pairs. These pairs of edge-shared octahedra are then corner shared with each other to form a 2d network with narrow cavity sites too small for the Sr atoms to occupy

(Figure 4.31a). The other type of layer, which contains the Sr atoms, is composed of a network of distorted trigonal prismatic Pt_6P building blocks. In this layer, the trigonal prisms are all edge-shared with each other to form a honeycomb-like 2d network. Looking at the c-axis view shown in Figure 4.31b, one can see that these edge-shared trigonal prisms form hexagon-shaped vacancies which are occupied by the Sr atoms.

4.3.3 Electrical resistivity and magnetic susceptibility

Figure 4.32 shows the results of our electrical transport measurements on $SrPt_{10}P_4$ from 300 K down to 500 mK. The temperature dependence of the resistivity of $SrPt_{10}P_4$ indicates a metallic behavior, while the strong negative curvature in the temperature dependence indicates possible strong electron correlations in this material. A suppression of superconductivity down to 500 mK is observed upon the application of a magnetic field of 1 T. The magnetic susceptibility of $SrPt_{10}P_4$ was also measured down to 500 mK (Figure 4.33) using a three-coil compensated mutual inductance technique as described in the Experimental Methods chapter. The narrow width of the superconducting transition ($\approx$ 0.1 K at 90% drop) indicates the very high quality of the sample.

Table 4.5: Structural parameters for $SrPt_{10}P_4$

Atom	Site	x	y	z
Pt(1)	8f	0.0782	0.2746	0.0164
Pt(2)	8f	0.3247	-0.0210	0.5158
Pt(3)	8f	0.2477	-0.0144	0.3512
Pt(4)	8f	0.1212	0.1487	0.3431
Pt(5)	8f	0.1513	0.0028	0.4813
Pt(6)	8f	0.1178	0.1182	0.1438
Pt(7)	8f	0.1267	0.1085	0.6543
Pt(8)	8f	0.0016	0.2656	-0.1478
Pt(9)	8f	0.0956	0.2515	0.5156
Pt(10)	8f	0.1183	0.3654	-0.1558
Pt(11)	8f	0.2321	-0.0210	0.6514
Pt(12)	8f	0.3538	0.1168	0.3520
Pt(13)	8f	0.1925	0.2650	-0.0049
Pt(14)	8f	0.1344	0.3937	0.1549
Pt(15)	8f	0.3675	0.1309	0.6453
Pt(16)	8f	0.0356	0.0800	0.4892
Pt(17)	8f	0.0585	0.4887	-0.0014
Pt(18)	8f	0.1037	0.1359	-0.1493
Pt(19)	8f	0.2134	0.1710	0.5131
Pt(20)	8f	-0.0129	0.2723	0.1508
Sr(1)	4e	0.0000	0.0089	0.2500
Sr(2)	8f	0.2495	0.2549	0.2468
Sr(3)	4e	0.0000	0.4958	-0.2500
P(1)	8f	0.3122	0.1592	0.5023
P(2)	8f	0.2337	-0.1085	0.5007
P(3)	8f	0.0620	0.0934	0.0016
P(4)	8f	0.0829	0.2629	0.2209
P(5)	8f	-0.0874	0.2561	-0.2202
P(6)	8f	0.1569	0.0014	0.2791
P(7)	8f	0.3242	-0.0064	0.7227
P(8)	8f	0.0130	0.6405	0.0009

Axis	Length
a	22.9151(9) Å
b	13.1664(5) Å
c	13.4131(5) Å

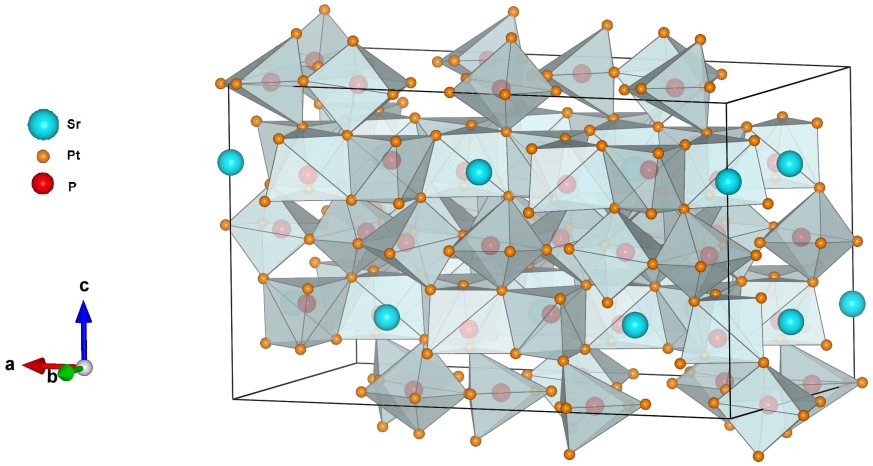

Figure 4.29: Perspective view of the crystal structure of $SrPt_{10}P_4$

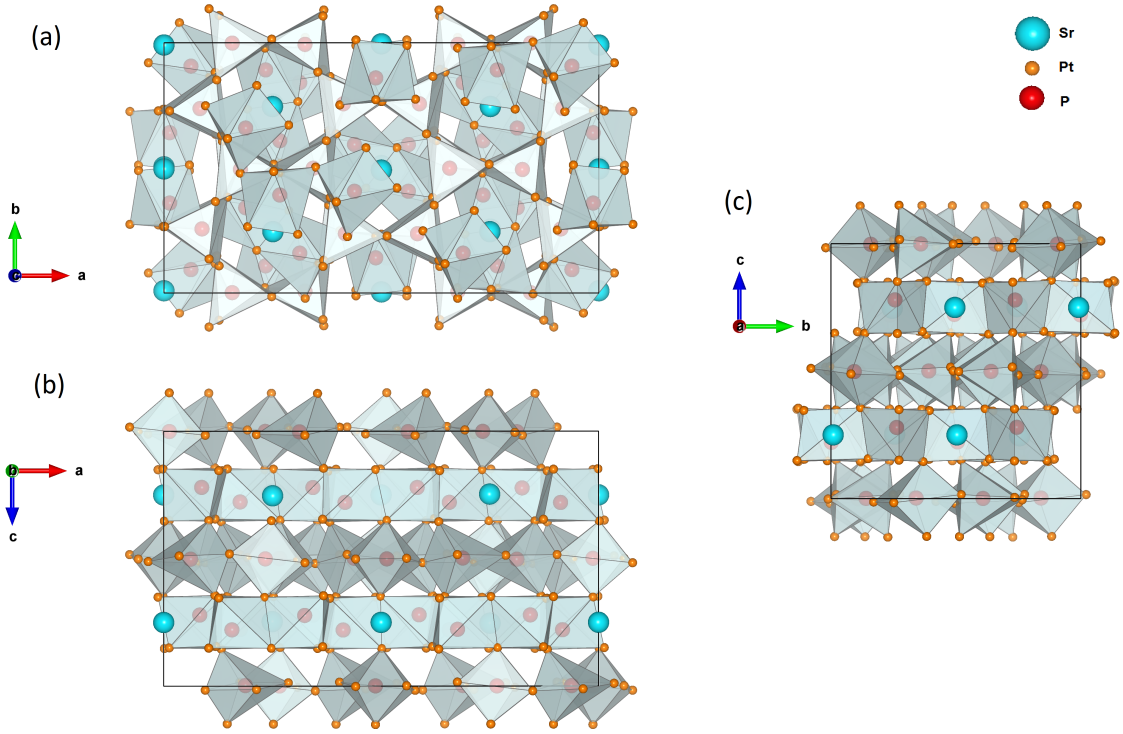

Figure 4.30: Crystal structure of $SrPt_{10}P_4$ viewed along different crystallographic axes

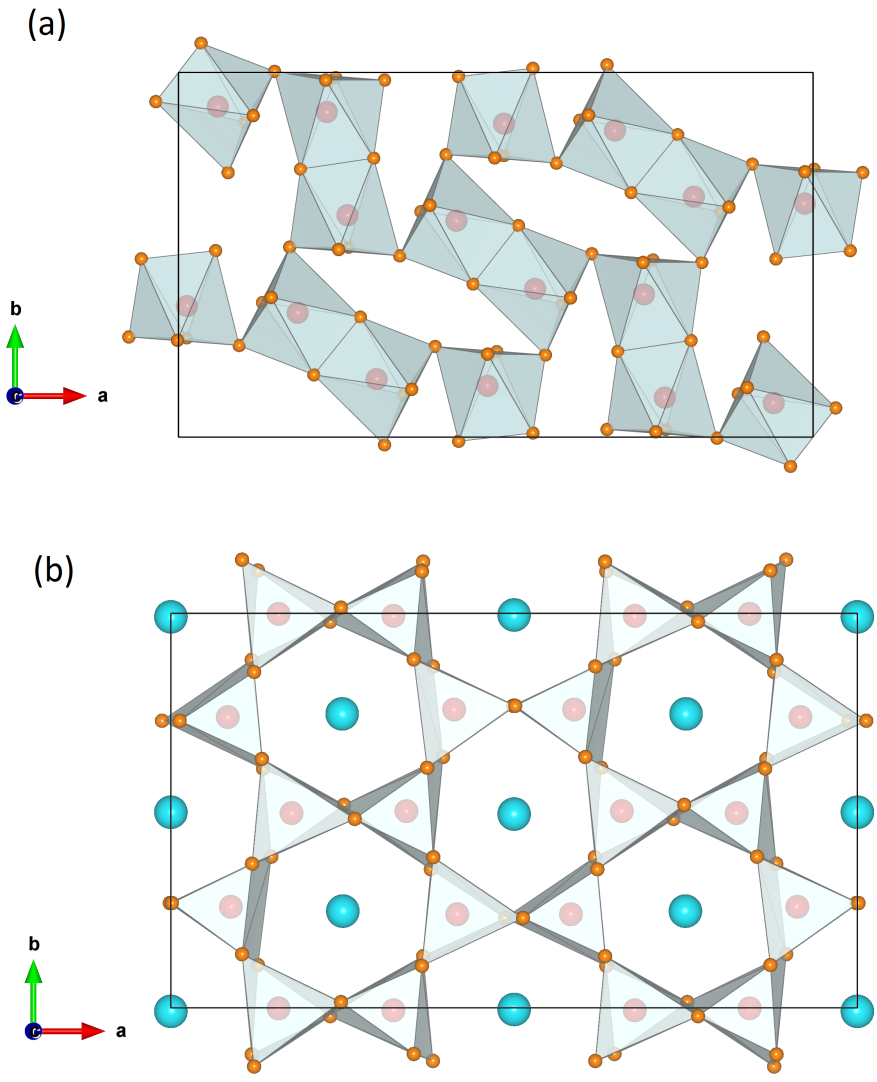

Figure 4.31: Two different layers of $SrPt_{10}P_4$ viewed along the c-axis

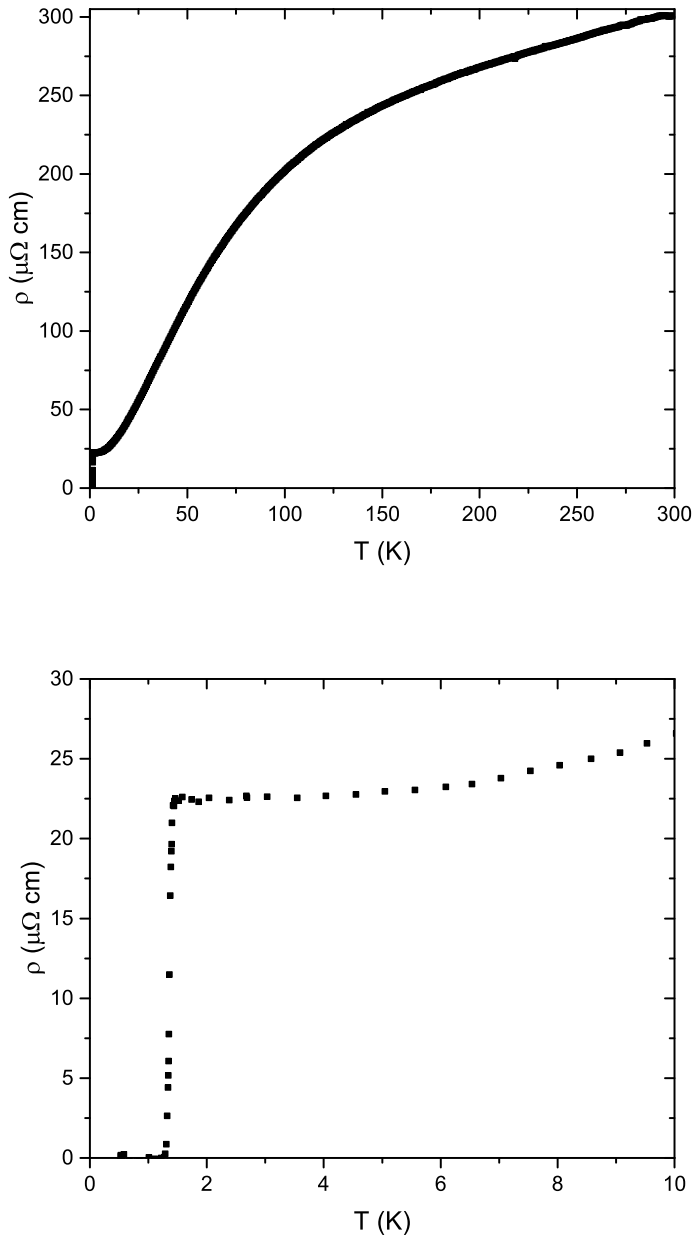

Figure 4.32: (Top) Resistivity vs. temperature from 0.5 K to 300 K for $SrPt_{10}P_4$, (bottom) enlarged scale view below 10 K of the superconducting transition

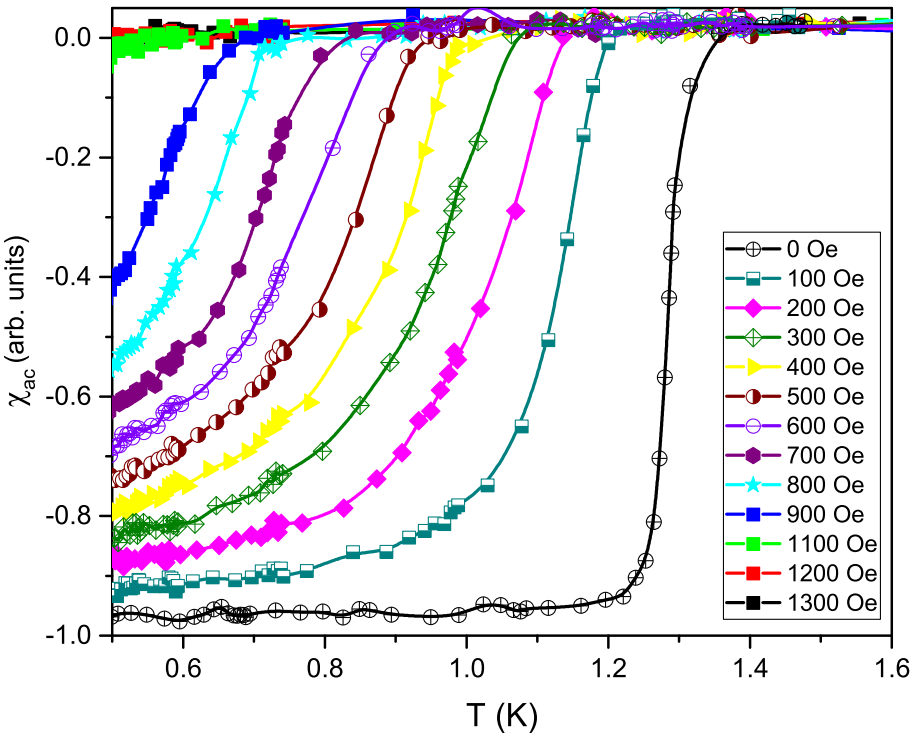

Figure 4.33: χ_{ac} vs. temperature for $SrPt_{10}P_4$ at different applied magnetic fields near the superconducting transition

4.3.4 High pressure

To probe the effects of lattice compression in $SrPt_{10}P_4$, we applied high physical pressure using a BeCu piston-cylinder type pressure cell as described in the Experimental Methods chapter. Upon the application of pressure up to 15.29 kbar, we observe a systematic suppression of the transition temperature T_c from ~ 1.263 K to ~ 1.234 K, or ~ 2.3% (Figure 4.34). A linear fit of the plot of T_c vs. pressure yields the pressure coefficient dT_c/dp = -0.019 K / GPa (Figure 4.35), and $dln T_c/dp$ = -0.015 K / GPa. The systematic suppression of T_c suggests that there is no significant peak in the density of states near the Fermi level. The relatively small change in T_c with pressure is comparable to that of many elemental superconductors which exhibit a linear suppression of T_c with pressure near ambient pressure[50] and is very close to the value of dT_c/dp = -0.02 K / GPa for pure niobium metal[68]. The suppression of T_c with pressure in $SrPt_{10}P_4$ can therefore be explained as the result of a stiffening of the lattice induced by the pressure, which results in a weakening of the electron-phonon coupling and therefore the T_c.

4.3.5 Specific heat

In order to verify the bulk nature of the superconductivity in $SrPt_{10}P_4$ and to extract information such as the electronic specific heat coefficient γ, we decided to measure the specific heat of a pure, bulk, polycrystalline sample of $SrPt_{10}P_4$. Figure 4.36 (top) shows the results of this measurement under different applied magnetic fields up to 600 Oe. The jump at T_c observed in the specific heat clearly demonstrates

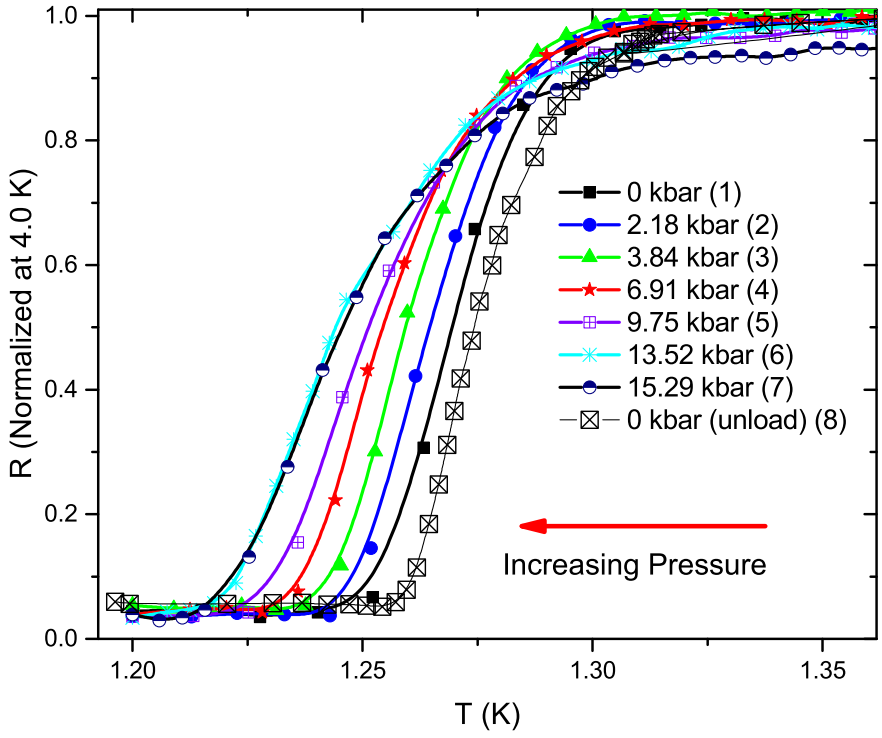

Figure 4.34: Resistivity vs. temperature of $SrPt_{10}P_4$ under different applied pressures

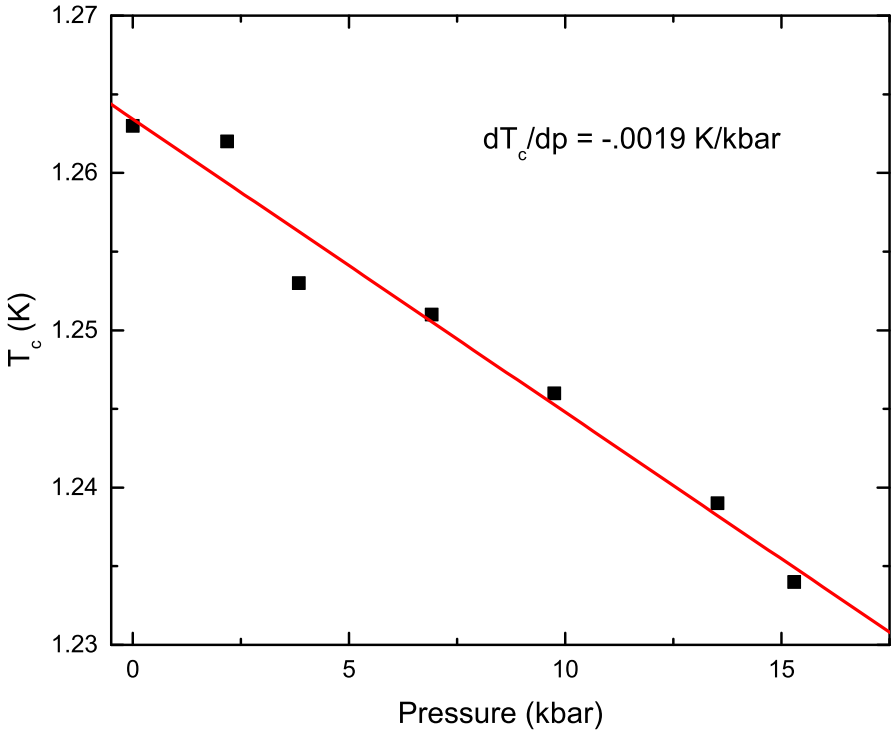

Figure 4.35: T_c vs. pressure for $SrPt_{10}P_4$

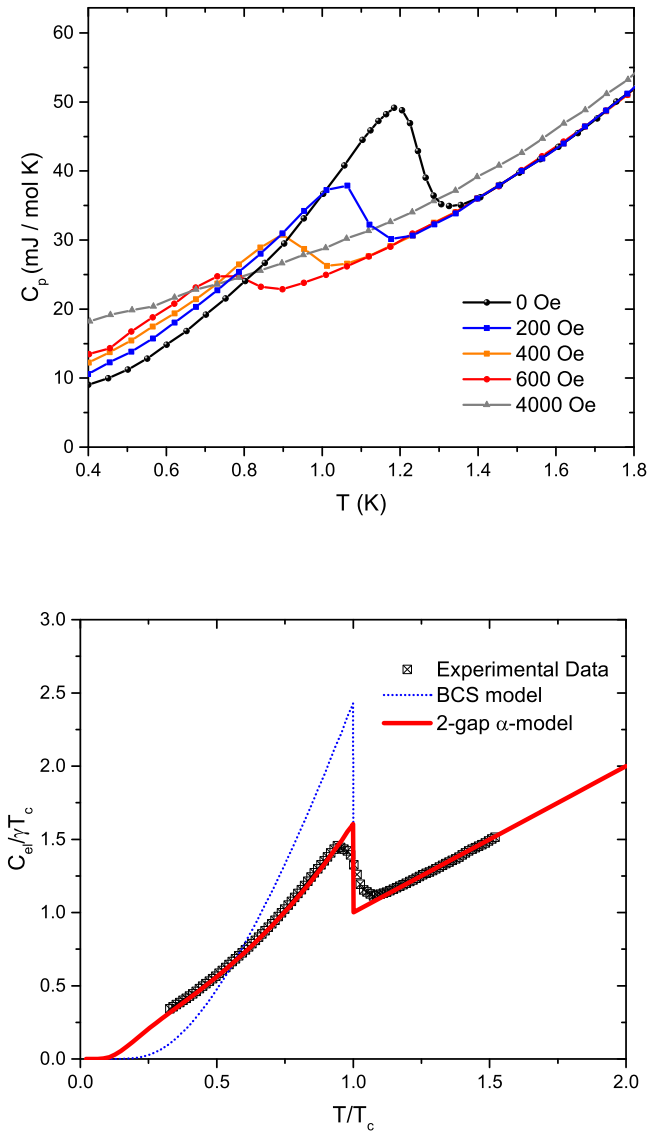

Figure 4.36: (Top) specific heat vs. temperature for $SrPt_{10}P_4$ at different applied magnetic fields, (bottom) $C_{el}/\gamma T_c$ vs temperature with BCS (dashed blue line) and 2-gap alpha-model (solid red line) fitting, where $2\Delta_1/k_BT_c = 2.0$ and $2\Delta_2/k_BT_c = 4.2$ for the 2-gap fit, and $\gamma = 32.5$ mJ/mol $\cdot$ K^2.

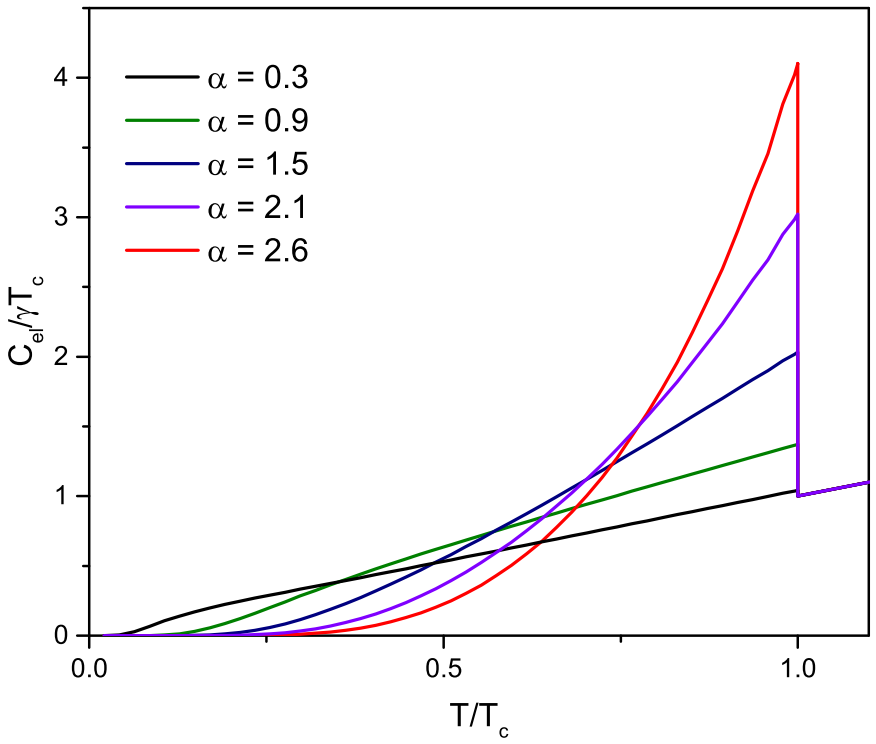

Figure 4.37: Theoretical $C_{el}/\gamma T_c$ vs. T/T_c for different values of α.

that the superconductivity observed in $SrPt_{10}P_4$ is of bulk nature. Using the relation $C/T = \gamma + \beta T^2$, we extract $\beta = 2.74$ mJ/mol $\cdot$ K^4. From this, we use the relation $\Theta_D = (12\pi^4 NR/5\beta)$ to obtain the Debye temperature $\Theta_D = 220$ K. This Debye temperature is comparable to that of $SrPt_3P$ ($\sim$ 200 K). As in the case of $SrPt_3P$ and $SrPt_6P_2$, we fit the temperature dependence of the specific heat below the transition temperature T_c with the α-model to learn more about the coupling strength of $SrPt_{10}P_4$. The fitted specific heat data for $SrPt_{10}P_4$ is shown in Figure 4.36 (bottom). It is clear from this plot that the data cannot be fitted with a single-gap model.

Specifically, at lower temperatures, the specific heat is higher than that predicted by a single-gap model. This can be accounted for by considering a two-gap α-model. The two-gap α-model is an extension of the one-gap α-model, allowing for two variable parameters $\alpha_1 = \Delta_1/k_BT_c$ and $\alpha_2 = \Delta_2/k_BT_c$. This model was used as early proof of the existence of two superconducting gaps in MgB_2 [41]. Figure 4.37 shows the theoretical $C_{el}/\gamma T_c$ vs. T/T_c for different values of α. This illustrates why the two-gap model can fit the specific heat data of $SrPt_{10}P_4$ while the single-gap model cannot. The low-temperature specific heat, which goes to zero more slowly than the BCS theory model, can be accounted for by including a second, smaller superconducting gap which has a low value of $\alpha = \Delta/k_BT_c$. Specifically, from the specific heat fitting, the values for the two superconducting gaps in $SrPt_{10}P_4$ are $2\Delta_1/k_BT_c = 2.0$ and $2\Delta_2/k_BT_c = 4.2$.

4.3.6 Critical field

To learn more about the superconductivity in $SrPt_{10}P_4$, we decided to study the behavior of the upper critical field H_{c2}. The temperature dependence of the upper critical field H_{c2} can provide a substantial amount of information regarding the nature of the superconductivity in a given material. Specifically, for a multi-band superconductor, the temperature dependence of the upper critical field H_{c2} is expected to differ from that of a single-band superconductor. The specific heat results show $SrPt_{10}P_4$ to be a two-gap superconductor; therefore, we should expect that the temperature dependence of H_{c2} can be described by a multi-band model rather than a single-band model. Figure 4.39 shows the resistive superconducting

transition of $SrPt_{10}P_4$ at different applied magnetic fields. The T_c is determined for each applied magnetic field by drawing a horizontal line at 10% of the resistive drop. The resulting dependence of the normalized critical field $H_{c2}/H_{c2}(0)$ on the normalized temperature T/T_c is shown in Figure 4.40. The expected temperature dependence of the single-gap BCS is linear near T_c and has a negative curvature at higher magnetic field values until levelling off near zero temperature. The temperature dependence of a two-band superconductor can be quite different and can exhibit significant positive curvatures at temperatures below T_c. For example, MgB_2 exhibits a very high upper critical field with an upward curvature in the temperature dependence[42]. Gurevich and coworkers attributed this upward curvature and high upper critical field to multi-band effects and employed a two-gap model to fit the data[42]:

$$2w[\ln t + u(b/t)][\ln t + u(\eta b/t)] + \lambda_b[\ln t + u(\eta b/t)] + \lambda_a[\ln t + u(b/t)] = 0$$

where $t = T/T_c$, $u(x) = \psi(1/2 + x) - \psi(1/2)$ ($\psi(x)$ is the Euler digamma function), $b = \hbar H_{c2} D_\sigma / 2\phi_0 k_B T_c$, ϕ_0 is the magnetic flux quantum, $\eta = D_2/D_1$, $w = \lambda_{11}\lambda_{22} - \lambda_{12}\lambda_{21}$, $\lambda_{a,b} = \lambda_0 \pm \lambda_-$, $\lambda_0 = (\lambda_-^2 + 4\lambda_{12}\lambda_{21})^{1/2}$, $\lambda_- = \lambda_{11} - \lambda_{22}$ and λ_{mn} are the BCS superconducting coupling constants. The D_m are the diffusivities of the different bands. For MgB_2, $\lambda_{11} = 0.81$, $\lambda_{22} = 0.28$, $\lambda_{12} = 0.115$, $\lambda_{21} = 0.09$, and $\eta = 0.12$ (solid green line in Figure 4.40). For $SrPt_{10}P_4$, we obtained the following values using this model (solid blue line in Figure 4.40): $\lambda_{11} = 1.3$, $\lambda_{22} = 1.1$, $\lambda_{12} = 0.2$, $\lambda_{21} = 0.2$, and $\eta = 0.035$.

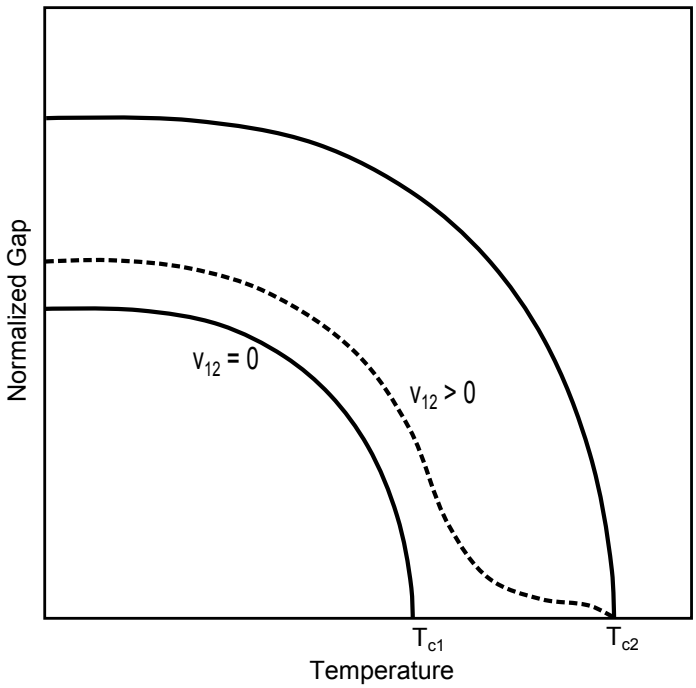

Figure 4.38: Temperature dependence of superconducting gap Δ in the case of two gaps. Solid lines indicate two gaps in the case of zero interband coupling, dashed line indicates smaller gap in the case of interband coupling (Figure adapted from [69]).

If the diffusivity in the two different bands is the same (if $D_1 = D_2$), then the temperature dependence reproduces that of the single-gap model. However, if the diffusivities are very different between the two bands, the curvature deviates significantly from that of the single-gap model and can present an upward curvature. Furthermore, the temperature at which this strong upward curvature occurs depends on the strength of the interband coupling constants (Figure 4.38). For MgB_2, the interband coupling is relatively weak, which could be attributed to the orthogonality of the σ and π bands, and the upward curvature in the temperature dependence of the critical field H_{c2} can be observed at low temperature (Figure

4.40). However, in $SrPt_{10}P_4$, the upward curvature occurs at a temperature closer to T_c, and the fitting yields interband coupling constants $\lambda_{12} = \lambda_{21} = 0.2$. The higher value of the interband coupling constants compared to MgB_2 gives insight into the possible origins of the two superconducting gaps in $SrPt_{10}P_4$. The two different types of layers in $SrPt_{10}P_4$ may hold two different types of charge carriers which would form two different Fermi surfaces. The relatively high interband coupling suggests that these two Fermi surfaces may be parallel to each other or at least not orthogonal as in the case of MgB_2. Figure 4.42 shows the results of charge density calculations on $SrPt_{10}P_4$. The charge density is shown along the two different types of layers (top = octahedral layer, middle = trigonal prismatic layer) as well as along the b-c plane (bottom). The very strong Pt-P bonding along the b-c plane, as indicated by the dark violet color in the figure, suggests that the phonons produced by these bonds are likely too energetic to participate in cooper pairing. If this is the case, then other candidates would be Pt-P bonds in along the a-b plane in the octahedral or trigonal prismatic layers. Then, it is possible that the two different types of electrons coming from the two different layers would couple differently to these phonons, resulting in two different superconducting gaps. Our magnetoresistance measurements (Figure 4.41) show a strongly non-quadratic magnetic field dependence of the magnetoresistance in $SrPt_{10}P_4$. In a metal with one type of charge carrier, the magnetoresistance would be expected to follow a quadratic magnetic field dependence:

$$\sigma_{xx} = \frac{\sigma_0}{1 + \omega_c^2 \tau^2}$$

where $\omega_c = eB/m^* =$ cyclotron frequency. Therefore, $\rho \propto B^2$. However, in a case with multiple carriers with distinct mobilities, a non-quadratic behavior could be expected [36], as we have observed for $SrPt_{10}P_4$.

4.3.7 Summary

We have discovered a new structure-type Sr - Pt - P superconductor with a unique combination of structural building blocks from both $SrPt_3P$ and $SrPt_6P_2$. We fully characterized the crystal structure and found the basic building blocks to be Pt_6P polyhedra, with two distinct types of layers. One type of layer is composed of a network of distorted corner-shared pairs of octahedra, while the other type of layer is composed of a network of edge-shared trigonal prisms with Sr atoms filling vacancies. We carried out magnetic susceptibility and electrical transport measurements which showed superconductivity at 1.4 K. We applied high physical pressure and found that the transition temperature is systematically suppressed, consistent with electron-phonon type superconductivity in which the stiffening of the lattice results in a weakening of electron-phonon coupling. We discovered the existence of two superconducting gaps by detailed analysis of specific heat and critical magnetic field data, and suggest a possible relation to the existence of two different types of charge carriers participating in cooper pairing, as supported by the non-quadratic magnetic field dependence of the magnetoresistance.

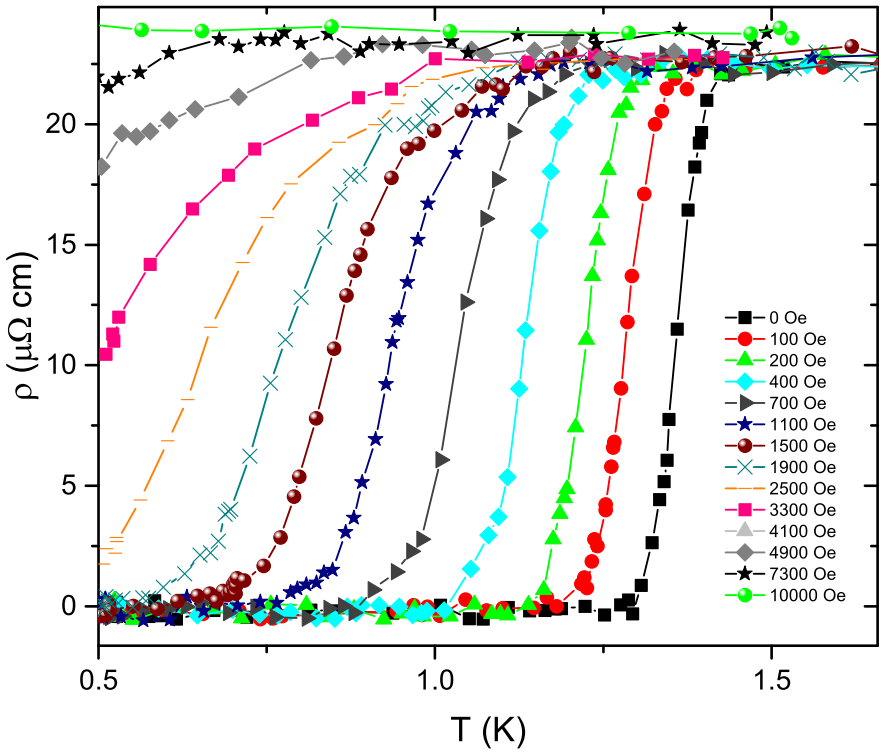

Figure 4.39: Enlarged scale view of the superconducting transition of $SrPt_{10}P_4$ at different applied magnetic fields

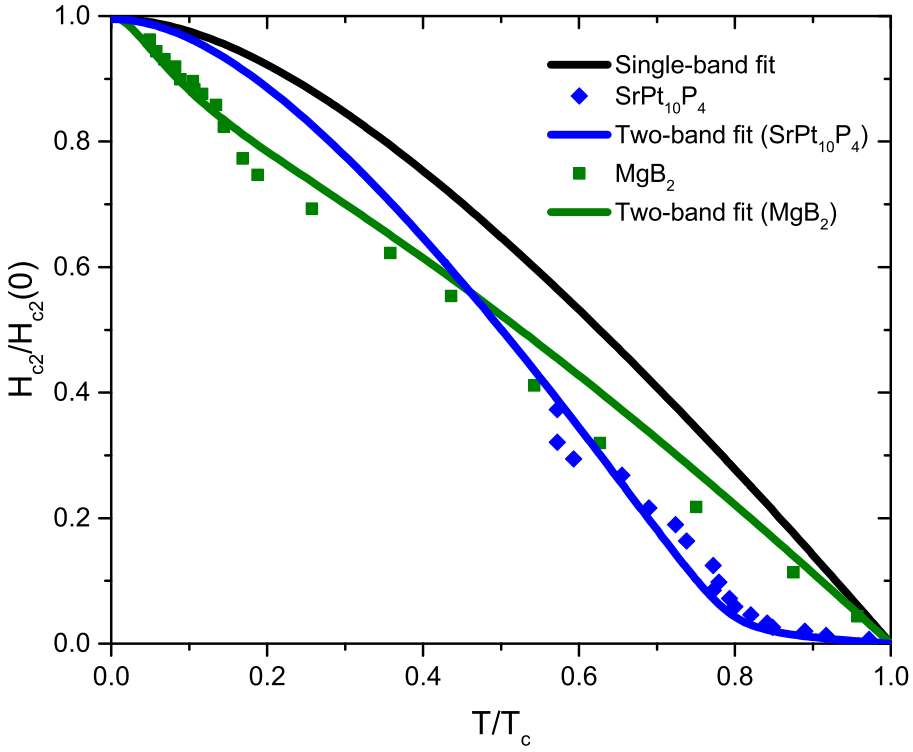

Figure 4.40: Normalized critical magnetic field $H_{c2}/H_{c2}(0)$ vs. normalized temperature T/T_c. Solid black line indicates single-gap BCS model, solid blue line indicates two-gap fit to $SrPt_{10}P_4$. Shown for comparison is data for MgB_2 [42]. Solid green line indicates two-gap fit to MgB_2 data.

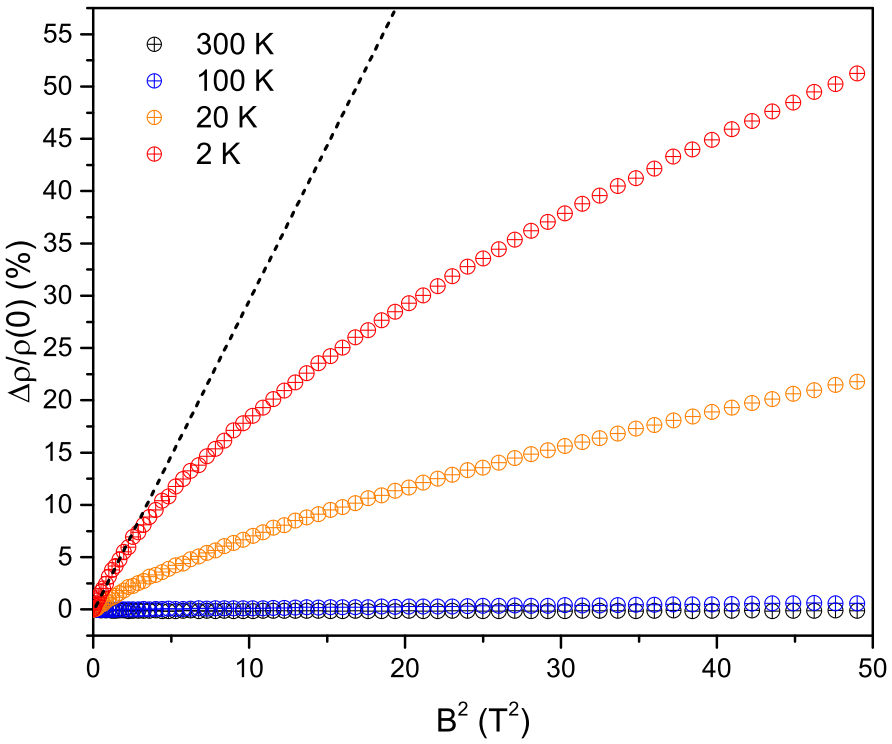

Figure 4.41: Magnetoresistance of $SrPt_{10}P_4$ vs. B^2 at different temperatures. Dashed line shows linear extrapolation from 2K data at low field strength.

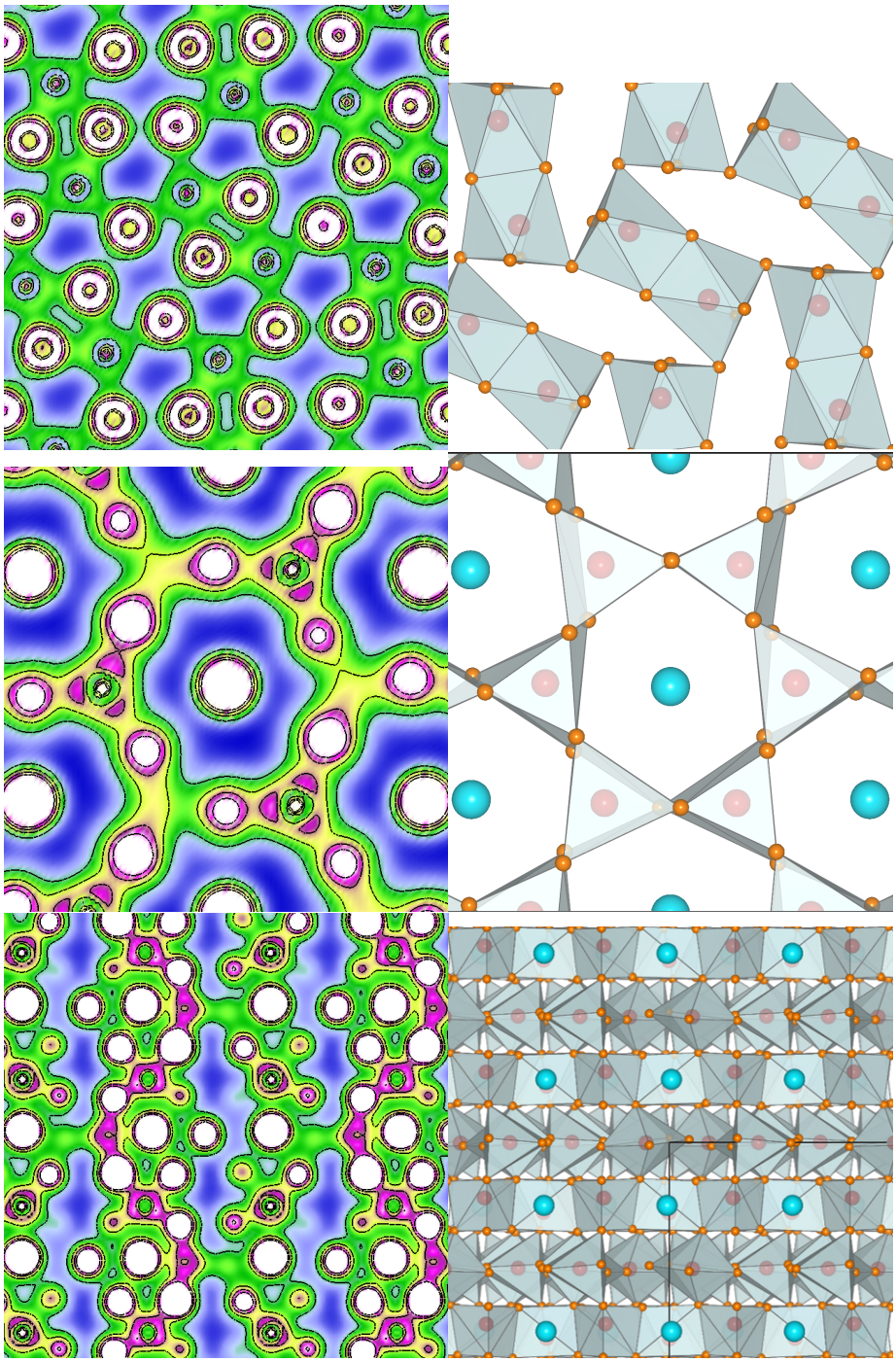

Figure 4.42: Charge density distribution in $SrPt_{10}P_4$ on the (top) a-b plane (octahedral layer), (middle) a-b plane (trigonal prismatic layer), and (bottom) b-c plane

Chapter 5

Conclusions

In this dissertation, an investigation of the superconducting properties of a series of strontium platinum phosphides has been carried out. Techniques such as electrical resistivity, calorimetry, magnetometry, and the application of high physical pressure were employed to gain insight into the nature of the superconductivity in $SrPt_3P$, $SrPt_6P_2$, and $SrPt_{10}P_4$, which have transition temperatures of 8.4 K, 0.6 K, and 1.4 K, respectively.

We found that, in $SrPt_3P$, the non-scaling of the T_c with the density of states at the Fermi level $N(E_F)$ can be attributed to a significant weakening of the electron-phonon coupling strength, likely due to a change in the local rigidity induced by a shortening of the Pt-P bond length. Our results show that, contrary to previous theoretical predictions, an increase in the density of states induced by hole doping leads to a decrease in the T_c as well as a decrease in the value of $\alpha = \Delta_0/k_BT_c$. We discovered two new superconductors, $SrPt_6P_2$ and $SrPt_{10}P_4$, which have very

different values of T_c despite striking similarities. $SrPt_6P_2$ was found to be a weak-coupling superconductor with $T_c = 0.6$ K based on α-model fitting of the specific heat data. As in $SrPt_3P$, the structural building blocks of $SrPt_6P_2$ are corner-shared Pt_6P polyhedra. Our DFT calculations revealed that significant inter-polyhedral Pt-Pt bonding stabilizes this structure despite the half of the cavity sites being unoccupied by Sr. Our DFT calculations also provide a possible rationale for the significantly weakened electron-phonon coupling and lower T_c compared to $SrPt_3P$ by comparing the anisotropy of the density of states at the Fermi level $N(E_F)$. In $SrPt_{10}P_4$, multi-gap superconductivity with strong inter-gap coupling was discovered by examination of the temperature dependence of the specific heat as well as the temperature dependence of the upper critical field H_{c2}. In $SrPt_{10}P_4$, two different types of Pt_6P polyhedra form two different types of layers. Our charge density calculations, coupled with the non-quadratic magnetic field dependence of the magnetoresistance, suggest that charge carriers from Pt-P bonds found in two different types of layers may couple differently to the lattice and lead to the observed two superconducting gaps.

This series of superconductors with Sr - Pt - P composition but with very different critical temperatures due to strongly varying coupling strengths provides a model system in which the same fundamental building block of Pt_6P polyhedra can lead to a wide range of superconducting properties, from weak to strong coupling, from single to multiple gaps, and from $T_c = 0.6$ to $T_c = 8.4$ K. The differences between these compounds are found to be related to the detailed physico-chemical structures of the compounds, as supported by our data analysis and band structure

calculations. The present work on the effects of the physico-chemical influence on superconductivity represents the most systematic study in a same compound system of its type to date, although the effect has been suggested previously.

Bibliography

[1] J. Bardeen, L. N. Cooper, and J. R. Schrieffer. Theory of Superconductivity. *Physical Review*, 108(5):1175–1204, 1957.

[2] George F. Hardy and John K. Hulm. Superconducting Silicides and Germanides. *Physical Review*, 89(4):884, 1953.

[3] Bt Matthias, Th Geballe, S. Geller, and E. Corenzwit. Superconductivity of Nb_{3} Sn. *Physical Review*, 95(6):1435–1435, 1954.

[4] B.T. Matthias, T.H. Geballe, R.H. Willens, E. Corenzwit, and G.W. Hull Jr. Superconductivity of Nb3Ge. *Physical Review*, 139(5A):A1501 – A1503, 1965.

[5] L.R. Testardi, J.H. Wernick, and W.A. Royer. Superconductivity with onset above 23 K in Nb-Ge Sputtered Films. *Solid State Communications*, 15:1–4, 1974.

[6] W.L. McMillan. Transition Temperature of Strong-coupled Superconductors. *Physical Review*, 167(2):331–343, 1968.

[7] F. Steglich, J. Aarts, C.D. Bredl, W. Lieke, D. Meschede, W. Franz, and H. Schafer. Superconductivity in the Presence of Strong Pauli Paramagnetism: CeCu2Si2. *Physical Review Letters*, 43(25):1892–1896, 1979.

[8] J.G. Bednorz and K.A. Muller. Possible High-Tc Superconductivity in the Ba-La-Cu-O System. *Zeitschrift fur Physik B Condensed Matter*, 64(2):189–193, 1986.

[9] C.W. Chu, P.H. Hor, R.L. Meng, L. Gao, and Z.J. Huang. Superconductivity at 52.5 K in the Lanthanum-Barium-Copper-Oxide System. *Science*, 235(4788):567–569, 1987.

[10] C. W. Chu, P. H. Hor, R. L. Meng, L. Gao, Z. J. Huang, Wang, and Y Q. Evidence for Superconductivity above 40 K in the La-Ba-Cu-O Compound System. *Physical Review Letters*, 58(4):405–407, 1987.

[11] P. H. Hor, L. Gao, R. L. Meng, Z. J. Huang, and Y. Q. Wang. High-pressure Study of the new Y-Ba-Cu-O Superconducting Compound System. *Physical Review Letters*, 58(9):911–912, 1987.

[12] M. K. Wu, J. R. Ashburn, C. J. Torng, P. H. Hor, R. L. Meng, L. Gao, Z. J. Huang, Y. Q. Wang, and C. W. Chu. Superconductivity at 93 K in a new mixed-phase Y-Ba-Cu-O compound system at ambient pressure. *Physical Review Letters*, 58(9):908–910, 1987.

[13] C.W. Chu, J. Bechtold, L. Gao, P.H. Hor, Z.J. Huang, R.L. Meng, Y.Y. Sun, Y.Q. Wang, and Y.Y. Xue. Superconductivity up to 114 K in the Bi - Al - Ca - Sr - Cu - O Compound System without Rare-Earth Elements. *Physical Review Letters*, 60(10):941–943, 1988.

[14] Hiroshi Maeda, Yoshiaki Tanaka, Masao Fukutomi, and Toshihisa Asano. A New High - Tc Oxide Superconductor without a Rare Earth Element. *Japanese Journal of Applied Physics*, 27(2):L209–L210, 1988.

[15] Z.Z. Sheng and A.M. Hermann. Bulk Superconductivity at 120 K in the Tl - Ca/Ba-Cu-O system. *Nature*, 332:138–139, 1988.

[16] A. Schilling, M. Cantoni, J.D. Guo, and H.R. Ott. Superconductivity above 130 K in the Hg - Ba - Ca - Cu - O System. *Nature*, 363:56 – 58, 1993.

[17] C.W. Chu, L. Gao, F. Chen, Z.J. Huang, R.L. Meng, and Y.Y. Xue. Superconductivity above 150 K in HgBa2Ca2Cu3O(8+delta) at High Pressures. *Nature*, 365:323 – 325, 1993.

[18] L. Gao, Y.Y. Xue, F. Chen, Q. Xiong, R.L. Meng, D. Ramirez, and C.W. Chu. Superconductivity up to 164 K in HgBa2Ca(m-1)Cu(2m+2+delta) under Quasihydrostatic Pressures. *Physical Review B*, 50(6):4260–4263, 1994.

[19] J Nagamatsu, N Nakagawa, T Muranaka, Y Zenitani, and J Akimitsu. Superconductivity at 39 K in Magnesium Diboride. *Nature*, 410(6824):63–64, 2001.

[20] C.W. Chu. A Possible Path to RTS. *AAPPS Bulletin*, 18(4):9–21, 2008.

[21] Andreas Barth and Werner Marx. Mapping High-temperature Superconductors - A Scientometric Approach. *Journal of Superconductivity and Novel Magnetism*, 21:113–128, January 2008.

[22] Yoichi Kamihara, Takumi Watanabe, Masahiro Hirano, and Hideo Hosono. Iron-based Layered Superconductor La[O(1-x)Fx] FeAs(x = 0.05 -0.12) with Tc = 26 K. *Journal of the American Chemical Society*, 130(11):3296–3297, 2008.

[23] Yoichi Kamihara, Takumi Watanabe, Masahiro Hirano, and Hideo Hosono. Iron-based Layered Superconductor La[O(1-x)F(x)]FeAs (x = 0.05-0.12) with T(c) = 26 K. *Journal of the American Chemical Society*, 130(11):3296–7, March 2008.

[24] K. Hasselbach, L. Taillefer, and J. Flouquet. Critical Point in the Superconducting Phase Diagram of UPt3. *Physical Review Letters*, 63(1):93–96, 1989.

[25] R.A. Fisher, S. Kim, B.F. Woodfield, N.E. Phillips, L. Taillefer, K. Hasselbach, J. Flouquet, A.L. Giorgi, and J.L. Smith. Specific Heat of UPt3: Evidence for Unconventional Superconductivity. In H.R. Ott, editor, *Ten Years of Superconductivity: 1980 - 1990*, pages 189–192. Springer, 1993.

[26] M.I. Eremets, I.A. Trojan, S.A. Medvedev, J.S. Tse, and Y. Yao. Superconductivity in Hydrogen Dominant Materials: Silane. *Science*, 319:1506–1510, 2008.

[27] Thomas Scheler, Olga Degtyareva, Miriam Marqués, Christophe L. Guillaume, John E. Proctor, Shaun Evans, and Eugene Gregoryanz. Synthesis and Properties of Platinum Hydride. *Physical Review B*, 83(21):214106, June 2011.

[28] Xiang-Feng Zhou, Artem R. Oganov, Xiao Dong, Lixin Zhang, Yongjun Tian, and Hui-Tian Wang. Superconducting High-pressure Phase of Platinum Hydride from First Principles. *Physical Review B*, 84(5):054543, August 2011.

[29] E. Bauer, G. Hilscher, H. Michor, Ch. Paul, E.W. Scheidt, A. Gribanov, Yu. Seropegin, H. Noël, M. Sigrist, and P. Rogl. Heavy Fermion Superconductivity and Magnetic Order in Noncentrosymmetric CePt3Si. *Physical Review Letters*, 92(2):027003, January 2004.

[30] U. Eibenstein and W. Jung. Li2Pd3B and Li2Pt3B: Ternary Lithium Borides of Palladium and Platinum with Boron in Octahedral Coordination. *J. Solid State Chemistry*, 133(1):21–24, 1997.

[31] K. Togano, P. Badica, Y. Nakamori, S. Orimo, H. Takeya, and K. Hirata. Superconductivity in the Metal-rich Li-Pd-B Ternary Boride. *Physical Review Letters*, 93(24):1–4, 2004.

[32] H. Q. Yuan, D. F. Agterberg, N. Hayashi, P. Badica, D. Vandervelde, K. Togano, M. Sigrist, and M. B. Salamon. S-wave Spin-triplet Order in Superconductors without Inversion Symmetry: Li2Pd3B and Li2Pt3B. *Physical Review Letters*, 97(1):5–8, 2006.

[33] Yoshihiro Nishikubo, Kazutaka Kudo, and Minoru Nohara. Superconductivity in the Honeycomb-Lattice Pnictide SrPtAs. *Journal of the Physical Society of Japan*, 80:1–2, 2011.

[34] H.C. Ku, I.a. Chen, C.H. Huang, C.W. Chen, Y.B. You, M.F. Tai, and Y.Y. Hsu. New Superconductor SrPt2Ge2 with Tc=10.2K. *Physica C: Superconductivity*, 493:93–95, October 2013.

[35] E. Bauer, A. Grytsiv, Xing Qiu Chen, N. Melnychenko-Koblyuk, G. Hilscher, H. Kaldarar, H. Michor, E. Royanian, G. Giester, M. Rotter, R. Podloucky, and P. Rogl. Superconductivity in Novel Ge-based Skutterudites: {Sr,Ba}Pt4Ge12. *Physical Review Letters*, 99(21):1–4, 2007.

[36] T. Takayama, K. Kuwano, D. Hirai, Y. Katsura, A. Yamamoto, and H. Takagi. Strong Coupling Superconductivity at 8.4 K in an Antiperovskite Phosphide SrPt3P. *Physical Review Letters*, 108(23):237001, June 2012.

[37] H.K. Onnes. The Resistance of Pure Mercury at Helium Temperatures. *Commun. Phys. Lab. Univ. Leiden*, 12, 1911.

[38] W. Meissner and R. Ochsenfeld. Ein neuer Effekt bei Eintritt der Supraleitfahigkeit. *Naturwissenchaften*, 21(44):787–788, 1933.

[39] Kristian Fossheim and Asle Sudbo. *Superconductivity Physics and Applications*. John Wiley & Sons Ltd, 2004.

[40] Leon N. Cooper. Bound Electron Pairs in a Degenerate Fermi Gas. *Physical Review*, 104(4):1189–1190, 1956.

[41] F. Bouquet, Y. Wang, R.A. Fisher, D.G. Hinks, J.D. Jorgensen, A. Junod, and N.E. Phillips. Phenomenological Two-gap Model for the Specific Heat of MgB2. *Europhysics Letters*, 56(6):856–862, 2001.

[42] A Gurevich, S Patnaik, V Braccini, K H Kim, C Mielke, X Song, L D Cooley, S D Bu, D M Kim, J H Choi, L J Belenky, J Giencke, M K Lee, W Tian, X Q Pan, A Siri, E E Hellstrom, C B Eom, and D C Larbalestier. Very High Upper Critical Fields in MgB2 Produced by Selective Tuning of Impurity Scattering. *Superconductor Science and Technology*, 17(2):278–286, February 2004.

[43] H. Padamsee, J. E Neighbor, and C. A. Shiffman. Quasiparticle Phenomenology for Thermodynamics of Strong-coupling Superconductors. *Journal of Low Temperature Physics*, 12(3-4):387–411, August 1973.

[44] David C Johnston. Elaboration of the α-Model Derived from the BCS Theory of Superconductivity. *Superconductor Science and Technology*, 26(11):115011, November 2013.

[45] Paolo Giannozzi, Stefano Baroni, Nicola Bonini, Matteo Calandra, Roberto Car, Carlo Cavazzoni, Davide Ceresoli, Guido L Chiarotti, Matteo Cococcioni, Ismaila Dabo, Andrea Dal Corso, Stefano de Gironcoli, Stefano Fabris, Guido Fratesi, Ralph Gebauer, Uwe Gerstmann, Christos Gougoussis, Anton Kokalj, Michele Lazzeri, Layla Martin-Samos, Nicola Marzari, Francesco Mauri, Riccardo Mazzarello, Stefano Paolini, Alfredo Pasquarello, Lorenzo Paulatto, Carlo Sbraccia, Sandro Scandolo, Gabriele Sclauzero, Ari P Seitsonen, Alexander Smogunov, Paolo Umari, and Renata M Wentzcovitch. QUANTUM ESPRESSO: a Modular and Open-source Software Project for Quantum Simulations of Materials. *Journal of Physics: Condensed Matter*, 21(39):395502, 2009.

[46] Cristina Buzea and Tsutomu Yamashita. Review of the Superconducting Properties of MgB2. *Superconductor Science and Technology*, 14:R115–R146, 2001.

[47] N. I. Medvedeva, A. L. Ivanovskii, J. E. Medvedeva, and A. J. Freeman. Electronic Structure of Superconducting MgB2 and Related Binary and Ternary Borides. *Physical Review B*, 64(2):020502, June 2001.

[48] A Bharathi, S Jemima Balaselvi, M Premila, T.N Sairam, G.L.N Reddy, C.S Sundar, and Y Hariharan. Synthesis and Search for Superconductivity in LiBC. *Solid State Communications*, 124(10-11):423–428, December 2002.

[49] H. Rosner, A. Kitaigorodsky, and W. E. Pickett. Prediction of High Tc Superconductivity in Hole-doped LiBC. *Physical Review Letters*, 88(12):127001, March 2002.

[50] B Lorenz and C W Chu. High Pressure Effects on Superconductivity. In *Frontiers in Superconducting Materials*, volume d, pages 459–497. 2005.

[51] J P Carbotte. Properties of Boson-exchange Superconductors. *Review of Modern Physics*, 62(4), 1990.

[52] B. Lachal, A. Junod, and J. Muller. Heat Capacity Analysis of a Large Number of Chevrel-type Superconductors. *Journal of Low Temperature Physics*, 55(3-4):195–232, May 1984.

[53] Z. Hiroi, S. Yonezawa, Y. Nagao, and J. Yamaura. Extremely Strong-coupling Superconductivity and Anomalous Lattice Properties in the β-Pyrochlore Oxide KOs2O6. *Physical Review B*, 76(1):014523, July 2007.

[54] Zenji Hiroi, Shigeki Yonezawa, Takaki Muramatsu, Jun-Ichi Yamaura, and Yuji Muraoka. Specific Heat of the β-Pyrochlore Oxide Superconductors CsOs 2 O 6 and RbOs 2 O 6. *Journal of the Physical Society of Japan*, 74(4):1255–1262, April 2005.

[55] Chang-Jong Kang, Kyo-Hoon Ahn, Kwan-Woo Lee, and Byung Il Min. Electron and Phonon Band-Structure Calculations for the Antipolar SrPt3P Antiperovskite Superconductor: Evidence of Low-energy Two-dimensional Phonons. *Journal of the Physical Society of Japan*, 82(5):053703, 2013.

[56] Alaska Subedi, Luciano Ortenzi, and Lilia Boeri. Electron-Phonon Superconductivity in APt3P (A=Sr,Ca,La) Compounds: From Weak to Strong Coupling. *Physical Review B*, 87(14):144504, April 2013.

[57] I. a. Nekrasov and M. V. Sadovskii. Electronic Structure of New Multiple Band Pt-Pnictide Superconductors APt3P. *JETP Letters*, 96(4):227–230, October 2012.

[58] R.D. Shannon. Revised Effective Ionic Radii and Systematic Studies of Interatomic Distances in Halides and Chalcogenides. In *Acta Crystallographica*, chapter A32, pages 751–767. 1976.

[59] R. Khasanov, A. Amato, P. K. Biswas, H. Luetkens, N. D. Zhigadlo, and B. Batlogg. SrPt3P: A Two-band Single-gap Superconductor. *Physical Review B*, 90(14):140507, October 2014.

[60] BenMaan I. Jawdat, Bing Lv, Xiyu Zhu, Yuyi Xue, and Ching-wu Chu. High-pressure and Doping Studies of the Superconducting Antiperovskite SrPt3P. *Physical Review B*, 91(9):094514, March 2015.

[61] James S Schilling. What High Pressure Studies Have Taught us About High-Temperature Superconductivity. In *Frontiers of High Pressure Research II:*

Application of High Pressure to Low-Dimensional Novel Electronic Materials, pages 345–360. Springer Netherlands, 2001.

[62] A.F. Wells. *Structural Inorganic Chemistry, 5th ed.* Oxford University Press, Oxford, U.K., 1984.

[63] Myung-Hwan Whangbo, Changhoon Lee, and Jürgen Köhler. Transition-metal Anions in Solids and their Implications on Bonding. *Angewandte Chemie (International ed. in English)*, 45(44):7465–9, November 2006.

[64] Myung-Hwan Whangbo, Changhoon Lee, and Jürgen Köhler. Metal Anions in Metal-rich Compounds and Polar Intermetallics. *European Journal of Inorganic Chemistry*, (26):3841–3847, September 2011.

[65] Jürgen Köhler and Myung-Hwan Whangbo. Late Transition Metal Anions acting as p-metal Elements. *Solid State Sciences*, 10(4):444–449, April 2008.

[66] Jürgen Köhler and Myung-hwan Whangbo. Electronic Structure Study of the [Ag - Ag] 4 - , [Au - Au] 4 - , and [Hg - Hg] 2 - Zintl Anions in the Intermetallic Compounds Yb 3 Ag 2 , Ca 5 Au 4 , and Ca 3 Hg 2 : Transition Metal Anions As p-Metal Elements. *Chemistry of Materials*, (20):2751–2756, 2008.

[67] Richard Dronskowski and Peter E. Blochl. Crystal Orbital Hamilton Populations (COHP): Energy-resolved Visualization of Chemical Bonding in Solids Based on Density-functional Calculations. *The Journal of Physical Chemistry*, 97(33):8617–8624, August 1993.

[68] T.F. Smith. Pressure Dependence of the Superconducting Transition Temperature for Niobium. *Physics Letters*, 33A(7):465–466, 1970.

[69] H. Suhl, B.T. Matthias, and L.R. Walker. Bardeen-Cooper-Schrieffer Theory of Superconductivity in the Case of Overlapping Bands. *Physical Review Letters*, 3(12):552–554, 1959.